NTNU

Norwegian University of
Science and Technology

Comparison of vertically sided model structures with circular and rectangular cross section subjected to ice-induced vibrations in the frequency lock-in regime

Cody Carlton Owen

Wind Energy

Submission date: September 2017

Supervisor: Zhen Gao, IMT

Co-supervisor: Michael Muskulus, NTNU, Department of Civil and Environmental Engineering
Hayo Hendrikse, TU Delft, CITG

Norwegian University of Science and Technology
Department of Marine Technology

Ice-induced Vibrations of Vertically Sided Model Structures

Comparison of structures with circular and rectangular cross-section subjected to the frequency lock-in regime

Cody C. Owen

Master of Science Thesis

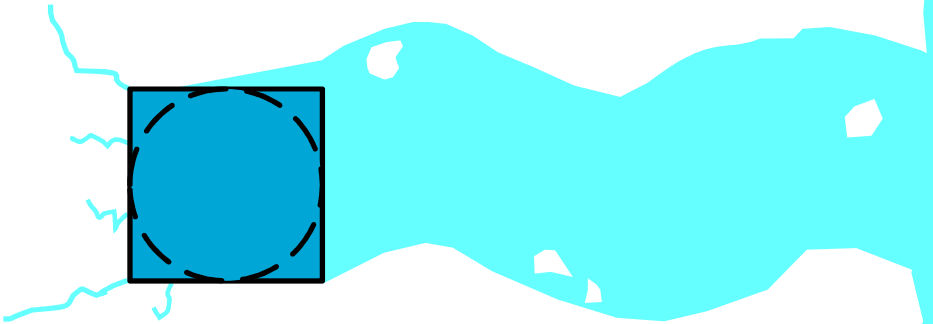

TU Delft Delft University of Technology

HSVA

NTNU
Norwegian University of Science and Technology

Ice-induced Vibrations of Vertically Sided Model Structures

Comparison of structures with circular and rectangular cross-section subjected to the frequency lock-in regime

Master of Science Thesis

For obtaining the degree of Master of Science in
Offshore and Dredging Engineering at the Delft University of Technology
and
Technology-Wind Energy at the Norwegian University of Science and Technology
as organized by
the Offshore Engineering track of the European Wind Energy Master joint education program.

Cody C. Owen

at the Delft University of Technology,
29 September 2017

Committee:	Prof. A. Metrikine	TU Delft - Chairman
	dr. ir. H. Hendrikse	TU Delft
	ir. M. van den Berg	TU Delft
	Dipl.-Ing. G. Ziemer	HSVA
	P. Hinse, M.Sc.	HSVA
	Prof. M. Muskulus	NTNU
	W. Popko, MSc	NTNU

EWEM

TU Delft Delft University of Technology

HSVA

NTNU Norwegian University of Science and Technology

PREFACE

This thesis is submitted as part of the requirement for obtaining the degree of Master of Science in Offshore and Dredging Engineering at the Delft University of Technology (TU Delft) and in Technology-Wind Energy at the Norwegian University of Science and Technology (NTNU). The program for the Master of Science was organized by the Offshore Engineering track of the European Wind Energy Master joint education program. The work contained herein was conducted primarily in the Faculty of Civil Engineering and Geosciences at TU Delft under regular supervision from dr. ir. H. Hendrikse. The work was completed between December 2016 and September 2017 and in collaboration with the Hamburg Ship Model Basin (HSVA) in Germany, where the author began the thesis by observing the experiments in the Large Ice Basin. Main supervision from HSVA was provided by Dipl.-Ing. G. Ziemer by means of videoconferencing. And Prof. M. Muskulus from the Department of Civil and Environmental Engineering acted as main supervisor from NTNU.

Sincere gratitude is given to the all of my committee members for their guidance throughout this work. I would like to thank Gesa for taking the time to meet with me after her presentation at the WindEurope Summit 2016. I would also like to express my gratitude to Hayo for meeting with me while he was at NTNU for the SAMCoT workshops and for inviting me to one of those inspiring workshops. Thank you, Marnix, for helping me with the initial stages of the thesis at TU Delft while Hayo was on his duly-deserved post-PhD holiday. And thank you, Philipp, for the support from HSVA while Gesa was on maternity leave. Thanks is given to Zhen Gao, Stathis Tsigkris, Michael Armstrong, Tom Willems, Jeroen Hoving, and Sven Voormeeren for assisting me in finding a thesis topic. Last but most certainly not least, I am so grateful to all of my family, friends, classmates, and office-mates for their undying support during this master program and thesis.

Cody C. Owen
Delft, September 2017

Abstract

Offshore wind energy has very recently begun expanding into subarctic regions with seasonally ice-infested waters like the Baltic Sea. For offshore wind turbines with conventional support structures such as monopiles and jackets that are typically flexible and vertically sided, the phenomenon known as ice-induced vibrations can develop. In response to the growing interest in offshore wind in the Baltic Sea and in further validating a state-of-the-art numerical model for ice-structure interaction, the Ice-induced Vibrations of Offshore Structures (IVOS) project has been coordinated with the Hamburg Ship Model Basin (HSVA) and many academic and industry partners—including TU Delft and NTNU—in order to enhance understanding of the topic via a comprehensive laboratory testing campaign.

In this thesis, specific data are selected from the extensive IVOS Phase 2 tests such that a comparative analysis is performed between two different model-scale structures, one with circular cross-section and another with rectangular cross-section, that were subjected to ice-induced vibrations in the frequency lock-in regime. Preceding the comparative analysis, the data from the IVOS Phase 2 tests are organized into a database and post-processing tools are developed to facilitate further research by supplying analysis-ready data sets. Included in the post-processing tools is an attempt to determine ice-induced global loads from uncalibrated tactile sensor data, which offers insight into the relationship between the relative pressure distributions along the ice-structure interface and the ice-induced global forces on the model structure.

The comparative analysis garnered qualitative information about the frequency lock-in regime and buckling failure of ice. It is observed that frequency lock-in vibrations usually persisted regardless of buckling events. For the frequency lock-in regime, the ice-induced global loads on the circular cross-section structure are generally lower than those for the rectangular cross-section structure. It is unclear whether the difference in global loads between the structures is caused by the difference in cross-sectional shape, other structural properties, ice properties, or combinations thereof. The analysis of the energy of the system is intriguing but does not offer lucid conclusions. However, the quasi-figure-eight pattern from the x-direction and derived y-direction structural displacements is an enlightening discovery that may explain inconsistencies in the energy of the system. Based on the general configuration of the test apparatus from the IVOS Phase 2 tests and the results from the comparative analysis, it can be concluded that ice-induced vibrations of the model-scale structures in the frequency lock-in regime should be regarded as a two-dimensional problem.

CONTENTS

1

INTRODUCTION

Past experience and research regarding design of offshore structures in the Arctic and similar environments have culminated in standards such as ISO 19906, which mainly refers to offshore oil and gas platforms, lighthouses, and bridge piers (ISO 2010). Generally, these structures were massive, stiff, and designed with the luxury of conservatism (see Figure 1.1). Various vertically sided offshore structures, ranging from channel markers in the Baltic Sea to the enormous Molikpaq platform in the Beaufort Sea, have encountered detrimental structural vibrations caused by sea ice (Kärnä et al. 2013). This phenomenon, referred to as ice-induced vibrations, has been subject to unresolved investigation for approximately the last 50 years (Peyton 1968).

Figure 1.1: Photograph of the Norströmsgrund lighthouse, an exemplary offshore structure in the subarctic Gulf of Bothnia from Bjerkås et al. (2013).

Currently, design standards do not provide an adequate means of predicting ice-induced vibrations or the consequential ice-induced loads on and displacements of a structure (Kärnä et al. 2013). Before 2015, several numerical models that simulated ice-induced vibrations had been developed with different levels of success, but none of the models offered predictive capabilities. Instead, the models could only emulate existing events, albeit with fine-tuning of parameters (Kärnä et al. 2013). More recently, an auspicious phenomenological model was created by Hendrikse & Metrikine (2015) that predicted ice-induced vibrations based on the novel concept of contact area variation between the ice and structure. This model was later partially substantiated with laboratory testing by Hendrikse & Metrikine (2016*a*) and then appended with ice buckling failure by Hendrikse & Metrikine (2016*b*); all of this was summarized by Hendrikse (2017).

Offshore wind energy has very recently begun expanding into subarctic regions with seasonally ice-infested waters like the Baltic Sea. In contrast to the design of offshore structures referenced in ISO 19906, the design of offshore wind turbines mandates optimization to aspire to economic feasibility. Additionally, ice-induced vibrations are very pertinent to the design of offshore wind turbines in regions with sea ice since conventional

support structures, including monopiles and jackets, are typically flexible and vertically sided. In response to the growing interest in offshore wind in the Baltic Sea and in further validating the numerical model proposed by Hendrikse (2017), the Ice-induced Vibrations of Offshore Structures (IVOS) project has been coordinated with Hamburgische Schiffbau-Versuchsanstalt (HSVA) and many academic and industry partners—including TU Delft and NTNU—in order to enhance understanding of the topic via a comprehensive laboratory testing campaign.

1.1. RESEARCH MOTIVATION

Much is still uncertain about the phenomenon that is ice-induced vibrations. Moreover, the phenomenological model by Hendrikse (2017) requires further validation by means of comparison with events from model-scale experiments and full-scale observations. Having been granted access to the extensive data from the IVOS project, the author aspires to analyze the data in a manner that improves comprehension of ice-induced vibrations and provides a framework with which to later validate and upgrade the state-of-the-art phenomenological model.

1.2. RESEARCH OBJECTIVES AND SCOPE

The broad aim of this research is, from the extensive data acquired during the IVOS project, to select and analyze specific data in such a way that knowledge is gained about ice-induced vibrations. Due to the multitude and variety of data, a specific aim was chosen to narrow the scope of the study. The scope of the research is posed as an inquiry that is then answered with objectives for the study.

1.2.1. RESEARCH QUESTIONS

For this study, a particular aim was formulated as the main research question:

To what extent does cross-sectional geometry of a vertically sided model structure influence the global behavior of ice during the frequency lock-in regime of ice-induced vibrations?

To further address the aim of the research, the main question is divided into the following sub-questions:

1. In this context, how does circular cross-sectional geometry compare with rectangular cross-sectional geometry?
2. Which criteria are selected to identify the frequency lock-in regime of ice-induced vibrations for a given structure?
3. How much is the global behavior of the ice-structure interaction impacted by the difference in cross-sectional geometry?

1.2.2. RESEARCH OBJECTIVES

To answer the above research questions and define the scope of the study, the following research objectives and sub-objectives are set:

1. To create a database and analytical tools for the IVOS Phase 2 tests.
   (a) To convert and format experimental data into a database.
   (b) To develop universal tools for data post-processing and manipulation of data for further analysis.
2. To perform a comparative analysis of relevant data from tests with structures, one with circular cross-section and another with rectangular cross-section, that were subjected to ice-induced vibrations in the frequency lock-in regime.
   (a) To select tests with similar ice and structural properties, specifically one structure with circular cross-section and another structure with rectangular cross-section.
   (b) To define criteria for identifying the frequency lock-in regime of ice-induced vibrations for a given structure.

(c) To compare the global behavior of the ice-structure interaction between the different structures.

These objectives are expounded in the following chapters, which are summarized in the next section.

1.3. REPORT OUTLINE

Chapter 2 briefly introduces the properties of ice and structure that are most relevant to the ice-structure interaction problem. Chapter 3 then defines and details the ice-structure interaction problem, including ice-induced vibrations. Next, in Chapter 4, the description of the IVOS Phase 2 tests is provided. After, Chapter 5 elaborates the experimental data post-processing. Chapter 6 presents the global comparative analysis of the pertinent post-processed data. In addition, Chapter 7 introduces an extension of the comparative analysis to two-dimensional ice-structure interaction. Finally, Chapter 8 concludes the study in summary and offers recommendations for further research.

2

PROPERTIES OF ICE AND STRUCTURE

The interaction between a floating, level ice sheet and a vertically sided structure is a complicated process. Prior to introducing the ice-structure interaction problem, it is important to define and elucidate the properties of the ice and the structure involved in this interaction. The properties of ice, including the physics and mechanical behavior, are provided in Section 2.1. Then the structural properties are mentioned, but not exclusively, in terms of dynamical systems in Section 2.2.

2.1. ICE PROPERTIES

The properties of sea ice are most relevant in the design of offshore structures when considering ice actions on the structure. However, this study focuses on results from model-scale experiments and therefore does not examine the complexities of sea ice. The formation of ice in general is also not discussed, but the reader is provided references to literature in the Section 2.1.1. Of greatest interest to this study are the macroscopic properties of model-scale ice that govern the mechanical behavior, including deformation and failure of the ice; the mechanics of ice are explained in Section 2.1.2.

2.1.1. ICE PHYSICS

The micro- and macro-structure of ice and its formation are crucial in understanding the macroscopic behavior and features of an ice sheet. Notwithstanding, a description of these topics is excluded from this study since only macroscopic mechanical behavior of ice is considered. The reader is encouraged to review the synopsis by Willems (2016) or the detailed explanations by Løset et al. (2006), Schulson & Duval (2009) for information about the omitted topics.

2.1.2. ICE MECHANICS

For the purpose of this study, the mechanics of ice are defined—similarly to that from Willems (2016)—as the deformation behavior and eventual failure of ice in compression. The deformation behavior of ice is the focus of this section due to its importance in explaining the different failure modes of ice and the development of ice-induced vibrations during ice-structure interaction (see Chapter 3). Ice deformation can be characterized by ductile, transitional, or brittle behavior. Each deformation regime is described in the following sections with respect to material behavior and the general stress-strain relationship.

According to Løset et al. (2006), ice can be considered an elastic, visco-elastic-plastic material. This means that stress and the rate of application of stress influence the behavior such that the material responds with both solid- and fluid-like characteristics. This behavioral dependence of the ice on time and stress can be exemplified by a creep test as depicted in Figure 2.1. The creep test comprises very low loading rate in order for the behavior of the material to be fully demonstrated. Shown in Figure 2.1b, a load σ_0 is instantly applied at time $t = t_0$ that causes a immediate elastic strain ϵ_e as depicted in Figure 2.1a. After some duration, the load is removed at time $t = t_1$, causing a reduction in strain in the material. Prior to removal of σ_0, the material also endured a visco-elastic strain ϵ_{ve} and a visco-plastic strain ϵ_{vp}. Corresponding to the creep test, the total strain of the material ϵ_{tot} can be defined as follows:

$$\epsilon_{tot} = \epsilon_e + \epsilon_{ve} + \epsilon_{vp} \tag{2.1}$$

where the total strain is a superposition of the aforementioned strains; however, it should be noted that ϵ_{ve} and ϵ_{vp} are time-dependent and delayed whereas ϵ_e is time-invariant and instantaneous. The definition of elastic behavior in this case is fully recoverable deformation upon removal of some load; the definition of plastic behavior is permanent deformation of the material upon removal of some load. These different strains illustrate the behavior of the ice and are used to assist in the explanation of the different deformation regimes.

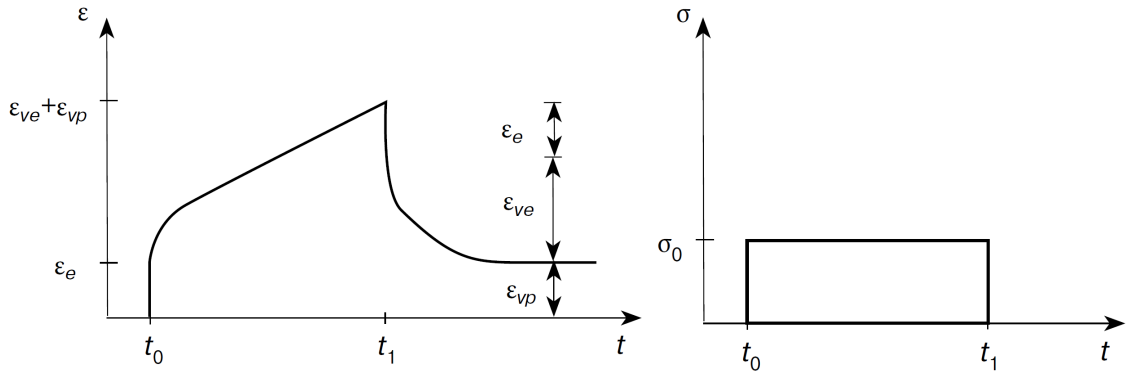

(a) Response of strain with time dependence.

(b) Controlled application of stress for specific duration.

Figure 2.1: Illustrative representation of creep test for an elastic, visco-elastic-plastic material adapted from Løset et al. (2006).

DUCTILE BEHAVIOR

The ductile behavior of ice is observed for relatively low loading or strain rates when visco-elastic and visco-plastic strain, in addition to elastic strain, can develop before the onset of ice failure. The stress-strain relationship for this behavior as a function of strain rate is represented on the left side in Figure 2.2. For increasing strain rates in ductile deformation, the behavior is accompanied by strain-rate hardening that grants an increasing maximum followed by a reduction and then asymptotic compressive stress (Schulson & Duval 2009).

TRANSITIONAL BEHAVIOR

The ductile-to-brittle transitional deformation of ice is generally indicated by a tranisitional, compressive strain rate $\dot{\epsilon}_{tc}$ as portrayed in Figure 2.2. Although the transition is typically marked by a single strain rate, the actual ductile-to-brittle transition occurs more gradually over a range of strain rates (Schulson & Duval 2009). The reason for the gradual ductile-to-brittle transition and consequently for a maximum ice compressive strength in this transition (see Figure 2.2) is the simultaneous strain-rate hardening from ductile behavior and strain-rate softening from brittle behavior (Schulson & Duval 2009).

BRITTLE BEHAVIOR

The brittle behavior of ice is observed for relatively high loading or strain rates when primarily only elastic strain can develop preceding failure. The stress-strain relationship for this behavior as a function of strain rate is displayed on the right side in Figure 2.2. Prior to the terminal failure stresses that are marked by an X in Figure 2.2, the propagation of micro-cracks in the ice causes temporary drops in the compressive stress (Schulson & Duval 2009). At the terminal failure stress, mechanical instability leads to a coalescence of micro-cracks and global failure of the ice. As previously mentioned, moderate strain-rate softening is observed with brittle behavior (Schulson & Duval 2009).

2.1.3. SUMMARY OF PERTINENT ICE PROPERTIES

The following properties of ice were provided by the IVOS Phase 2 tests (see Chapter 4) and serve as the pertinent ice properties for this study:

- Thickness

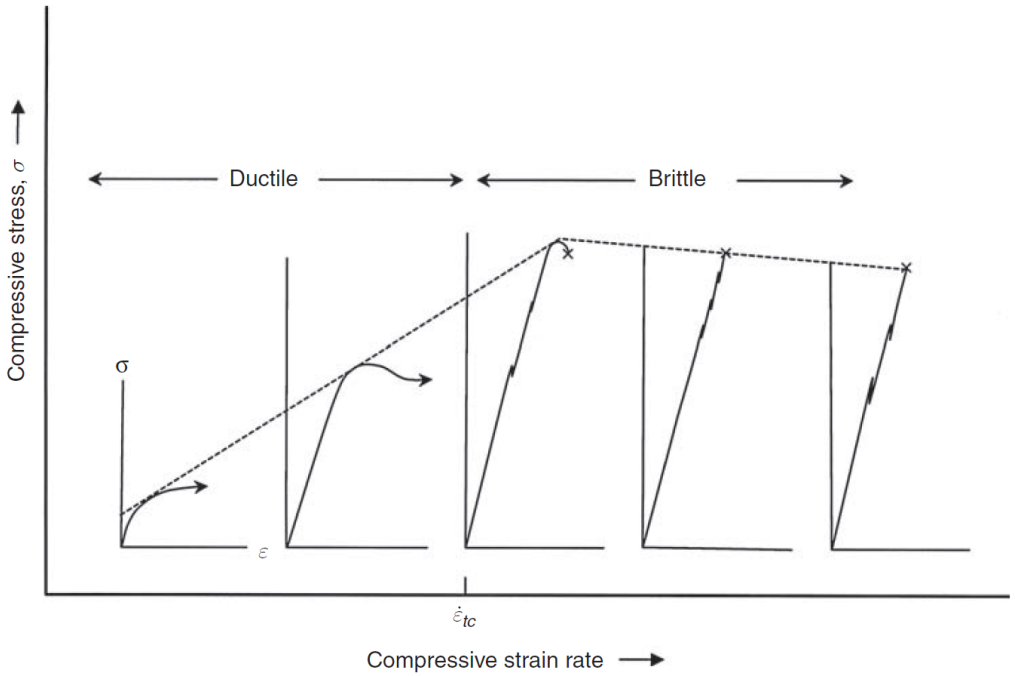

Figure 2.2: Illustrative representation of stress-strain relationship for ice as a function of strain rate from Schulson & Duval (2009). The ductile-to-brittle transition is indicated at the strain rate $\dot{\varepsilon}_{tc}$.

- Compressive strength
- Flexural strength
- Velocity

and all other properties of ice that govern strength and general behavior are either incorporated implicitly in the abovementioned properties or treated as constants and/or neglected in this study. Ice properties such as density, salinity, relative elastic modulus, and thin sections were recorded by HSVA, but were not directly considered for the analysis.

2.2. STRUCTURAL PROPERTIES

The features of a vertically sided offshore structure that are most fascinating for ice-structure interaction relate to the ice-structure interface and to the compliance of the structure. The flexibility of the structure permits a dynamic structural response during ice-structure interaction that can be modeled as a dynamical system, which is outlined in Section 2.2.1.

The ice-structure interface can be defined as the region of contact between the structure and the impinging ice sheet. As shown in Figure 2.3a, the contact area is typified in literature as the product of the ice thickness h and the width D of the structure (ISO 2010). However, this definition precludes the cross-sectional geometry of the structure at the ice-structure interface and its possible impact on the ice-structure interaction. Ergo, the shape of the structural cross-section is included in the definition of the ice-structure interface, which affects the contact area as well as implies a two-dimensional scenario (see Figure 2.3b). The two-dimensional ice-structure interface problem is addressed in Hendrikse (2017), Willems (2016) as well as Chapter 6 and Chapter 7.

2.2.1. STRUCTURAL DYNAMICS

The IVOS Phase 2 tests included experiments with a compliant test apparatus that was designed to act as a single-degree-of-freedom system (see Chapter 4). The test apparatus was assumed to move predominantly in one direction and the mass, stiffness, and damping of the system were modeled as illustrated in Figure 2.4. The equation of motion for a mass-spring-dashpot system subjected to a time-dependent external load $F(t)$ is written as follows:

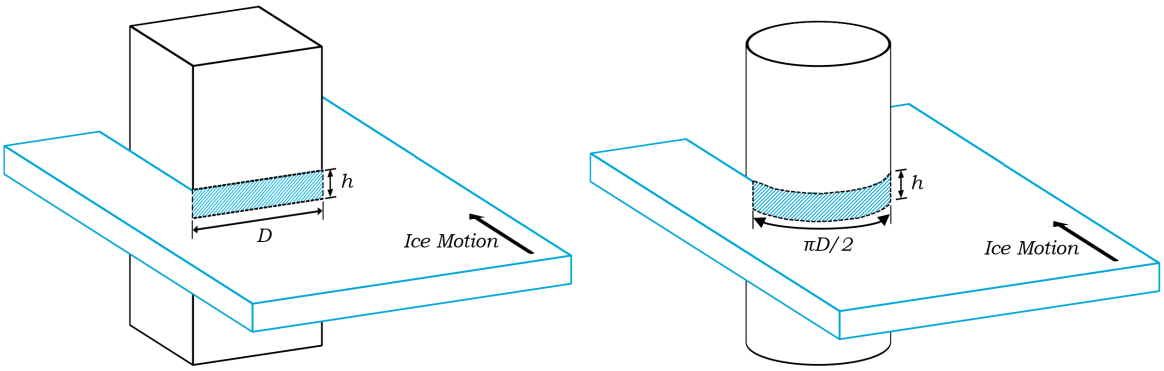

(a) Schematic for rectangular cross-section.

(b) Schematic for circular cross-section.

Figure 2.3: Schematics of ice-structure interface with structures of different cross-section. Contact area is indicated by the cross-hatched region and is defined as the product of the ice thickness h and the interaction width, which depends on the cross-sectional geometry of the structure.

$$m\ddot{x} + c\dot{x} + kx = F(t) \tag{2.2}$$

where m is the lumped mass, c is the viscous damping, k is the linear stiffness, $x(t)$ is the displacement of the mass from an equilibrium position, and $\dot{x}$ and $\ddot{x}$ are the velocity and acceleration of the mass, respectively. When dividing Equation 2.2 by m and introducing the natural frequency $\omega_n = \sqrt{k/m}$ and damping ratio $\zeta = c/(2m\omega_n)$, the equation of motion can be reformulated:

$$\ddot{x} + 2\zeta\omega_n\dot{x} + {\omega_n}^2 x = \frac{F(t)}{m} \tag{2.3}$$

where mass, stiffness, and damping ratio are the structural properties of interest in the dynamical system.

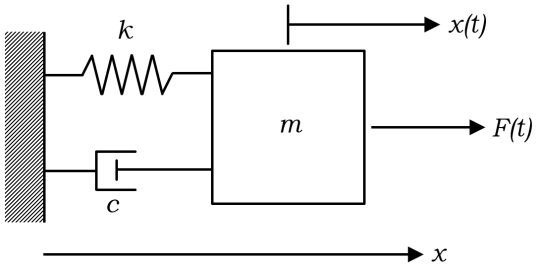

Figure 2.4: Schematic of single-degree-of-freedom dynamical system.

2.2.2. SUMMARY OF PERTINENT STRUCTURAL PROPERTIES

The following properties of structure were either explicitly provided by or derived from the IVOS Phase 2 tests (see Chapter 4 and Chapter 5) and serve as the pertinent structural properties for this study:

- Width
- Cross-sectional geometry
- Mass
- Stiffness
- Damping ratio

All other structural properties that influence the dynamics of the structure or the ice-structure interaction were either included implicitly in the abovementioned properties or treated as constants and/or neglected in this study.

3

ICE-STRUCTURE INTERACTION

When a floating, level ice sheet impinges on a vertically sided structure, the ice can fail by means of various mechanisms depending on various ice and structural properties. This chapter elaborates on the failure modes of ice due to ice-structure interaction and in terms of the ice and structural properties. Additionally, the total load exerted on the structure by the ice action, called the ice-induced global load, is described in terms of time dependence for each of the respective failure modes. First, a rigid structure is introduced in Section 3.1 to exemplify the behavior of ice without dynamic interaction with the structure. Then, in Section 3.2, a compliant structure is implemented to explain the development of ice-induced vibrations during dynamic ice-structure interaction.

3.1. ICE FAILURE MODES DURING INDENTATION WITH RIGID STRUCTURE

For the case of ice acting on a rigid structure, the structure is assumed to not move, deflect, or deform and thus cannot interact with the ice in any dynamic manner. The only structural properties which then contribute to the ice failure modes are the cross-sectional geometry and the width of the structure in contact with the ice. Therefore, the variation in ice properties primarily governs the ice failure modes and consequential ice-induced global loads, which are discussed in the following sections.

3.1.1. CREEP

Creep of ice occurs for relatively low ice velocities and low aspect ratios; this failure mode is associated with ice failure via mainly ductile deformation (Hendrikse 2017). Unless otherwise specified, the term aspect ratio is defined henceforth as the ratio between the width of the structure and the ice thickness. According to Blanchet et al. (1988), creep of ice can happen in-plane or out-of-plane; for this study, creep failure of ice is defined as in-plane and deforming in a plastic way to flow around the structure (see Figure 3.1). Nearly full contact and uniform pressure along the interface of the ice and structure is experienced during this failure mode (Hendrikse 2017).

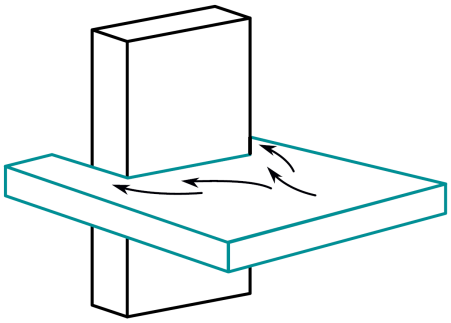

Figure 3.1: Schematic of in-plane creep failure from Willems (2016).

The dependence of ice-induced global load on time for creep is qualitatively shown in Figure 3.2. In this

case, the ice sheet begins to act on the structure when the load is small and then the load increases until reaching a maximum. Once this maximum is achieved, the load decreases and eventually a nearly constant, steady-state load is maintained (Sodhi 1991). This failure mode is not of much interest to this study because the range of ice velocities for which creep governs does not correspond to the ice velocities generally necessary for ice-induced vibrations to develop.

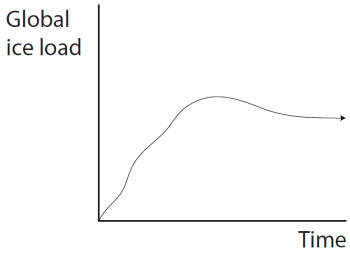

Figure 3.2: Illustrative representation of ice-induced global load in time caused by creep failure from Hendrikse (2017).

3.1.2. CRUSHING

Crushing failure of ice is witnessed for relatively high ice velocities and low aspect ratios (Hendrikse 2017). The failure of ice in crushing involves predominantly elastic deformation, formation and coalescence of micro-cracks, and then brittle failure in combinations of pulverization, spalling and flaking, and radial cracking (Hendrikse 2017). The ice-structure interface during crushing failure is characterized by local contact of high pressure zones (HPZ) of random size and duration—but typically form along the horizontal centerline of the interface—that transfer the majority of the load to the structure (Hendrikse 2017, Jordaan 2001, Sodhi 2001). Furthermore, the stochastic nature of ice crushing failure yields incomplete contact between the ice and structure.

The ice-induced global load during crushing failure is found to be quasi-random about a mean value, and the process of which is attributed to the HPZs and stochastic, local failure of ice (Hendrikse 2017). Ice rubble, from pulverization and spalling, can also cause a load the structure, but this load is small when compared to the load from the HPZs of the intact ice sheet (Hendrikse 2017). The qualitative nature of ice-induced global load in time from crushing failure is shown in Figure 3.3.

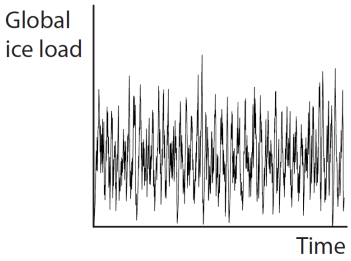

Figure 3.3: Illustrative representation of ice-induced global load in time caused by crushing failure from Hendrikse (2017).

PULVERIZATION

Ice crushing failure with pulverization begins when ice in local contact with the structure develops very high pressure as a result of confinement (Jordaan 2001). Also according to Jordaan (2001), once a certain stress level is achieved, the ice within the HPZ is pulverized and expelled from the HPZ; ice rubble accumulates above and below the ice-structure interface (see Figure 3.4).

SPALLING

Spalling (also known as flaking) can occur concurrently with pulverization during ice crushing failure. A spalling event starts when micro-cracks initiate in proximity to the HPZs and coalesce into cleavage cracks which propagate to the free surface of the ice sheet (Jordaan 2001). As shown in Figure 3.5, semicircular

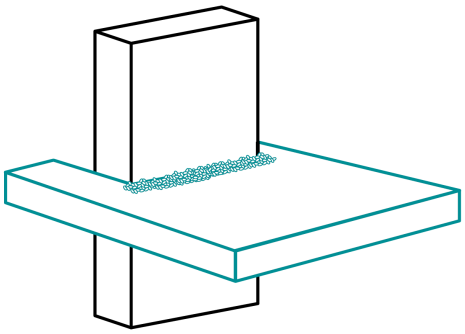

Figure 3.4: Schematic of ice crushing failure with pulverization from Willems (2016).

plate-shaped pieces of ice, called spalls, of various sizes are then extruded from the ice sheet, leaving a wedge shaped ice front (Hendrikse 2017, Palmer & Bjerkås 2013). Spalling is known to happen for aspect ratios greater than one (Hendrikse 2017).

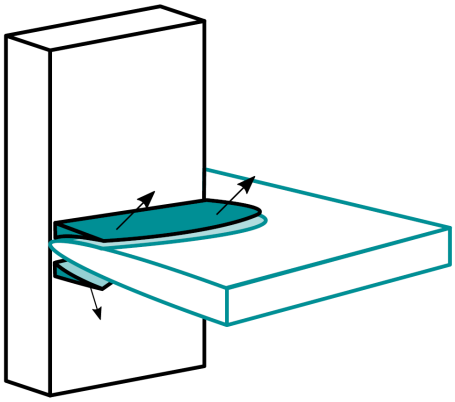

Figure 3.5: Schematic of ice crushing failure with spalling from Willems (2016).

RADIAL CRACKING

Radial cracking is defined as the propagation of cracks through the entire thickness of the ice sheet and radially from the ice-structure interface (Palmer et al. 1983). According to Willems (2016), crushing failure of ice with radial cracking is the prompted by in-plane tensile and shear failure in the direction of loading on the ice sheet (see Figure 3.6). Therefore, the formation and direction of radial cracks depend on the cross-sectional shape of the structure at the ice-structure interface. Although radial cracking may not limit the ice-induced loads exerted on the structure during the ice crushing failure mode, the cracks can have an impact on other failure modes (Palmer et al. 1983). It is important to note that, even though radial cracking can arise simultaneously with spalling and pulverization, radial cracking is typically observed for relatively higher aspect ratios when compared to other mechanisms of ice crushing failure (Willems 2016).

3.1.3. BUCKLING

Buckling failure of ice occurs for both low and high ice velocities and for high aspect ratios (Hendrikse 2017). For this study, buckling failure is defined for when the bending stress surpasses the flexural strength — pertaining to the critical buckling load—of the ice sheet and sufficient out-of-plane deformation ensues (see Figure 3.7a). Note that the term buckling refers to failure caused by in-plane compressive loads on the ice; however, vertical loads on the ice sheet such as the presence of ice rubble can produce a failure mode with similar results, namely bending failure (Hendrikse 2017). A consequence of the buckling failure is the formation of circumferential cracking, as shown in Figure 3.7b, which occurs along the front of flexural strength exceedance in the ice sheet (Willems 2016).

The ice-induced global load during buckling failure can follow the trend as shown in Figure 3.8. For each buckling failure event, contact between the ice sheet and structure is made, then the load increases until the

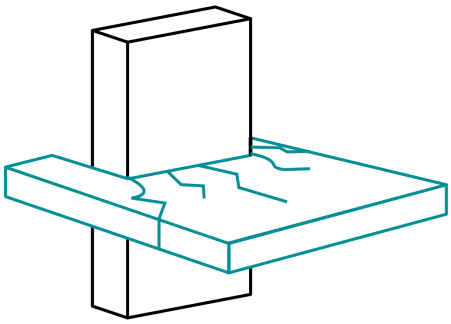

Figure 3.6: Schematic of ice crushing failure with radial cracking from Willems (2016).

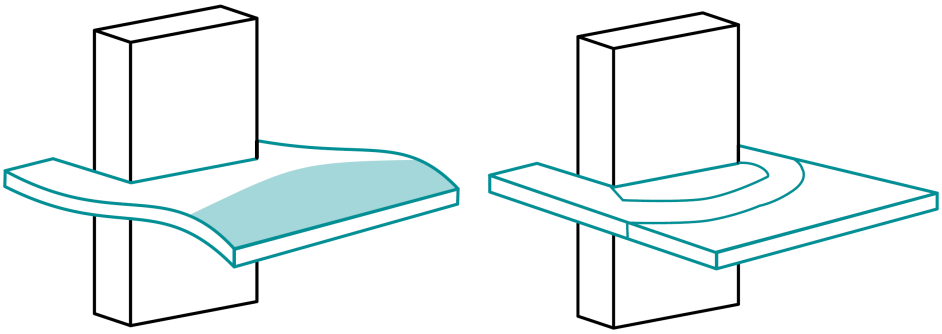

(a) Schematic of out-of-plane bending. (b) Schematic of circumferential cracking.

Figure 3.7: Schematics of buckling failure from Willems (2016).

critical buckling load of the ice sheet is reached. A global failure of the ice sheet swiftly ensues, causing a loss of contact between the structure and intact ice sheet and thus a steep drop in ice-induced global load. Between buckling failure events are periods of essentially zero load—or perhaps low loads from ice rubble—when the intact ice sheet and structure are not in contact.

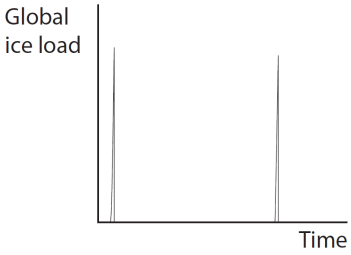

Figure 3.8: Illustrative representation of ice-induced global load in time caused by buckling failure from Hendrikse (2017).

3.1.4. FAILURE MODE MAP

A summary of the failure modes and the transitions between the modes is provided in Figure 3.9. The aspect ratio in Figure 3.9 is denoted as d/h on the abscissa and the velocity of the ice sheet is indicated by v_{ice} on the ordinate. Transitions between failure modes are suggested by the dashed lines. The horizontal dashed line corresponds to the transition velocity where a transition from ductile to brittle ice behavior is known to occur for small ice samples in compression (Schulson & Duval 2009). The downward diagonal dashed line represents the transition from creep to buckling failure for relatively low ice velocities and high aspect ratios where the flexural strength is less than the stress required to deform the ice sheet in creep (Hendrikse 2017). And the upward diagonal dashed line indicates the transition from crushing to buckling failure for relatively high ice velocities and high aspect ratios with the same rationale as that for the transition between creep and

buckling.

In terms of transitional failure modes, the mixed crushing and buckling failure mode is of interest to this study. Denoted as *m* on the failure mode map, the mixed crushing and buckling failure mode can have a substantial impact on ice-induced vibrations because this failure mode is observed within a similar range of ice velocities and aspect ratios to those of ice-induced vibrations. The mixed crushing and buckling failure mode is detailed in Section 3.1.5 and the impact of this failure mode on ice-induced vibrations is provided in Section 3.2.

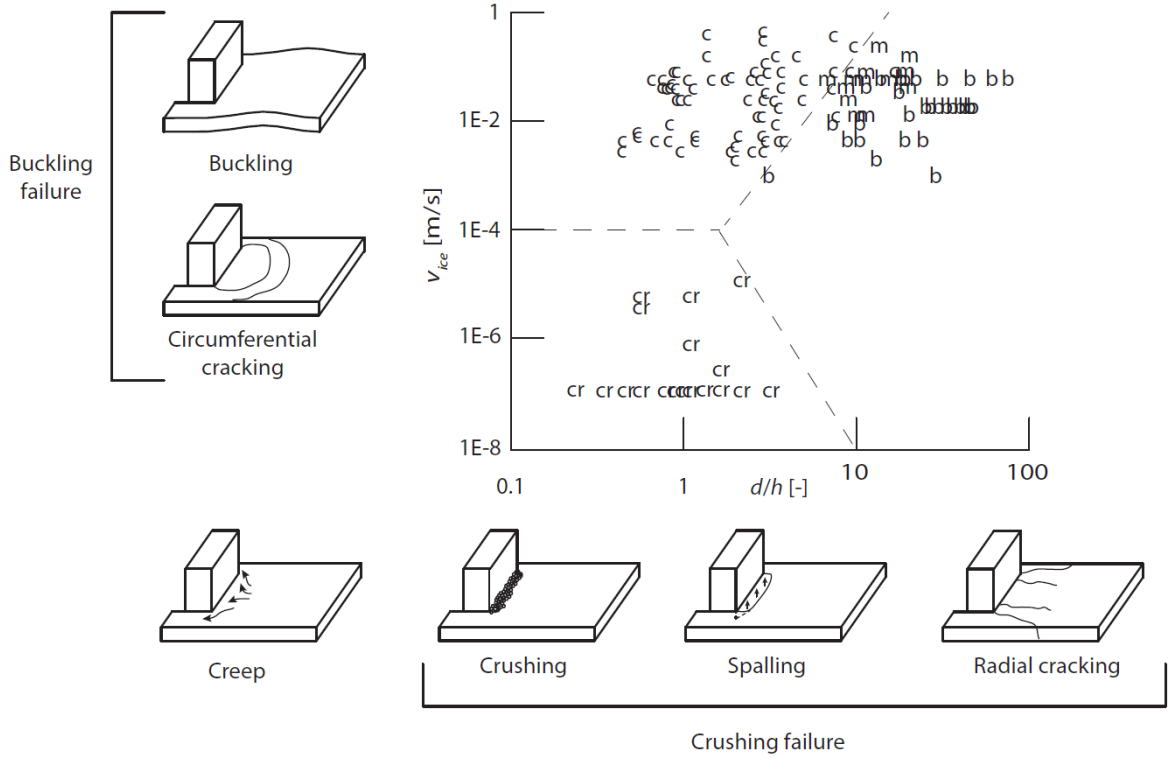

Figure 3.9: Illustration of ice failure mechanisms and failure mode map from Hendrikse (2017) using data from Timco (1991). Legend for failure mode map: cr - creep; c - crushing (including spalling, radial cracking); b - buckling (including circumferential cracking); m - mixed crushing and buckling.

3.1.5. MIXED CRUSHING AND BUCKLING

The mixed ice crushing and buckling failure mode marks a transition from crushing failure to buckling failure and consists of a mixture of both failure modes. Typically in this failure mode, a buckling failure is preceded by some duration of crushing (Hendrikse 2017). In terms of the ice-induced global load during mixed crushing and buckling failure, the the mixture of failure modes may appear as depicted in Figure 3.10.

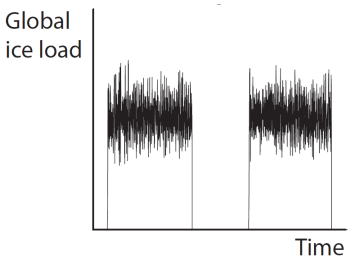

Figure 3.10: Illustrative representation of ice-induced global load in time caused by mixed crushing and buckling failure from Hendrikse (2017).

Because of the relatively high aspect ratios associated with this failure mode, radial cracking can form

and affect the buckling failure. Depending on the cross-sectional shape of the structure at the ice-structure interface, the radial cracks may generate ice wedges—as viewed from above—with different angles between cracks and thus different sizes of wedges (Kerr 1978). As portrayed in Figure 3.11, the ice wedges formed by the radial cracks from the rectangular cross-section structure are generally wider than those from the circular cross-section structure.

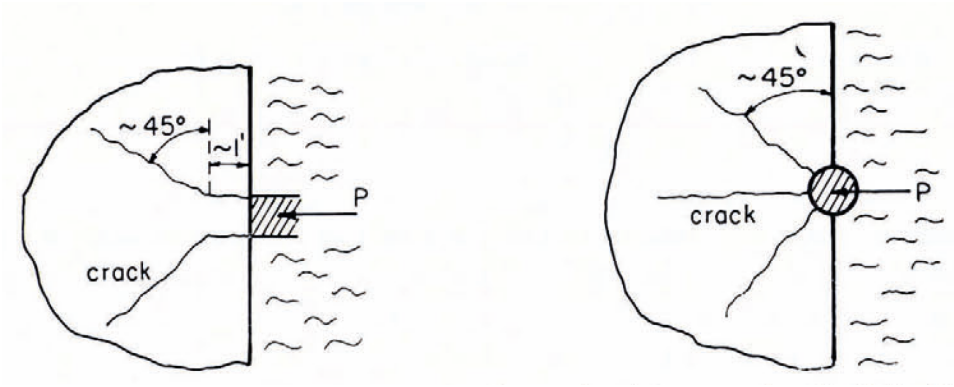

Figure 3.11: Observations of radial crack and resulting ice wedge formation for rectangular and circular cross-section structures from Kerr (1978).

The assumption was made by Kerr (1978) that an ice wedge can be modeled as a wedge shaped beam with Winkler elastic foundation that is subjected to a compressive load. Under this assumption, it was proposed that the transition from purely ice crushing failure to mixed crushing and buckling failure might be prompted at higher aspect ratios for the circular cross-section structure when compared to the rectangular cross-section structure of equivalent width. This is because the angle between radial cracks is smaller for the circular cross-section structure than that for the rectangular cross-section structure of equivalent width. The smaller angle means a lower buckling resistance for each ice wedge, but also a lower compressive load on the ice wedge (see Figure 3.12).

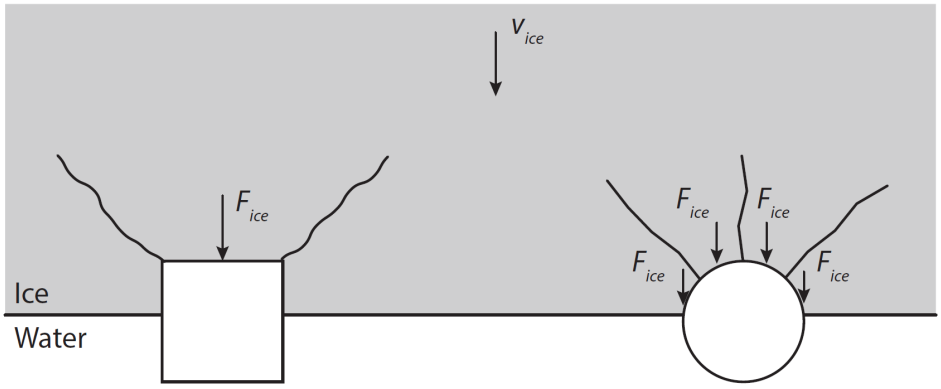

Figure 3.12: Schematic of ice-induced forces from ice wedges on rectangular and circular cross-section structures from Hendrikse (2017). Notation: v_{ice} - ice velocity; F_{ice} - ice-induced force on structure.

In the master thesis, Willems (2016) adapted the phenomenological model from Hendrikse & Metrikine (2015) to include both lateral motion and buckling failure for a structure with circular cross-section. As shown in Figure 3.13, Willems (2016) applied the assumption by Kerr (1978) such that radial cracks always formed four distinct ice wedges. It was concluded that buckling failure of ice should occur at greater ice thicknesses for a structure with a flat interaction surface (rectangular cross-section) than for a cylindrical structure (circular cross-section) of equivalent interaction width (Willems 2016).

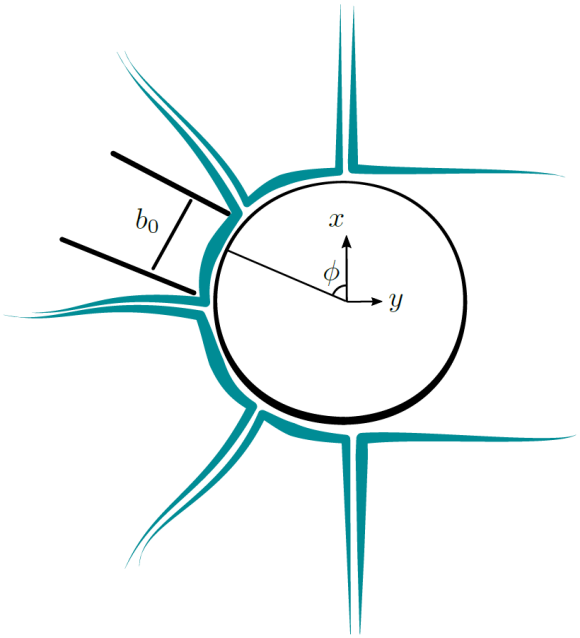

Figure 3.13: Schematic of ice wedge formation for circular cross-section structure from Willems (2016). Notation: y - direction parallel to ice motion; x - direction orthogonal to ice motion; ϕ - angle from x-axis to some location along circumference of structure; b_0 - contact width of ice wedge at ice-structure interface.

3.2. ICE-INDUCED VIBRATIONS

For the case of ice acting on a compliant structure, the structure is permitted to move or deflect and therefore can interact with the ice in a dynamic manner. The many structural properties, as well as ice properties, play an important role in the interaction of ice with the flexible structure. During the dynamic ice-structure interaction, vibration of the structure can arise and cause a unique synergism between the ice and the vibrating structure; this is known as ice-induced vibrations. Ice-induced vibrations can develop over a range of structural and ice properties and hence different ice failure modes.

Because the nature of creep failure of ice involves relatively low ice velocities and mostly plastic deformation, abrupt changes in ice-induced global load of significant magnitude on the structure do not transpire. Therefore, vibrations caused by creep are probably negligible and thus creep is not included in the discussion of ice-induced vibrations.

The process of ice-induced vibrations is most common for the ice crushing failure mode, which corresponds to low aspect ratios or relatively thick ice (Hendrikse 2017). Within the crushing failure mode of ice exist three regimes of ice-induced vibrations, which are defined as follows—using nomenclature by Hendrikse (2017)—in order of increasing ice velocity: intermittent crushing (ICR), frequency lock-in (FLI), and continuous brittle crushing (CBR). When comparing the ice failure modes with respect to ice velocity between a rigid and compliant structure, the regimes of ice-induced vibrations can be portrayed as shown in Figure 3.14. Depending the various ice and structural properties associated with the ice-structure interaction, the intermittent crushing and frequency lock-in regimes may not develop. Coincidentally, intermittent crushing and frequency lock-in are the most interesting of the three regimes due to the most significant global ice-induced loads and structural displacements observed within these regimes (Hendrikse 2017); notwithstanding, all three regimes of ice-induced vibrations are detailed in the following sections.

Buckling failure of ice is characterized by rapid changes in magnitude of ice-induced global load that can induce transient vibrations of the structure. However, Hendrikse (2017) refers to these vibrations as small in amplitude, meaning that ice-induced vibrations from buckling failure can be disregarded for this study. Ice buckling as a limiting mechanism for ice-induced vibrations is of much interest for this work but is a very new topic by Hendrikse (2017) and thus can only be considered as numerically experimental. This limiting mechanism is addressed in Section 3.2.4 in terms of ice-induced vibrations during mixed crushing and buckling failure of ice.

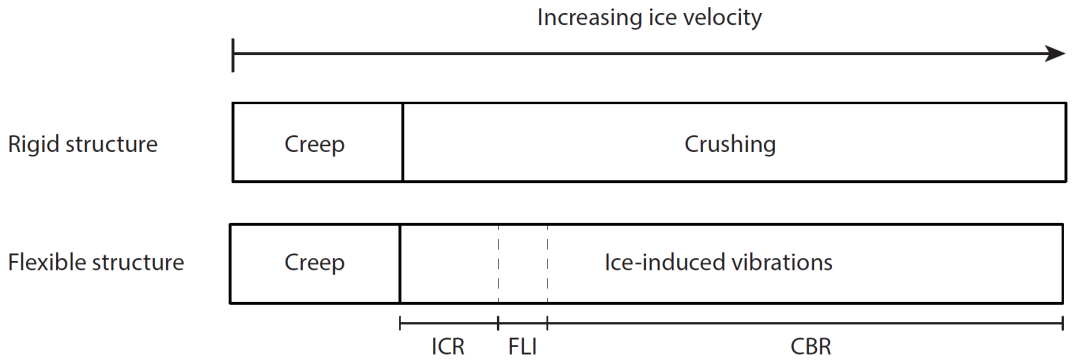

Figure 3.14: Illustration of ice failure modes with respect to ice velocity for rigid and flexible structures from Hendrikse (2017). Note that intermittent crushing and frequency lock-in may not progress in every case.

3.2.1. INTERMITTENT CRUSHING

The intermittent crushing regime of ice-induced vibrations can be invoked when an ice sheet with relatively low ice velocity interacts with a non-rigid structure (Hendrikse 2017). As seen in Figure 3.15, the structural displacement and ice-induced global load time signals of the intermittent crushing regime appear synchronized in time, proportional, and entail a saw-tooth like pattern (Hendrikse 2017).

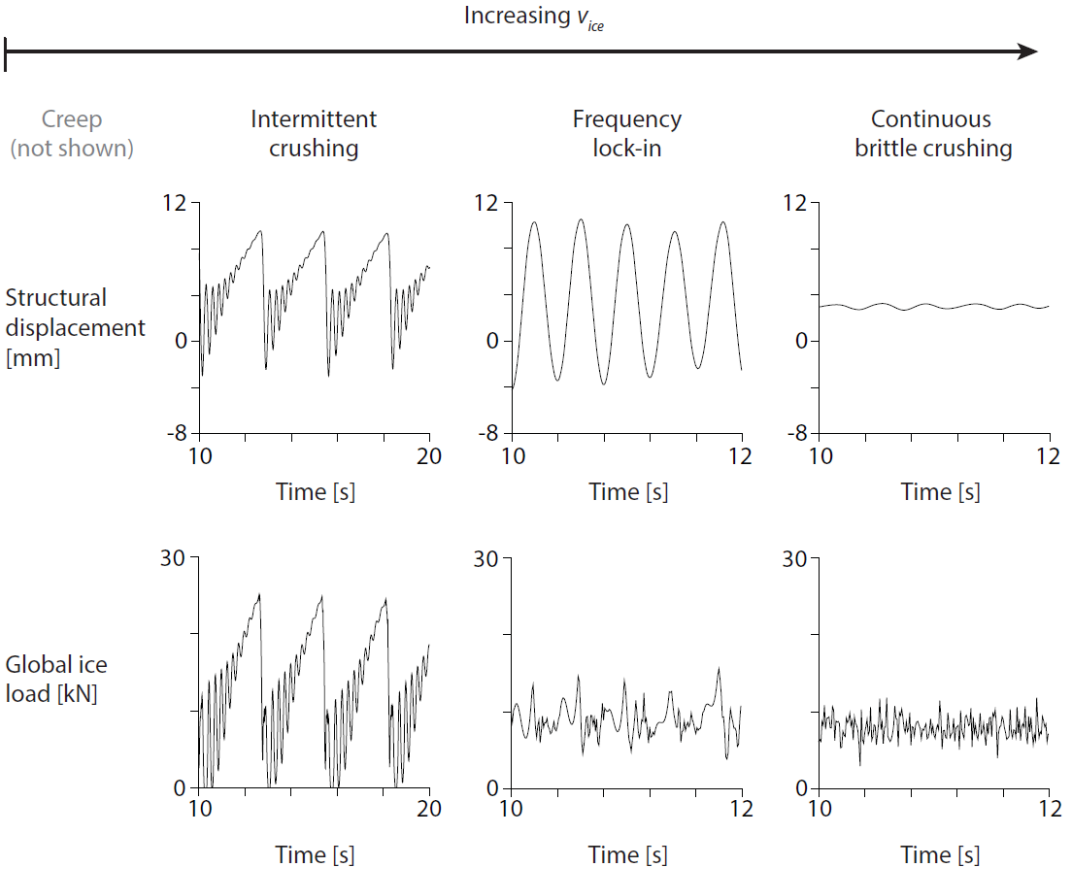

Figure 3.15: Illustration of ice-induced vibration regimes with structural displacement and ice-induced global load time signals of expected relative shape and magnitude from Hendrikse (2017). The values marked were computed from numerical simulations and should be regarded as relative and not actual (Hendrikse 2017).

According to Sodhi (2001), a major aspect of this ice-structure interaction is the large range of relative velocities between the ice and structure. Causing the significant range in relative ice-structure velocity is the ice-structure interaction cycle, which is separated into three phases. The first phase is the loading phase,

where relative velocity is low and the structure is gradually displaced and loaded by ice that is deforming in a mainly ductile manner. The second phase involves simultaneous ice crushing failure and subsequent, rapid movement of the structure into the ice sheet; the relative velocity is high. During the second phase, the ice deforms with brittle behavior. The third phase entails movement of the structure away from the ice sheet during structural oscillation, which results in a low or almost zero load on the structure as ice-structure contact is lost; the relative velocity is again low. Assuming that the failure length of the ice sheet is greater than the amplitude of structural oscillation, the structure will oscillate near one of its dominant natural frequencies until the structure regains contact with the ice sheet.

To better visualize the interaction cycle and introduce the effect of local ice-structure contact on the intermittent crushing regime, Figure 3.16 presents an example of ice-induced global load and contact area time series with labeled instances of interfacial pressure distributions. Note that this example comprises specific ice and structural properties but is considered representative of the intermittent crushing regime for the purpose of explanation. As described by Hendrikse (2017), and in agreement with Sodhi (2001), the first phase of the interaction cycle begins with instant **A** where relative ice-structure velocity is low and ductile ice deformation permits increase in contact area and mean interfacial pressure. The second phase corresponds with instant **B** when local brittle fracture begins as a consequence of maximum deformation exceedance in a HPZ. This initial fracture triggers a cascading effect as local ice failure sheds load to other HPZs that then fail in a local brittle manner. The failing ice sheet reduces the global load on the structure and allows movement of the structure into the ice sheet and towards the equilibrium position, increasing the relative velocity. Prior to the third phase, instant **C** marks the decrease in global contact area from the essentially simultaneous failure of the ice sheet. Again, depending on the failure length of the ice sheet, the structure either oscillates about its equilibrium position until it regains contact with the ice sheet or the structure maintains contact with the ice sheet during its oscillations and causes brittle fracture of the ice sheet while relative velocity remains high. The cycle restarts once the relative velocity is sufficiently reduced.

Assuming homogeneous ice sheet properties, the interaction cycle—or saw-tooth pattern—frequency is governed by the ice velocity and increases with increasing ice velocity until another ice-induced vibrations regime dominates (Sodhi 2001). After global ice failure when the global contact decreases substantially, the ice-structure interaction is influenced by the dynamic structural properties as well as the ice properties (Hendrikse 2017). Moreover, Hendrikse (2017) states that the ratio between ice-induced global load and structural stiffness governs the structural displacement amplitude, which grants describing the intermittent crushing regime as a quasi-static interaction.

3.2.2. FREQUENCY LOCK-IN

The frequency lock-in regime of ice-induced vibrations is achieved for a range of ice velocities greater than that for the intermittent crushing regime and for flexible structures with relatively low damping and natural frequencies (Hendrikse 2017). The range of ice and structural properties for which frequency lock-in may occur is not completely known; the reader is referred to the experiments by Huang et al. (2007) as well as the experimental and numerical tests by Hendrikse (2017) for more information.

As displayed in Figure 3.15 for the frequency lock-in regime, the structural displacement appears nearly harmonic and oscillates at slightly below one of the natural frequencies of the structure (Hendrikse 2017). According to Hendrikse (2017), the sinusoidal harmonic displacement of the structure experiences an aberration at the instant of global ice failure due to ice presence obstructing the structure from returning to its equilibrium position. The cause of the ice-structure interaction process for the frequency lock-in regime is primarily attributed to the relative velocity between the advancing ice sheet and the oscillating structure (Hendrikse 2017). This relative velocity influences the local failure behavior of the ice, which then affects the contact area and global load on the structure. The following description of the ice-structure interaction process for the frequency lock-in regime, referred to as the frequency lock-in cycle, is based on the observations from the forced vibration experiments by Hendrikse (2017); it is assumed that the details from tests with specific conditions are representative of the frequency lock-in regime in general.

Based on Figure 3.17, the first phase of the frequency lock-in cycle starts at instant **A** with recent global ice failure and soon rapidly increasing relative velocity that induces local brittle ice failure. The local brittle ice failures occur in HPZs with no correlation between local forces. Instant **B** indicates the transition from local brittle to more ductile failure behavior of the ice when the relative velocity decreases below some threshold. This transitional brittle-ductile ice failure behavior permits an increase in mean contact area and mean pressure, which result in more correlated local forces and a ice-induced global load greater than that for local

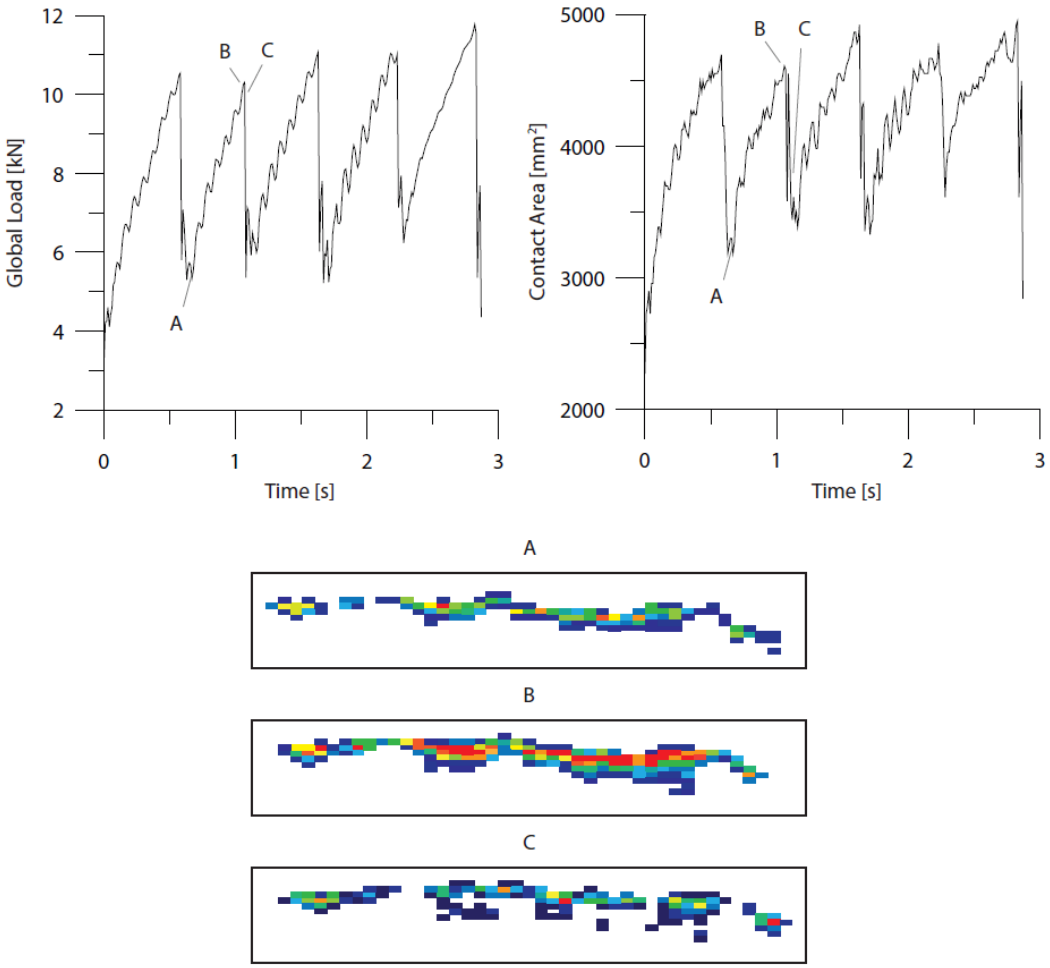

Figure 3.16: Global load and contact area time series of model structure and corresponding instances of interfacial pressure distributions from Hendrikse (2017) according to the experiments from Määttänen et al. (2012). Legend for pressure color scheme: blue - low pressure; red - high pressure.

brittle failure. As the relative velocity again begins to increase, the transitional ice failure behavior is superseded by brittle behavior and global failure by fracture occurs after a peak global load marked by instant **C**. For this example, the relative ice-structure velocity never becomes negative, i.e. the structure during its oscillation away from the ice sheet never moves faster than the ice velocity. Consequently, the structure does not lose contact with the ice sheet.

Figure 3.18 illustrates the change in contact area and mean pressure during the interaction process in the frequency lock-in regime with specific instances of the interfacial pressure distributions. Similarly to Figure 3.17, instant **A** marked on the contact area and contact pressure time signals refers to the moment immediately after a significant global ice failure event; only several points contact are present, and with low to medium pressure. Chronologically, but not alphabetically, instant **D** demonstrates an example of peak contact area and pressure during local brittle failure behavior when the majority of the pressure is concentrated within the HPZs (within the A–B region from Figure 3.17). The initial predominance of ductile ice behavior is indicated by instant **B** (same as in Figure 3.17) where the contact area is fairly large and some pressure zones of medium to high magnitude are beginning to form. For instant **C**, which is the same in meaning for both Figure 3.17 and Figure 3.18, the pressure distribution shows large regions of high pressure that transfer a larger global ice-induced load than that from instant **D**. This difference between pressure distributions from brittle (instant **D**) and ductile (instant **C**) ice behavior can be observed in the pressure histograms in Figure 3.18.

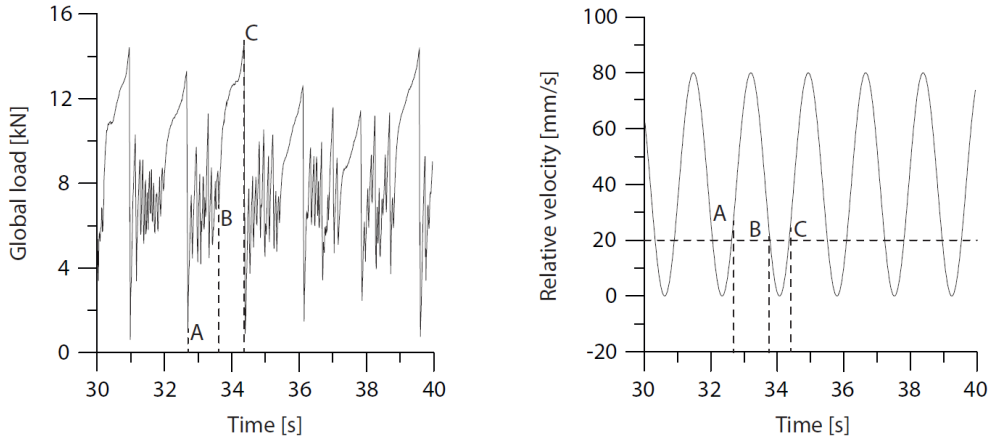

Figure 3.17: Ice-induced global load and relative velocity time signals of model structure according to forced vibration experiments from Hendrikse (2017). For region A–B, brittle ice behavior governs failure; for region B–C, ductile ice failure behavior is predominantly present.

FREQUENCY LOCK-IN RELATION

As summarized by Hendrikse (2017), a nearly linear relationship between the constant ice sheet velocity and the maximum structural velocity per frequency lock-in cycle is observed during frequency lock-in. The relation can be defined as follows:

$$\dot{u}_{max} = \beta v_{ice} \tag{3.1}$$

where $\dot{u}_{max}$ is the maximum structural velocity during a frequency lock-in cycle, β is an empirical coefficient which has been observed to be not exclusively between 1.0 and 1.5, and v_{ice} is the ice sheet—or indentation—velocity. According to Hendrikse (2017), no clear explanation for this relation is known. A conjectural method was made by Ziemer & Hinse (2017) to estimate the range of ice velocities for which frequency lock-in could develop based on one frequency lock-in event for a given structure. However, this method does not provide a substantiated explanation for the frequency lock-in relation.

3.2.3. CONTINUOUS BRITTLE CRUSHING

The continuous brittle crushing regime is observed for high ice velocities greater than those for intermittent crushing and frequency lock-in regimes and for all types of compliant structures (Hendrikse 2017). Figure 3.15 shows that, for the continuous brittle crushing regime, the ice-induced global load is seemingly random and fluctuates about a constant mean value, assuming a homogeneous ice sheet (Hendrikse 2017). Additionally, the amplitude of structural displacement is relatively small and similar in response to a structure acted on by an aperiodic load (Hendrikse 2017). Overall, the maximum global load and structural displacement in the continuous brittle crushing regime are much smaller that those in the intermittent crushing and frequency lock-in regimes; notably, there is little ice-structure interaction in the continuous brittle crushing regime.

3.2.4. ICE-INDUCED VIBRATIONS AND BUCKLING

For a compliant structure, the development of ice-induced vibrations were witnessed during the mixed ice crushing and buckling failure mode. For full-scale observations on the Norströmsgrund lighthouse, a combination of crushing, buckling or bending, and splitting (not considered in this study) was seen (Bjerkås et al. 2013). And for model-scale experiments with a flexible structure, crushing failure was frequently interrupted by bending and buckling failure (Ziemer & Evers 2014).

Additionally, Hendrikse & Metrikine (2016*b*) conducted a numerical investigation of ice-induced vibrations with ice buckling failure as a limiting mechanism. As proposed by Kerr (1978), the wedge beam on a Winkler foundation approach was selected by Hendrikse & Metrikine (2016*b*) and implemented in the phenomenological model. It was concluded, based on specific ice and structural properties, that ice-induced vibrations could ensue given that buckling failure does not happen within a cycle of intermittent crushing or

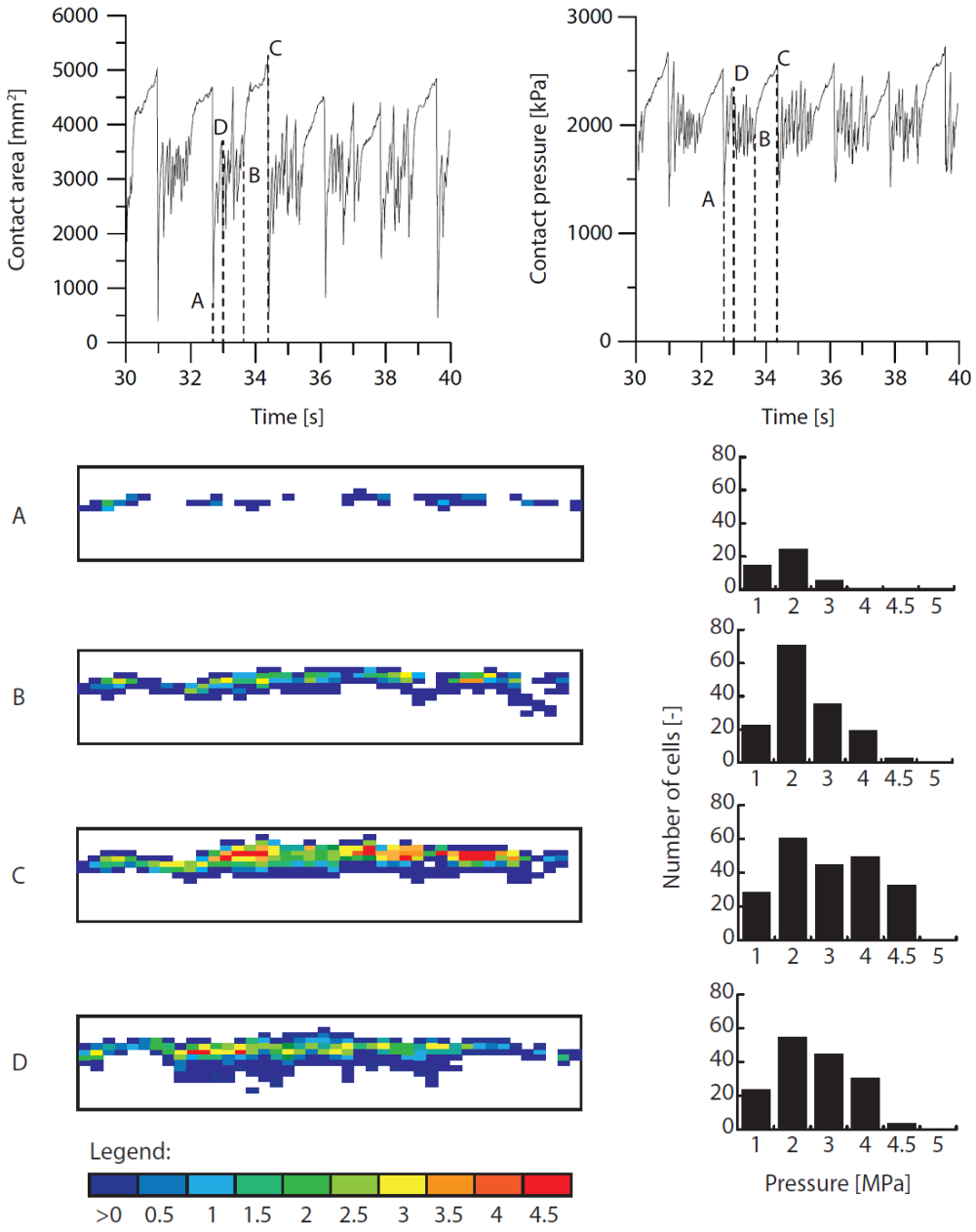

Figure 3.18: Contact area and contact pressure time signals of model structure with corresponding instances of interfacial pressure distributions according to experiments from Hendrikse (2017).

frequency lock-in. An increase in ice velocity and increase in aspect ratio are each predicted to increase the frequency of buckling failure. For the numerical investigation, a special case was found for a flexible structure where intermittent crushing prevented buckling failure which would have otherwise occurred for a rigid structure; the details of this non-limiting mechanism are offered in Hendrikse (2017).

Regarding the ice and structural properties involved in the ice-structure interaction, the cross-sectional geometry of the structure seems to play a much more important role in mixed ice crushing and buckling failure mode than in other failure modes (besides buckling failure by itself). This may be especially apparent for a compliant structure when ice-induced vibrations can be interrupted or perpetuated by buckling failure.

An interesting finding by Willems (2016) about ice-induced vibrations and buckling was that the frequency lock-in regime developed at lower ice velocities for a circular cross-section structure than for a rectangular cross-section structure of equivalent width. This conclusion was based on numerical simulations from the adapted phenomenological model as mentioned in Section 3.1.5. Nevertheless, Willems (2016) justified

the result by explaining that the ice-induced global load in the direction of ice motion is lower in general for the cylindrical structure than for a structure with rectangular cross-section of equivalent width. It was stated that if the frequency of ice-structure interaction remains constant, then the maximum structural velocity per frequency lock-in cycle increases with increasing ice-induced global load on the structure (Willems 2016).

4

DESCRIPTION OF EXPERIMENTS

As part of the IVOS (Ice-induced Vibrations of Offshore Structures) project from January 2015 until December 2016, myriad experiments with model-scale structures were conducted in the Large Ice Basin at the Hamburg Ship Model Basin (HSVA). The experiments deployed rigid and compliant single-degree-of-freedom test systems with a multitude of configurations regarding ice and structural properties. The many tests were divided into two phases; the second phase tests, referred to as the Phase 2 tests, are of specific interest to this study. Included in the Phase 2 tests were structures each with circular and rectangular cross-section. Additionally, the ice and structural properties from the tests were sufficiently similar that comparison between the structures of different cross-sectional shape is viable. Note that the author did not partake in the design of the experiments, but did assist in recording measurements during tests in December 2016. A general description of setup and conditions from the Phase 2 tests are given in Section 4.1. This is followed by Section 4.2, which comprises a scrutiny of the tests that are analyzed in this study.

4.1. COMPLIANT TEST APPARATUS

The compliant test apparatus from the IVOS Phase 2 tests is elaborated according to the IVOS progress reports by Hinse et al. (2017), Ziemer (2016), the published article by Ziemer & Hinse (2017), and observations from the author. The test setup was designed to be versatile and ergonomic such that the many structural properties of the system could be changed easily and rapidly. Also, it was decided that passive loading on the system would be applied, the definition and details of which are offered in Section 4.1.6.

A general schematic of the test setup is shown in Figure 4.1. Starting from the bottom and moving sequentially upwards, the major components of the test apparatus are listed with their marked color as follows: the model structure in light blue, the 6-component scale in green, the compliant basis in yellow, the system springs in black, and the main carriage in brown. To avoid confusion, it is important to note that the working platforms (also in green) and the support structure (in grey) are considered part of the main carriage. Moreover, the additional weights (in light green) are included in the compliant basis. The major components of the test setup are discussed in the following sections.

4.1.1. MODEL STRUCTURES

The purpose of each model-scale structure was to accept and transmit the ice action to the test system. Various model-scale structures were implemented during the Phase 2 tests. A summary of the cross-sectional geometry, size, and the specific test runs for each structure is depicted in Figure 4.2. Note that the structures of rectangular cross-section in fact only have three sides. It may be assumed that this has no impact on the ice-structure interaction since the missing side faces away from the direction of ice motion.

The model structures by themselves, in terms of the test system, were designed to be rigid and therefore were not supposed to deflect, vibrate, or deform during ice-structure interaction. All of the structures were inherently rigid in design except for the structure of 120 mm diameter, which required a stiffening bracket. Note that the stiffening bracket was added such that the 120 mm diameter model structure would be sufficiently rigid in the artificial full-scale ice, which was much stronger than the model-scale ice and thus would exert much greater loads on the structure. Under the assumption of sufficient rigidity, bending of the struc-

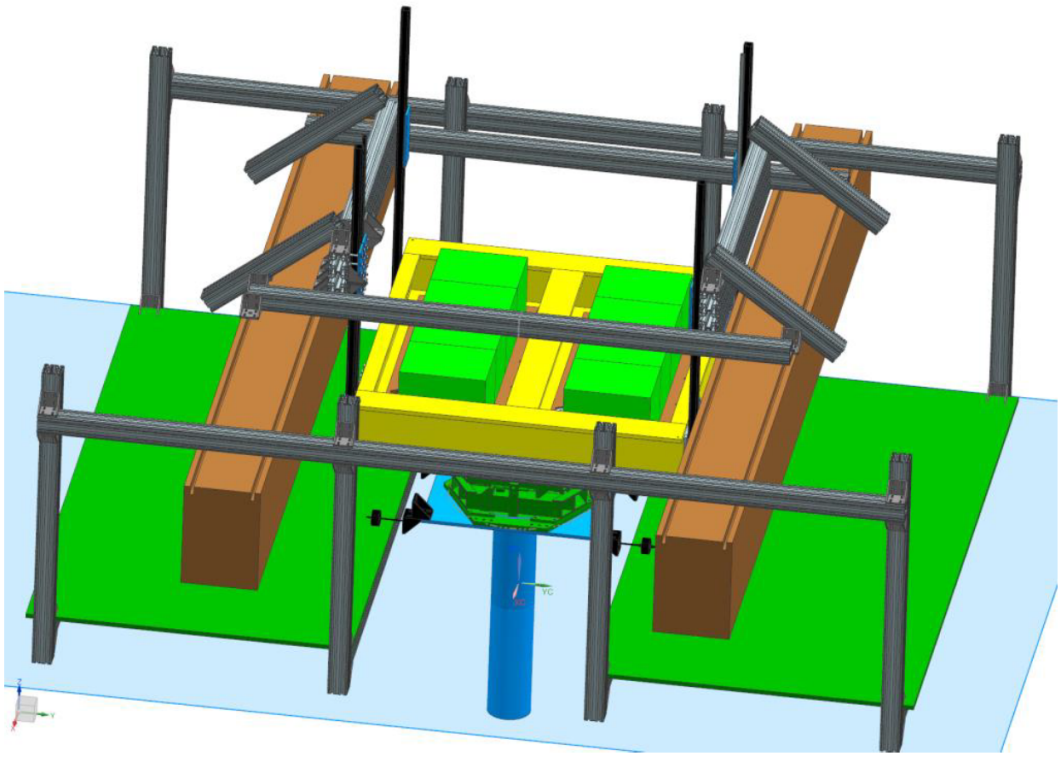

Figure 4.1: Schematic of IVOS Phase 2 test apparatus from Hinse et al. (2017).

ture from the base—connected to the 6-component scale—to the ice-structure interface, near the waterline, should not occur.

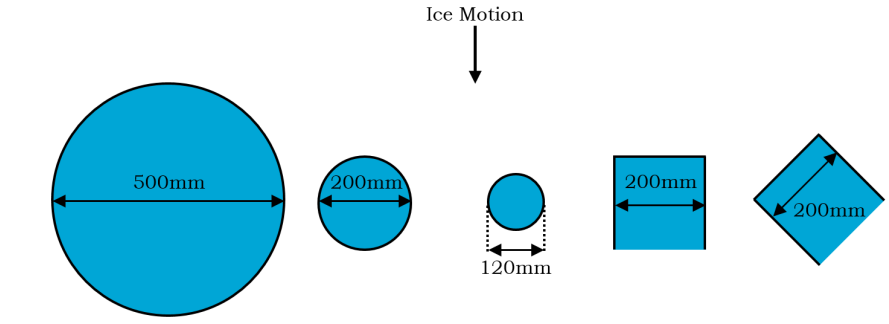

Test Runs					
	21010	22010	24010	25010	26010
	21011	22110	24020	25011	
	21020	22120	24021	25012	
	23020	23010	27010	25020	
			27020	26020	
			27030		

Figure 4.2: Schematic of IVOS Phase 2 test model structure cross-sections, size, and relevant test runs. For the complete test matrix, refer to Appendix A.

4.1.2. 6-COMPONENT SCALE

The 6-component scale connected the model structure to the compliant basis and comprised a load cell sandwich. It was affirmed by Hinse et al. (2017) that model structures were easily exchangeable based on the designed connection between the model structure and 6-component scale. The 6-component scale measured in-plane and out-of-plane forces from the ice action that were transmitted from the model structure. As stated by Ziemer (2016), the 6-component scale demonstrated a stiffness of about 4500 N/mm; a rule-of-

thumb for rigidity is the stiffness of the rigid component should be at least two orders magnitude greater than that of the flexible component. Therefore, the compliance of the 6-component scale cannot be neglected forthright in this study. Discussion of the flexibility of the 6-component scale is provided in Section 4.1.8.

4.1.3. COMPLIANT BASIS

The compliant basis acted as the means to create a single-degree-of-freedom system by carrying the mass of the model structure, 6-component scale, and additional weights and by transferring the ice action from the model structure to the system springs. The additional weights that were located on the compliant basis could be swiftly and easily changed to tune the mass of the system. The compliant basis was deemed rigid for the tests.

4.1.4. SYSTEM SPRINGS

The test system utilized bending rods with rectangular cross-sections as the system springs in order to grant the desired stiffness for the system. According to Hinse et al. (2017), six types of rods with different sizes were available for individual or parallel combinations for grossly tuning the stiffness of the system. Moreover, the stiffness of the system parallel and perpendicular to the direction of ice motion was designed to match. Fine tuning of the stiffness by altering the length of the rods was discouraged by Ziemer (2016) as the process was laborious and slow. Furthermore, the change in length of the bending rods would result in a change in the submerged volume of the model structure, thereby altering the added mass of the system. According to HSVA, it is important to note that the bending rods provided stiffness for the system that was not entirely linear, and the nonlinearity of the stiffness was exacerbated with increasing displacement. As an aside, Ziemer & Hinse (2017) confirmed that the high frequency vibrations from the main carriage could not be transferred to the compliant basis because of the damping of the bending rods.

4.1.5. MAIN CARRIAGE

The system springs connected the compliant basis to the support structure and therefore the main carriage. More specifically, the support structure was attached to the moon pool of the main carriage, all of which were considered rigid for the testing. The working platforms facilitated in situ modifications to the test apparatus. The main carriage is a large, mobile structure that traverses the Large Ice Basin on a railway system and was the means of providing passive loading on the system, which is described in the following section.

4.1.6. LARGE ICE BASIN

The Large Ice Basin at HSVA comprises a specialized refrigerated towing tank with the capability of preparing a floating ice sheet for, in the case of this test campaign, ice-structure interaction with model-scale structures. For the IVOS Phase 2 tests, each model structure was propelled by the main carriage through a stationary ice sheet in the Large Ice Basin; this method is denoted as passive loading. One of the major benefits of utilizing passive loading was that splitting failure caused by radial cracking that propagated to a free surface or edge was highly improbable because the ice sheet was kept frozen to the walls of the basin and thus no free edge was provided (Ziemer & Hinse 2017). Note that passive loading entails an indentation velocity of the model structure into an immobile ice sheet and not an ice drift velocity of the ice sheet against a stationary structure. In terms of relative motion, these cases are synonymous and henceforth are treated as such.

ICE SHEET FORMATION

Two different types of ice sheets were prepared during the IVOS Phase 2 tests: model-scale ice and artificial full-scale ice. Specifically, seven model-scale ice sheets and one artificial full-scale ice sheet were created. The method to form the model-scale ice sheet first involves a wet seeding process where a saline solution is sprayed into the air by applicators on the main carriage as the carriage moves through the basin. Hours prior to the seeding, the refrigeration system had cooled the basin to about -18°C; the saline mist freezes and is deposited on the surface of the water to begin the formation of columnar ice. Further description of the process are provided by Evers & Jochmann (1993), Määttänen et al. (2012), Ziemer & Evers (2014) since the author was not present for the entire duration of the formation. However, once the ice sheet begins to form, the edges of the ice sheet are cleared from the sides of the basin. This technique is intended to reduce the accelerated freezing caused by the colder sides of the basin and make the ice sheet more uniform in thickness.

Note that the ice sheet does in fact refreeze to the sides of the basin, but intentionally with less ice thickness than an uninterrupted ice sheet formation.

Although very interesting, the creation and experimentation of the artificial full-scale ice sheet is not discussed because the tests which implemented this ice are not relevant to this study. The reader is referred to the description by Hinse et al. (2017) for more information.

For all of the ice sheets, the ice thickness, compressive strength, and flexural strength were measured for multiple locations along the length of the basin. The methods are generally mentioned by Ziemer & Evers (2014) and given in detail by Hinse et al. (2017).

4.1.7. SENSORS

Besides the load cell sandwich of the 6-component scale, many other measurement devices were utilized in the Phase 2 tests. According to Ziemer (2016), accelerometers were mounted on the model structure, compliant basis, and the main carriage and recorded accelerations of the system. Displacement of the model structure in the direction of ice motion was measured via laser sensor that was attached to the main carriage. The overall motion of the compliant basis was monitored by a Qualisys optical motion capture system. The velocity and displacement of the main carriage were also recorded. Finally, each model structure was equipped with TekScan I-Scan tactile sensors at the ice-structure interface in order to record local contact areas and pressures. For the majority of the test runs, the model structure was equipped with two tactile sensors: a large tactile sensor that was intended to capture capture ice crushing events along the entire ice-structure interface; and a small, detailed tactile sensor that was meant to record local ice crushing events around the front central portion of the ice-structure interface.

All of the sensors, except for the tactile sensors, recorded and sent data to a single data acquisition device. Because the tactile sensors required a separate data acquisition system, the data were saved in a separate format. This topic is further addressed in the next chapter.

4.1.8. DISCUSSION OF COMPLIANT TEST APPARATUS

In accordance with Hinse et al. (2017), Ziemer (2016), the test setup in general was proven to be functional and satisfactory for the intended purpose. However, some design considerations and application of sensors need to be addressed for better understanding of the data collected during the experiments.

First and foremost, the flexibility of the 6-component scale can disrupt the validity of the single-degree-of-freedom system. For example, if a certain amount of ice-induced force is applied to the model structure, then the system springs will deflect and grant an aspired displacement of the compliant basis in the direction of ice motion. Of course, the load cells of the 6-component scale deflect during testing, but it is assumed that the deflection is sufficiently small compared to that of the displacement of the compliant basis. But if the ice-induced force is sufficiently large, then the 6-component scale could severely deflect and the model structure would rotate about the 6-component scale and introduce another degree of freedom. This degree of freedom of the system was observed for each model structure during the relaxation tests, the definition of which is afforded in the following chapter. During the design of the test apparatus, HSVA reported that the 6-component scale would afford this degree of freedom; however, the tactile sensors required comparison to another measurement system in order to be calibrated. It was decided by Ziemer (2016) that this unwanted degree of freedom was not dominant and therefore neglected so that testing could continue as planned. The author has some reservations about this design decision but recognizes the difficulty of combating the issue. Moreover, the presence of the undesirable degree of freedom was not severely apparent in the data from the experiments.

Given this potential rotational degree of freedom for the model structure, the measurements of laser displacement sensor may have been distorted. The laser measured the distance from the surface of the model structure to a supposedly fixed point. In actuality, the laser was attached to an aluminum fixture, which was then connected to the main carriage. During testing, the main carriage vibrated while moving, which transferred motions to the laser via the non-rigid aluminum fixture. As explained by HSVA, constructing a fully rigid fixture for the laser was not economically feasible. If the rotation of the structure about the 6-component scale occurred, then the measurements by the laser include both the displacement of the compliant basis and the rotation of the model structure. Furthermore, flexibility of the setup in general could have originated from the base plates, the bolted connections between main components, and other sources, according to HSVA. Too much uncertainty of the system was present for potential correction for this rotation—as well as general flexibility—to be performed; regardless, this topic should not be neglected altogether.

Because the 6-component scale was positioned within the single-degree-of-freedom system, the load cell sandwich recorded, in addition to ice-induced forces, inertial forces presumably from the mass of the model structure, added mass of the submerged volume of the structure, and added mass from the ice. A technique to treat this problem encompasses the force and acceleration measurements for the model structure and is discussed in the next chapter. But the accelerometer that was mounted on the base plate of the model structure—which was directly adjacent to the 6-component scale—only measured the in-plane accelerations at that location. Thus, the possible acceleration caused by rotation of the model structure about the 6-component scale could not be recorded.

It was discussed by Ziemer (2016) that the infrared signal of the Qualisys system caused disturbance in the laser displacement measurements during one of the tests. It is believed that this issue was resolved and is not discussed further. In terms of signal processing, noise was discovered within the majority of experimental data, especially the accelerometers and tactile sensors, upon cursory inspection. This subject is detailed in the following chapter.

Several problems regarding ice properties were witnessed during the Phase 2 tests. In general, downward bending of the ice was observed during the majority of the experiments. This topic is thoroughly described by Hinse et al. (2017) and served as one of the main motivations for the artificial full-scale ice sheet. Each ice sheet was created in the attempt to achieve specific, homogeneous ice properties; unfortunately, this was not normally the case. The properties of the ice varied considerably throughout the ice sheet without an obvious explanation, even though the control variables for preparing the ice sheet were monitored vigilantly. Nonetheless, the scatter in ice properties was typical for model-scale ice as observed by HSVA.

4.1.9. RIGID TEST APPARATUS

In addition to the compliant test setup, a rigid test apparatus was designed and implemented (see Figure 4.3). As shown in Figure 4.3 and explained by Hinse et al. (2017), the model structure was attached to a massive steel beam that was directly connected to the main carriage via adapter plates. Tactile sensors were placed on the model structure in the same manner as previously stated, and accelerometers and the laser displacement sensor were mounted on the system to verify rigidity. The 6-component scale was omitted due to the problem of compliance; therefore, ice-induced loads needed to be computed from the tactile sensors. Deployment of the apparatus proved that the setup was not fully rigid but experienced structural displacements that were a factor of six less than those from the equivalent compliant test apparatus (Hinse et al. 2017). Ideally, a fully rigid test apparatus would experience structural displacements two orders of magnitude less than those of the equivalent compliant test setup.

4.2. DESCRIPTION OF RELEVANT TESTS

Based on the objectives for this study, test runs were distinguished which contained structures of circular and rectangular cross-section, similar ice and structural properties, and ice-induced vibrations in the frequency lock-in regime. Summarized in Table 4.1 is the test matrix for the selected test runs based on Hinse et al. (2017), Ziemer (2016). Note that the model structure with circular cross-section was used during the 23010 test run (see model structure in Figure 4.1) and the model with rectangular cross-section was deployed for the 26020 test run (see model structure in Figure 4.4). Both structures had widths of 200 mm and were subjected to ice sheets with fairly similar ice properties. But the ice during the tests of the circular cross-section structure, with 25 % less flexural strength than the ice from the tests with the rectangular cross-section structure, was observed to be substantially more prone to the downward bending and buckling failure.

The range of indentation velocities tested for each structure was similar enough but the exact velocity increments applied were not the same. From Hinse et al. (2017), Ziemer (2016), the stiffness of the system for each test run was nearly alike; this is reviewed by the author in the next chapter. Finally, a percent difference of about 7 % in natural frequency between structures is large enough to warrant concern; this difference as well as the adequacy of similarity between test runs are addressed in Chapter 6.

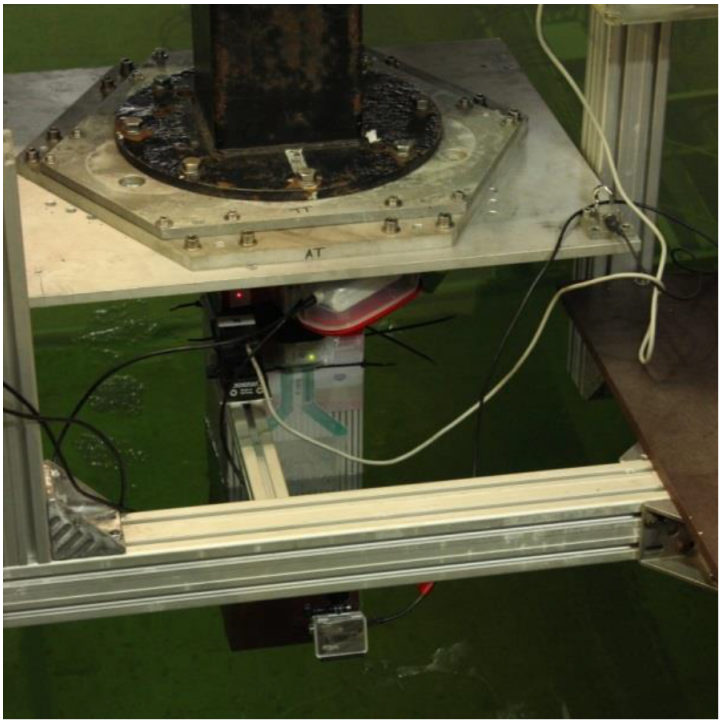

Figure 4.3: Photograph of rigid test apparatus during 25020 test run from Hinse et al. (2017).

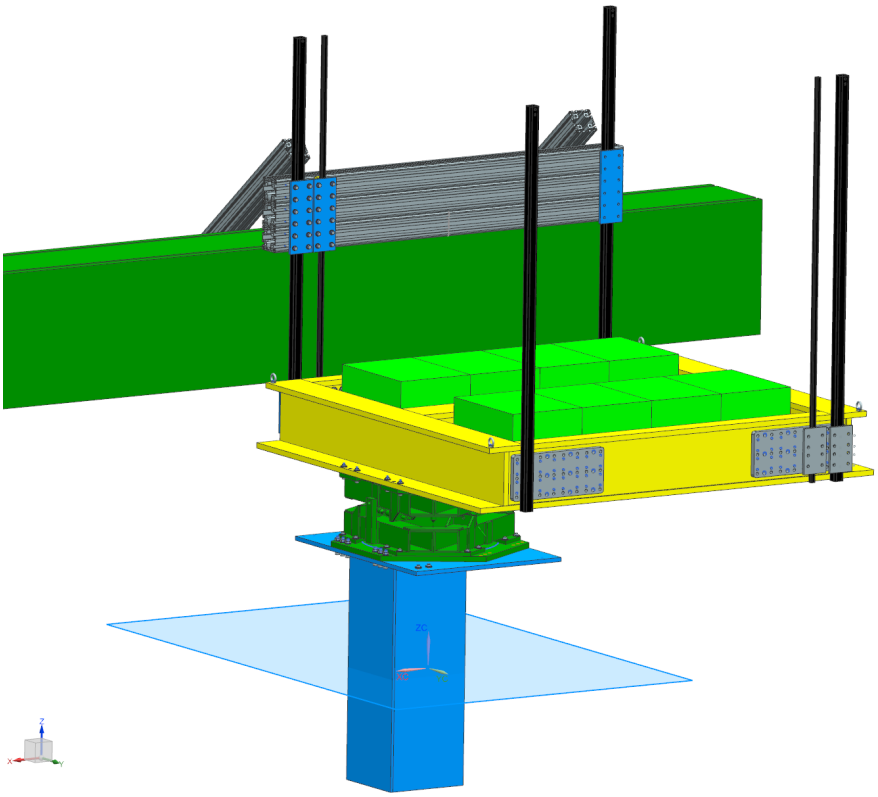

Figure 4.4: Schematic of compliant test apparatus with model structure of rectangular cross-section from Ziemer & Hinse (2017).

Table 4.1: Test matrix for 23010 and 26020 test runs from Hinse et al. (2017), Ziemer (2016).

Series	**Test Run**	**Diameter [mm]**	**System stiffness [N/mm]**	**Natural frequency [Hz]**	**Ice thickness [mm]**	**Ice flexural strength [kPa]**	**Ice compressive strength [kPa]**	**Indentation velocity [mm/s]**
23000	23010	200	1930	5.8	43	45	97	5-9 (2 mm/s steps); 10-20 (5 mm/s steps); 30-50 (10 mm/s steps); 70 100 150
26000	26020	200	1950	5.4	45	60	110	3-50 (1 mm/s steps); 60-80 (10 mm/s steps); 100 150

5

EXPERIMENTAL DATA POST-PROCESSING

The data collected during the IVOS Phase 2 tests required post-processing prior to analysis of the results. Given the large quantity of data and the limitations of the previous analytical software, it was decided that ergonomic tools in the software MATLAB would be developed for signal processing as well as data manipulation and analysis. To facilitate the design of these tools, a database was created with uniform data file format and intuitive nomenclature.

This chapter explains the methodology and application of the post-processing techniques, beginning with the development of the database in Section 5.1. Next, the various signal processing methods that were implemented in this study are reviewed in Section 5.2. Then, in Section 5.3, the pertinent structural properties are determined from the relaxation tests of the respective test runs. A means of computing ice-induced global loads from the uncalibrated tactile sensors was attempted; this is discussed in Section 5.4. Ultimately, the post-processing and recapitulation of pertinent data for the following analysis is presented in Section 5.5.

5.1. DATABASE

The data from the IVOS Phase 2 tests were collected using two different data acquisition systems: one system consisted of the laser displacement transducer, accelerometers, Qualisys optical motion capture system, and load cells from the collective main carriage, compliant basis, 6-component scale, and model structure; the other system consisted of the TekScan I-Scan tactile sensors mounted on the perimeter of the model structure at the ice-structure interface. For simplicity, the following terminology is conferred on each of the two systems: 6-component scale (6COMP) for the former system and tactile sensor (TAC) for the latter system. To create the database, the data collected by the 6COMP and TAC systems had to be converted into uniform file formats.

Data from the 6COMP system were saved as comma-separated value (CSV) files, which were too large and cumbersome to analyze in Microsoft Excel. Therefore, a tool was made to convert the 6COMP data format from CSV files to binary MATLAB files (MAT-files). It is important to note that these data include both the test runs and their corresponding relaxation tests. Data from the TAC system were originally collected via the Tekscan I-Scan software. The valuable data were extracted from the TAC system data by manually truncating data sets and exporting from Tekscan I-Scan to CSV files; the process was tedious and time-consuming. Then the TAC system CSV files were converted to MAT-files by utilizing a tool; the process of converting all of the files was automated but computationally expensive.

To summarize, both the 6COMP and TAC system data for all test runs from the IVOS Phase 2 tests were successfully converted into MAT-files with explicit nomenclature that were readily loaded into MATLAB for further manipulation. Due to the size of the TAC system data files, the loading time can be on the order of one minute; this loading time can be reduced by applying a sparse matrix technique to the TAC data. This method has not yet been implemented but is recommended.

5.2. SIGNAL PROCESSING

The data, as recorded by the data acquisition systems, were not suitable for analysis; therefore, certain signal processing techniques were applied to specific data sets as deemed appropriate. The signal processing meth-

ods are defined generally in the following sections and later utilized for the test runs that are relevant to this study. Application of the signal processing is discussed in a later section.

5.2.1. OFFSET ADJUSTMENT

At the beginning and end of every test run was some duration with no activity, meaning that measured forces, accelerations, displacements, etc. should have been negligible or nil. In the case when this duration with no activity yielded unexpected non-zero measurements, the mean of the given duration was computed as an offset and then subtracted from the original signal such that the offset signal was zeroed. An offset in a signal can have numerous causes such as change in internal stresses in the sensors from temperature gradients, but the most common reason—according to HSVA—is usually that the data acquisition system chooses a zero point at an instant with non-zero measurement.

5.2.2. TRUNCATION

In terms of signal processing, truncation refers to the selection of a specific portion of a signal and disregard of the remainder of the signal. This simple technique expedites general post-processing computations with the selection of smaller data sets and benefits the signal time-synchronization method that is detailed in Section 5.4.

5.2.3. DIGITAL FILTERING

In terms of signal processing, recognizable noise was discovered in the unprocessed data from both 6COMP and TAC systems, which needed to be mitigated prior to further manipulation and analysis of the data. The most pervasive noise observed in the data, especially in the tactile sensor and acceleration data, was 50 Hz fluctuations and corresponding harmonics from the power source. Knowing that the majority of macroscopic ice crushing events and structural responses occurred with a frequency of less than 50 Hz, the low-pass filter design was chosen as means of generally attenuating noise for frequencies above 50 Hz. Based on the uncertainty in the efficacy of the filters in MATLAB for this particular task, a comparative evaluation of three common filters was performed. This assessment is described in the following sections and entailed selecting a noisy sample signal, performing filtering using three different low-pass filters, and assessing the filtering based on spectral analysis and comparison among the filtered signals. First, the definition of spectral analysis is offered, then the filters are described. After, the filters are compared and lastly a filter is selected for further post-processing of the data.

SPECTRAL ANALYSIS

To isolate the noise within a signal, the power spectrum of the signal was computed by means of fast Fourier transform (FFT) algorithm. The FFT algorithm, as defined and implemented by the MATLAB default function, discretely converts the signal from the time domain to the frequency domain. The relevant portion of the signal in the frequency domain was then used to compute the power spectral density (PSD) function, which describes the distribution of figurative power, or energy content, of the signal over a discrete range of frequencies. The generalized discrete PSD function S_{xx} can be computed as follows:

$$S_{xx}(\omega) = \frac{2}{f_s L} |\hat{x}_{FFT}(\omega)|^2 \tag{5.1}$$

where f_s is the sampling frequency of the signal, L is the length of the signal, and $\hat{x}_{FFT}$ is the signal in the frequency domain from the FFT conversion. The range of frequencies ω is defined from zero to the Nyquist frequency, or simply half of the sampling frequency. The power content from $\hat{x}_{FFT}$ only includes half of the total power of the original signal due to the selected frequency range; thus, the value of two is included in Equation 5.1. To demonstrate the purpose of the PSD function, a sample signal was selected which contained considerable noise and was relevant to this study. Specifically, a sample of unprocessed, uncalibrated normalized TAC global force signal from the test run of the rectangular cross-section structure was chosen. The method for determining the global force from the TAC system data is detailed in Section 5.4. As shown in Figure 5.1, the PSD function of the selected signal illustrates the presence of the noise at approximately 50 Hz, 100 Hz, and 150 Hz; the frequencies containing energy content from structural responses and ice crushing events are observed below 40 Hz. It is important to note that the energy content at zero frequency in Figure 5.1 is significantly larger than that at 50 Hz, but the ordinate of has been truncated for the purpose of visual comparison.

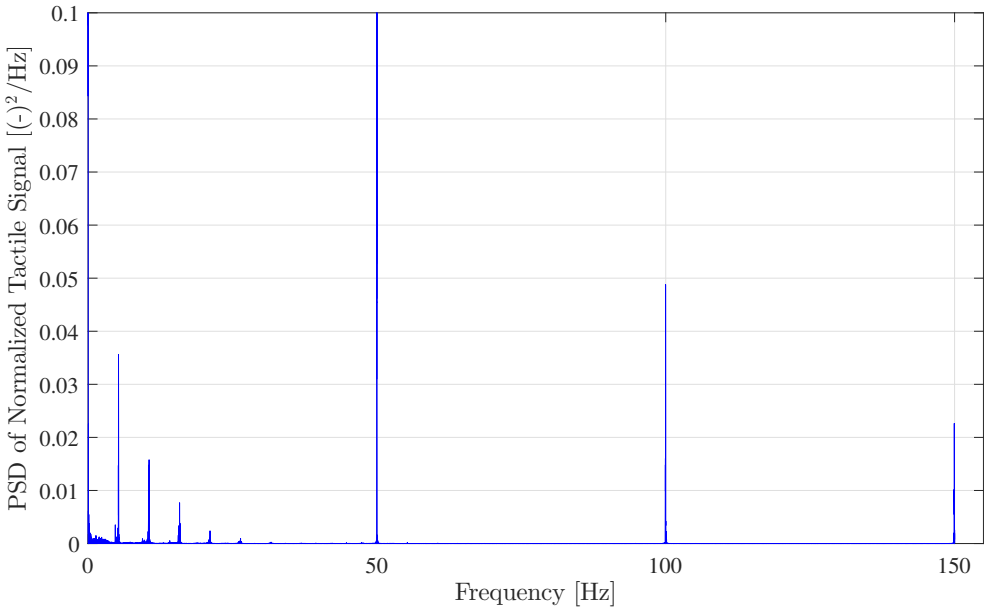

Figure 5.1: Power spectral density function for sample signal from 26020 test run. The ordinate is truncated for clarity.

Besides the frequencies observed with peaks of energy content, important statistical properties of mean and standard deviation (from variance) can be derived from the PSD function. These statistical properties, in addition to the peaks of energy content in the PSD function, can be compared to analyze the effect of a filter on the signal. The standard deviation σ_{xx} of the signal can be found from the PSD function using the following relation:

$$\sigma_{xx} = \left[\frac{1}{2} \sum_{n=2}^{F_{Nyq}} \left[S_{xx}(\omega_{n+1}) + S_{xx}(\omega_n) \right] (\omega_{n+1} - \omega_n) \right]^{\frac{1}{2}} \tag{5.2}$$

where F_{Nyq} is the aforementioned Nyquist frequency. Equation 5.2 utilizes trapezoidal numerical integration to approximate the standard deviation of the original signal from the PSD function. Note that the first discrete frequency, the zero frequency, is meaningless with respect to standard deviation but is important to the mean of the signal. The mean $\bar{x}$ of the signal from the PSD functio is computed as follows:

$$\bar{x} = S_{xx}(\omega = 0)\Delta\omega \tag{5.3}$$

where $\Delta\omega$ is the incremental frequency defined by the frequency range for the PSD function. The mean is invariant and therefore is represented by the zero-frequency energy content in the power spectrum. This explains the significant energy content at zero frequency in Figure 5.1 since the signal has a large value for the mean when compared to the standard deviation. Note that the selected signal needs to be a stationary process in order for the PSD analysis to be valid. A stationary process is defined as a stochastic process whose mean and variance do not change with time. This assumption is assessed within the PSD analysis; it is recommended that the signal be truncated if needed such that the examined signal becomes a stationary process.

DESCRIPTION OF FILTERS

Based on the spectral analysis, it was observed that noise was present in the unprocessed data from both systems for frequencies greater than 49 Hz; therefore, it was decided that the data should be filtered using this criterion. Three different filters were applied to the sample signal: a moving average, Butterworth, and Bessel filter. For both the Butterworth and Bessel filters, an undesirable phase shift was observed and then circumvented via zero-phase digital filtering. It is of note that application of the zero-phase digital filter doubles the order of the original filtering.

The generic moving average MATLAB default filter offered a fast and simple initial attempt to filter the signal but does not possess specific capabilities for low-pass filtering. Instead, the low-pass filtering is performed by a user-defined averaging window that is applied along the signal. When applied, the moving-average-filtered signal appeared to generally be reduced in peakedness from noise—as well as from the valuable data—and not incur a discernible phase shift. Because this filter cannot target specific ranges of frequencies, the filtering affects both the signal caused by the ice-structure interaction and by the noise.

The Butterworth filter provides a more specific low-pass filtering process with user-defined cutoff frequency (set to 49 Hz) and order, or magnitude, of filtering. Again, a MATLAB default filter was used after creating the filter design coefficients. A benefit of the Butterworth filter is the flat passband; i.e. with respect to power spectra, the power content below the cutoff frequency is unaffected by the filtering. But an issue with the Butterworth filter is the gradual attenuation of the unwanted power content above the cutoff frequency, which means that the highest power content at 50 Hz is attenuated the least of the reduced power content (the power content at 50 Hz is the greatest of the noise frequencies). The Butterworth filter cannot target the 50 Hz frequency without shifting the cutoff frequency to lower frequencies, which might remove power content from the measurements and not just from the noise.

The Bessel filter offers an order of filtering and a user-defined cutoff frequency (set to 49 Hz) with a nearly constant phase shift across the passband frequency and steeper attenuation of unwanted power content above the cutoff frequency. Also, a MATLAB default filter was used after creating the filter design coefficients and converting the coefficients from analog to digital format. This low-pass filter was previously used in filtering of laboratory test data at and was highly recommended by HSVA.

EVALUATION AND SELECTION OF FILTER

To evaluate the filters, the sample signal and the corresponding PSD function were determined. Then the filters were each applied separately to the sample signal, and the PSD function for each of the filtered signals was computed along with a statistical analysis of the PSD function. Finally, the standard deviation and mean values were compared between the original signal and the filtered signal from each filter. Furthermore, the percent reduction in energy content above 49 Hz from the PSD function of each filtered signal was compared (see Table 5.1). As displayed in Table 5.1, the order or span of the filter quantifies the magnitude of the filtering, i.e. more filtering is applied for a greater order or span. In the case of the moving average filter, the span is defined as the size of the window from which the filtering coefficients are determined and to which the low-pass filter is applied, and must be an odd number. For the Butterworth and Bessel filters, the order refers to the polynomial order of the low-pass filtering.

The mean of the signal is negligibly affected by the filtering, which is justified by the fact that the energy content of the mean is contained at zero frequency and therefore should not be influenced by frequency-dependent or averaging filtering. The standard deviation of the signal is markedly changed by the filtering, which is expected because the noise in the sample signal is severe in magnitude. In general, the different filtering noticeably reduces the quantity of energy content at the frequencies caused by noise. It is important to clarify that the energy content considered for above and below 49 Hz excludes the zero-frequency energy content, as this energy content comprises the majority of the total energy, does not change with filtering, and is thus not of interest for comparison.

Table 5.1: Comparison of the effect of the filters on the sample signal from the 26020 test run.

Filter type	Moving average	Butterworth	Bessel
Filter order	Span 5	Order 6	Order 6
Difference in mean [%]	0.0	0.0	0.0
Difference in std. [%]	32.4	25.8	33.5
Reduction in energy content above 49 Hz [%]	96.0	83.6	98.0

To select the most suitable filter to be used for further analysis, the aforementioned comparisons were made between the three filters based on difference in mean, standard deviation, and on reduction in power content above the selected cutoff frequency. For filter span and orders of similar magnitude, the filters affected the sample signal in a similar manner. But the Bessel filter demonstrated the greatest reduction of power content caused by noise while also altering the standard deviation of the filtered signal in a manner

that was comparable to that of the other filters. Hence, the Bessel filter was selected for all further data post-processing techniques implemented. Note that this design decision was made rather generally and may not be adequate for all types of data.

5.3. STRUCTURAL PROPERTIES FROM RELAXATION TESTS

Before each test run, a relaxation test was conducted to confirm the dynamical properties of the compliant test apparatus. A relaxation test is the free decay test of a dynamical system by means of an initial displacement. The compliant system is displaced some distance from equilibrium and then released almost instantly such that the system can oscillate freely. For each test run, a relaxation test was performed and the forces, accelerations, and displacements were measured by the 6COMP system. Note that the test apparatus was neither near nor in contact with the ice sheet during the relaxation tests. These measurements were then utilized to calculate the relevant dynamical properties of the system for this study as elaborated in the following sections.

5.3.1. SIGNAL PROCESSING OF RELAXATION TESTS

The following measurements were extracted from the 6COMP system data of each relaxation test:

- Pull force
- Inertial force
- Displacement from laser transducer
- Acceleration from accelerometer on model structure

and it is of note that all of these measurements correspond to the direction of ice motion for the test runs. The pull force was the force applied to the system in order to achieve the desired displacement from equilibrium. And the inertial force was the force measured by the 6-component load cell sandwich during the oscillations of the decay test. Each of the measurements was filtered with an order 8 Bessel filter (including zero-phase digital filtering) and an offset adjustment was made for each signal by using the mean of the final 10 % duration of the signal. This offset adjustment was chosen because the relaxation test should decay to nil regardless of the offset before the beginning of the relaxation test. In general, the order 8 Bessel filter was found to reduce the energy content from noise for frequencies above 49 Hz by at least 99 %, which is deemed sufficient for this study.

5.3.2. NATURAL FREQUENCY

The dominant natural frequency of the system was determined by first computing the PSD function of the displacement. The maximum energy content at a non-zero frequency was then found within the PSD function, which corresponded to the dominant natural frequency of the system.

5.3.3. DAMPING RATIO

In order to compute the damping ratio from the displacement of the relaxation test, the local maxima—or peaks—from the displacement of the free decay were distinguished. Then, under the assumption of a single-degree-of-freedom system, the logarithmic decrement δ was calculated as follows:

$$\delta = \frac{1}{n} \log \left[\frac{u_s(t_k)}{u_s(t_{k+n})} \right] \tag{5.4}$$

where n is the number of successive peaks, u_s is the structural displacement, t_k is the time instant at peak k, and t_{k+n} is the time instant at successive peak $k+n$. From the logarithmic decrement, the damping ratio ζ_k was found:

$$\zeta_k = \frac{\delta}{\sqrt{4\pi^2 + \delta^2}} \tag{5.5}$$

where the damping ratio corresponds to a specific displacement amplitude at peak k. Based on this method, it was discovered that the damping ratio was dependent on the amplitude of the displacement. Thus, the

number of successive peaks n was specifically selected for each relaxation test and a linear regression was computed for the range of damping ratios depending on the displacement amplitude. The number of successive peaks was chosen based on a trade-off between increasing linear correlation coefficient of the damping ratios to displacement amplitudes and reduction in maximum damping ratio caused by averaging over more successive peaks. Generally, the linear correlation was fairly good, and the computed maximum damping ratio values were reasonable for generic structural damping. For the 26020 and 23010 test runs, the number of successive peaks $n = 2$ was suitable for the respective relaxation tests, and granted positive damping ratios. The presence of negative damping ratios as computed from relaxation tests were the result of beat frequencies within the displacement measurements of the decay test. This was mostly circumvented in the damping ratios for the relaxation tests of the relevant test runs by selecting a sufficiently large number of successive peaks, particularly $n = 2$ in this case. The terms from the linear regression for the displacement-dependent damping ratios for each of the test runs are provided in Table 5.2.

Table 5.2: Linear regression terms and correlation for the displacement-dependent damping ratio for the 26020 and 23010 test runs. For the linear regression $y = ax + b$, y is the damping ratio and x is the displacement amplitude.

Test run	26020	23010
Term "a" [1/mm]	1.268e-02	2.169e-02
Term "b" [-]	2.420e-03	1.356e-03
Linear correlation [-]	0.816	0.888

5.3.4. LINEAR STIFFNESS

During each relaxation test, a pull force was applied to the test apparatus in order to achieve a desired initial displacement of the system and then rapidly removed such that the decay test began and the structure oscillated freely. Before the commencement of the decay test, a gradual increase and then plateau in pull force and displacement were recorded; the measurements from this duration were used to compute the linear stiffness of the system. To compute the linear stiffness, a linear regression was determined for relationship between the pull force and the displacement. As displayed in Table 5.3, because the b linear terms were small compared to the maximum pull force (less than 2 %) and can be neglected, the linear stiffness was taken as the respective a linear term for the 26020 and 23010 test runs. Therefore, assuming a single-degree-of-freedom system, the linear stiffness k_{linear} was defined as follows:

$$k_{linear} = \frac{F_{pull}}{u_x} \tag{5.6}$$

where F_{pull} is the pull force and u_x is the structural displacement. Generally, the linear stiffness of the system matched tolerably with the values provided by HSVA (see Appendix A).

Table 5.3: Linear regression terms and correlation for the linear stiffness for the 26020 and 23010 test runs. For the linear regression $y = ax + b$, y is the pull force and x is the displacement.

Test run	26020	23010
Term "a" [N/mm]	2011	1781
Term "b" [N]	-37	57
Linear correlation [-]	1.000	0.999

5.3.5. SYSTEM MASS

Based on the single-degree-of-freedom system assumption, the mass of the system m_{sys} was determined as follows:

$$m_{sys} = \frac{k_{linear}}{\left(2\pi f_{nat}\right)^2} \tag{5.7}$$

where f_{nat} is the dominant natural frequency of the system. This system mass included the mass of the system springs, compliant basis, 6-component scale, model structure (including added mass from the submerged portion of the structure), and the added weights on the compliant basis to achieve the desired natural frequency.

5.3.6. OSCILLATING MASS

The compliance of the 6-component scale and its location between the model structure and the compliant basis resulted in the inclusion of inertial forces in the 6COMP system ice-induced global forces during the test runs. The presence of inertial loads in the global load measurements meant that the 6COMP global loads were not solely from ice action on the model structure. Thus, it was essential to distinguish and attenuate the inertial loads in the 6COMP global loads. As recommended by HSVA, the inertial loads were assumed to be the product of the acceleration of the model structure and an oscillating mass. The oscillating mass is a simplified representation of the mass of the model structure, the added mass from the water accelerated around the submerged portion of the model structure, and other equipment influencing the inertia of the system that were recorded in the accelerations by the accelerometer. The oscillating mass was determined by means of relaxation tests. Provided that only one dominant natural frequency is observed in the oscillations of the system, the free decay of the relaxation test can be used to find the oscillating mass based on the simplifying assumption of a single-degree-of-freedom system.

First, the local maxima—or peaks—from the displacement measurements of the free decay test were distinguished. Then the acceleration and inertial force measurements at the corresponding displacement peaks were found. To compute the oscillating mass, a linear regression was determined for relationship between the inertial forces and the accelerations at the corresponding displacement peaks. As presented in Table 5.4, the b linear terms were small compared to the maximum inertial force (less than 5 %) and can be neglected; therefore, the oscillating mass was taken as the respective a linear term for the 26020 and 23010 test runs. The oscillating mass m_{osc} was determined based on the following relationship:

$$m_{osc} = \frac{F_{iner}(t_k)}{\ddot{u}_s(t_k)} \tag{5.8}$$

where F_{iner} is the inertial force, t_k is the time instant at displacement peak k, and $\ddot{u}_s$ is the structural acceleration. The displacement peaks were selected instead of the acceleration or inertial force peaks because the acceleration or inertial force measurements contained, at larger displacements, the presence of the natural frequency from the bending of the 6-component scale. This other natural frequency caused the method of determining the oscillating mass to deviate at the larger displacements, but otherwise the method was valid and the results were suitable for this study.

Table 5.4: Linear regression terms and correlation for the oscillating mass for the 26020 and 23010 test runs. For the linear regression $y = ax + b$, y is the inertial force and x is the acceleration.

Test run	26020	23010
Term "a" [kg]	128	139
Term "b" [N]	6	2
Linear correlation [-]	0.979	0.996

5.4. POST-CALIBRATION OF TACTILE ICE-INDUCED GLOBAL LOADS

The data recorded by the TAC system comprised movie frames of pressure sensels that mapped the pressure distribution along the ice-structure interface during the test runs. The pressure sensels measured local, relative pressures and required calibration in order to indicate actual pressures. Many issues with calibration before testing, such as the dependence of the tactile sensor readings on temperature, deterred the use of this method. Instead, post-calibration of the TAC system was chosen, which relied on the data—and therefore the calibration—of the 6COMP system for accurate results. The relative pressures could not be converted into actual pressures, but ice-induced global loads from the tactile sensor pressure measurements could be post-calibrated using the ice-induced global loads from the 6COMP data. The process of post-calibration involved numerous assumptions and steps, which are detailed in the following sections.

5.4.1. PRESSURE DISTRIBUTION

Of interest to the post-calibration of the tactile ice-induced global loads were the data of the large tactile sensor. The large tactile sensor data comprised 44 rows by 54 columns of sensels and recorded the relative pressure distribution about the entire ice-structure interface, and not just a local region, which was necessary to compute the global loads caused by the interaction between the ice and structure. For the large tactile sensor, each pressure sensel was 9.271 mm in width and 4.699 mm in height. Lacking in calibration prior to testing, the pressure sensels of the large tactile sensor recorded relative pressures ranging from 0 to 255. The number 0 indicated no pressure and the number 255 represented saturated pressure, which meant a relative pressure of at least 255; therefore, saturated pressure could not be considered valid for precise numerical analysis.

Because the measured pressures were relative, and depending on the sensitivity setting of the relative pressure for the particular test run, the contribution of noise to the pressure sensor data was generally very significant, especially during periods when minor ice crushing occurred. One manner of mitigating the contribution of noise, preceding the calculation of tactile global ice-induced loads, was to specifically select the most relevant pressure sensels to be used for the calculation. In addition to noise, other erroneous data were collected by the pressure sensels. The sources of error included pressure from bending of the sensor around the structure, water pressure from seepage between the sensor and structure, or even combinations of these with noise. Thus, it was very important to incorporate only relevant pressure sensels in the computation of the tactile global load.

To assist in choosing the pressure sensels of interest, the peak relative pressures over the entire duration of the test run were compiled into a single pressure distribution frame in order to discern the range of rows and columns containing ice crushing pressures. Figure 5.2 and Figure 5.3 portray this technique for the 26020 and 23010 test runs, respectively. Note for clarity that relative pressures of 0 are colored in sensels of black and relative pressures of 255 are colored in sensels of magenta. Additionally, a recommended range of rows and columns that contained pertinent ice crushing pressures is respectively indicated by the red box in Figure 5.2 and Figure 5.3. The criterion for the dimensions of the red box is that the mean of each of the rows and columns considered is at least the mean of the entire frame.

Several issues with the data were observed upon inspection of the frame of peak relative pressures for each test run. In general, the number of saturated pressure sensels in the ice-structure interaction zone was not insubstantial. Moreover, entire rows or columns of the large tactile sensor were not recording during testing, likely caused by a fault in the pressure sensor or in the connection between sensor and measurement system. For some cases, the missing row or column was located in a region where important ice crushing pressure should have been recorded. For the specific case of the missing row 23 in Figure 5.2, in a region where important ice crushing pressure should have been recorded, error is introduced into the computation of the tactile global loads which cannot be remedied in post-processing. Further ramifications of these issues are mentioned in terms of the post-calibration in Section 5.4.

5.4.2. ISOLATION OF PRESSURE SENSELS

The presence and relative magnitude of noise in the tactile sensor is clearly illustrated in Figure 5.2 by the sensels of dark blue that are far from the ice-structure interface, highlighted approximately by the red box. In Figure 5.3, noise—or at least not pressure from ice crushing—was observed approximately between columns 1 and 7. To avoid including this noise in the calculation of the ice-induced global loads, only the pressure sensels within or near the red box for each test run were considered. Note that the red box was not used explicitly in defining the region of relevant pressure sensels, but only was utilized as a reference. The pressure sensels of interest were chosen manually and are given below in Table 5.5. For the rectangular cross-section structure from 26020 test run, the rows and columns of pressure sensels were divided into three regions: starboard, front, and port. The front region was distinguished by containing rows of sensels with the majority of ice crushing pressure. Moreover, the columns of the front region were chosen based on the bending noise caused by the corners of the structure at columns 21 and 43. Although no substantial relative pressures were recorded on the starboard side of the structure for this duration, a region of equal size to the port side was included for the starboard side for the purpose of symmetry. The presence of significant, asymmetric ice crushing pressures on the port side may indicate that the structure was mounted at an oblique angle to the direction of ice motion. This potential issue is detailed in Chapter 7.

An issue with directly removing the noise in the pressure sensor data was the superposition of the noise with the ice crushing pressures in the region of ice-structure interface. Furthermore, the magnitude and

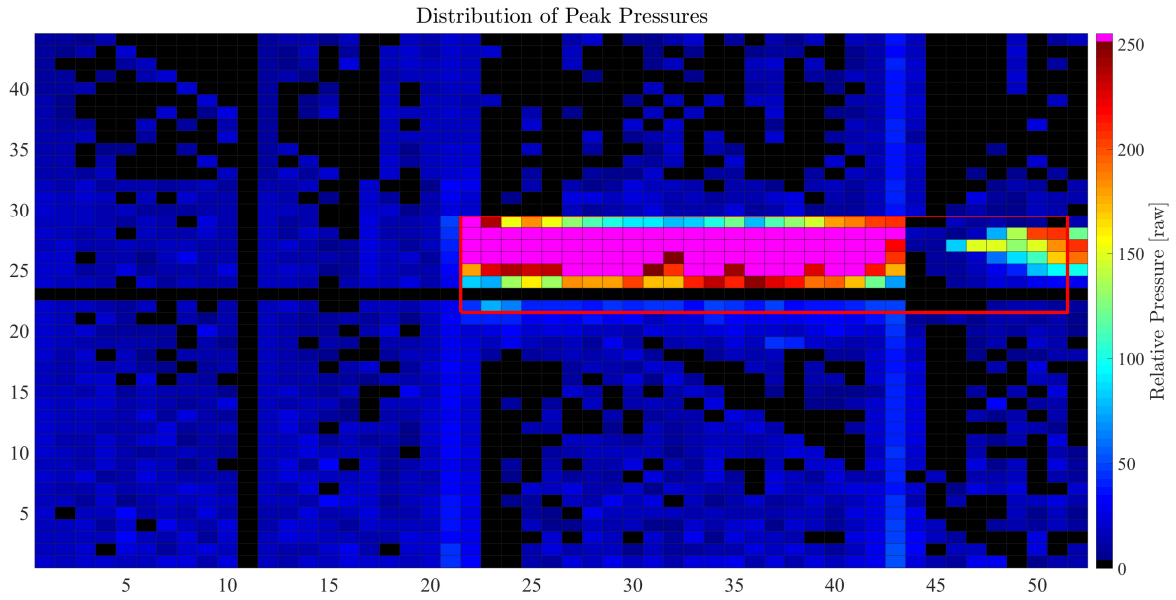

Figure 5.2: Frame containing the distribution of peak pressures over some duration for the 26020 test run. The red box highlights a region of interest.

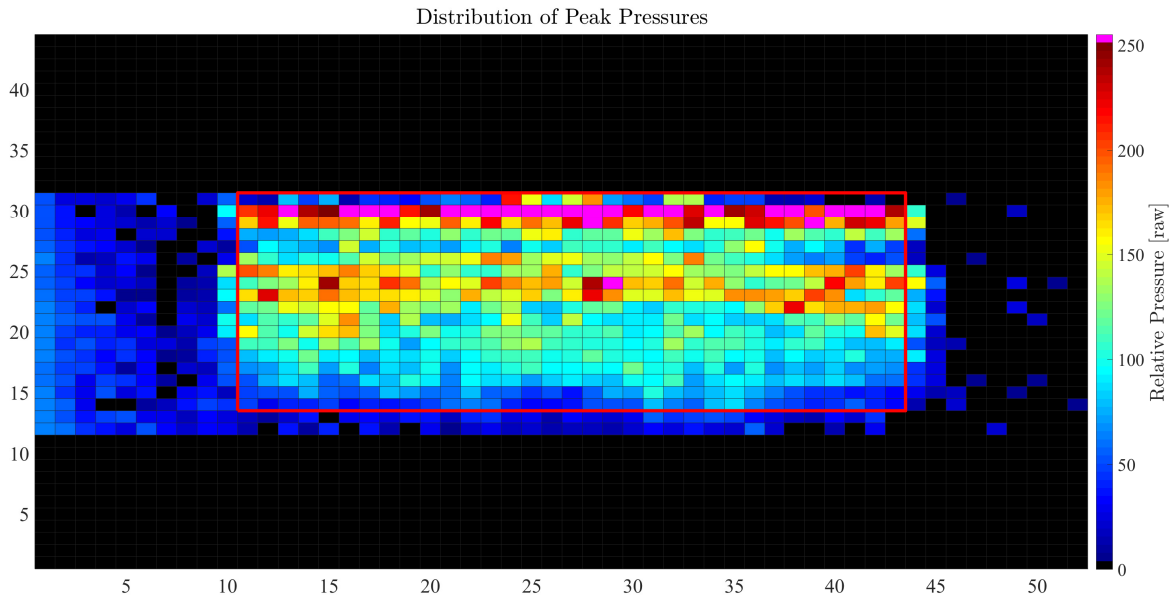

Figure 5.3: Frame containing the distribution of peak pressures over some duration for the 23010 test run. The red box highlights a region of interest.

location of the noise varied temporally and not necessarily periodically; therefore, the explicit removal of only noise would be very difficult and was not attempted in this study.

Table 5.5: Inclusive range of rows and columns for selected pressure sensels from 26020 and 23010 test runs.

Test run	26020	23010
Side of structure	Starboard; Front; Port	Front
Rows	22-29; 22-29; 22-29	13-33
Columns	12-20; 21-43; 44-52	10-44

5.4.3. DEFINITION OF CROSS-SECTIONAL GEOMETRY

The pressure distribution along the perimeter of the model structure represented the pressures orthogonal to the surface. Therefore, the geometry of the cross-section of the model structure required definition with respect to the pressure distribution in order to assign locations to the pressures and later direction to the global forces. Figure 5.4 and Figure 5.5 illustrate schematics of the cross-sectional geometry of the respective model structures and confirm the manual definition of a spatially dependent coefficient designed to decompose the global forces into components parallel and orthogonal to the direction of ice motion. This coefficient is explained in the next section. The exact location of the pressure sensels on the perimeter of each model structure was not known; therefore, it was assumed that the center of the peak pressure distribution of the front region corresponded to the center of the front side of the model structure. Note that only the selected pressure sensels are shown in Figure 5.4 and Figure 5.5 as the other sensels are not considered for the remainder of the study.

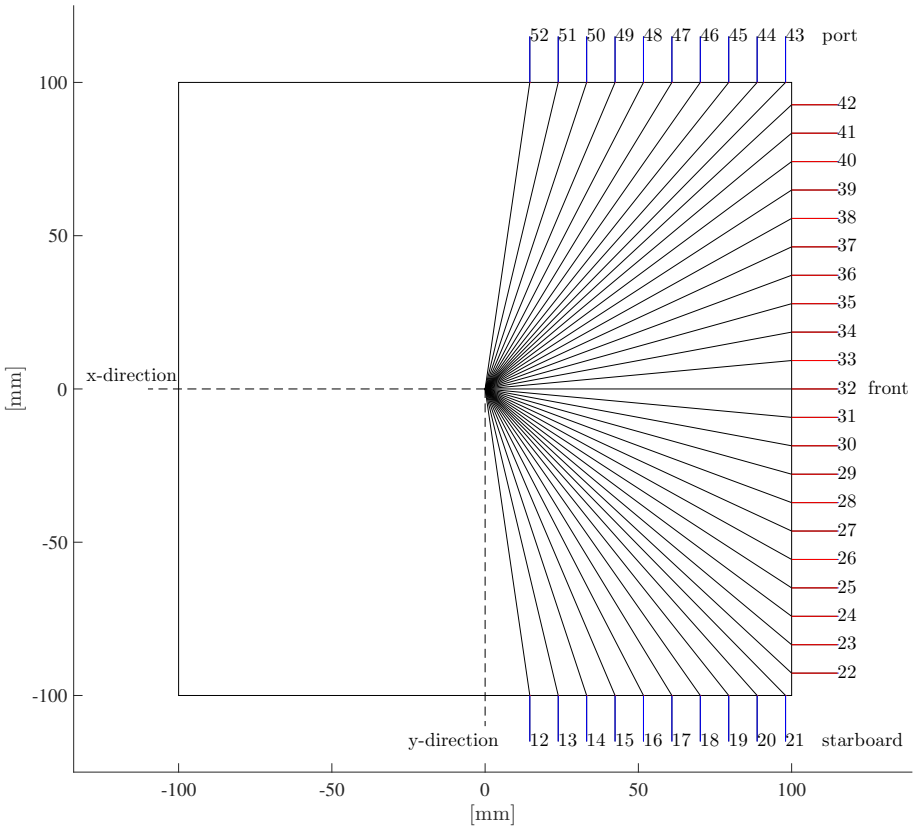

Figure 5.4: Geometric force decomposition schematic and location of pressure sensel columns along perimeter of structure for 26020 test run. Legend: red – force parallel to ice motion (x-direction); blue – force orthogonal to ice motion (y-direction).

5.4.4. CALCULATION OF TACTILE GLOBAL FORCE

From the selected pressure sensels, the tactile ice-induced global force was computed by means of the following equations. The uncalibrated tactile global force F_N^{TAC*} normal to the surface of the structure was calculated as follows:

$$F_N^{TAC*}(t) = \sum_{j=1}^{J} \sum_{i=1}^{I} P_{ij}(t) A_{ij} \tag{5.9}$$

where t is time, J is the total number of selected pressure sensel columns for each column j, I is the total number of selected pressure sensel rows for each row i, P_{ij} is the relative pressure of each pressure sensel, and A_{ij} is the area of each pressure sensel. Note that this force is computed from actual area values (units of mm^2) but from relative pressure values, meaning that the signal is an artificial force (denoted units of raw)

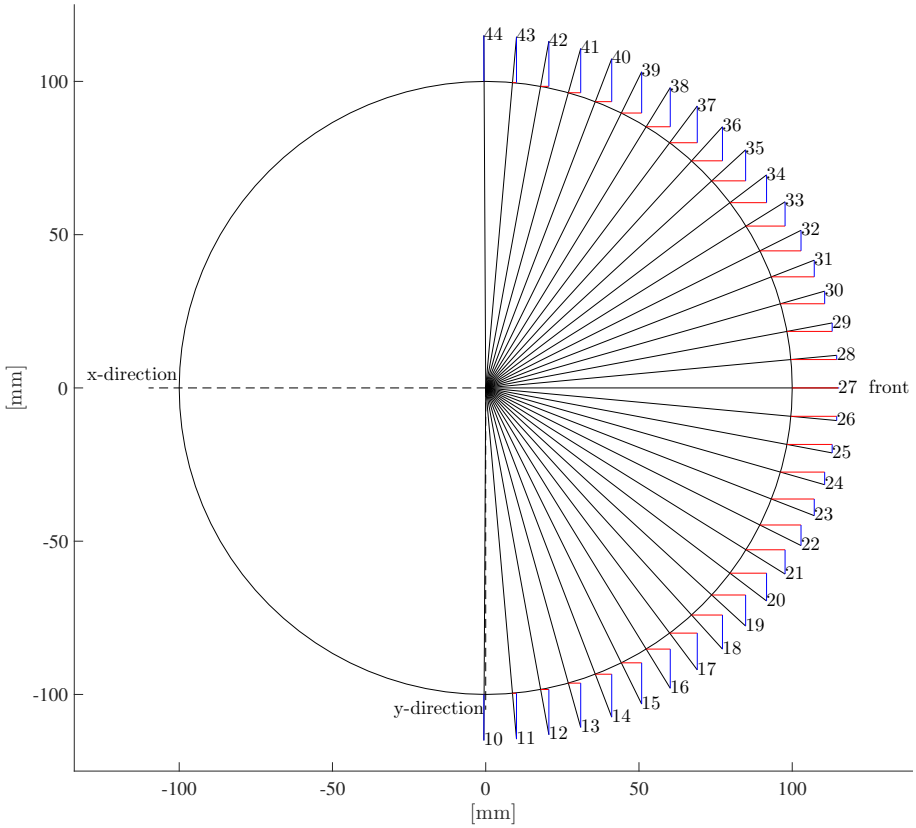

Figure 5.5: Geometric force decomposition schematic and location of pressure sensel columns along perimeter of structure for 23010 test run. Legend: red – force parallel to ice motion (x-direction); blue – force orthogonal to ice motion (y-direction).

until post-calibrated. Because the 6COMP ice-induced global forces of interest were measured parallel and orthogonal to the direction of ice motion, comparable tactile global forces were needed in those directions for proper post-calibration. The uncalibrated tactile global force F_x^{TAC*} parallel to the direction of ice motion (x-direction) was determined as follows:

$$F_x^{TAC*}(t) = \sum_{j=1}^{J} \sum_{i=1}^{I} P_{ij}(t) A_{ij} \cos\theta_j \tag{5.10}$$

where θ_j is the angle from the centerline of the model structure—parallel to the direction of ice motion—to the location of the pressure sensel. This angle was defined manually by the shape of the cross-section of the model structure and the approximate location of the pressure sensels along the perimeter of the cross-section. The application of angle θ_j is represented by the black radii in Figure 5.4 and Figure 5.5. Similarly, the uncalibrated tactile global force F_y^{TAC*} orthogonal to the direction of ice motion was computed as follows:

$$F_y^{TAC*}(t) = \sum_{j=1}^{J} \sum_{i=1}^{I} P_{ij}(t) A_{ij} \sin\theta_j \tag{5.11}$$

where the direction normal to the ice motion is represented by the y-direction. The aforementioned coefficient of geometric force decomposition was defined as the $\cos\theta_j$ for the x-direction and $\sin\theta_j$ for the y-direction; however, the angle θ_j for the rectangular cross-section structure of the 26020 test run was set as $\theta_j = -\pi$ for the starboard side, $\theta_j = 0$ for the front side, and $\theta_j = \pi$ for the port side.

In summary, the following derived TAC measurements were considered for the rest of the post-calibration method:

- Force in x-direction (uncalibrated)
- Force in y-direction (uncalibrated)

while noting the sampling frequency of about 300 Hz and the corresponding time series of the TAC data.

5.4.5. SIGNAL PROCESSING

For the post-calibration of the tactile ice-induced global loads, the following measurements were extracted from the 6COMP system data for each test run:

- Force in x-direction from 6-component scale
- Force in y-direction from 6-component scale
- Acceleration in x-direction from accelerometer on model structure
- Acceleration in y-direction from accelerometer on model structure
- Velocity of ice in x-direction

where the ice velocity was technically the velocity at which the carriage—and therefore the compliant basis and model structure—moved through the ice basin, but relatively represented the velocity of the ice impinging on the model structure during the test runs. Each of these measurements, including derived TAC global force measurements from Section 5.4.4, was filtered with an order 8 Bessel filter (including zero-phase digital filtering) and an offset adjustment was made for each signal by using the mean of the first 5 s duration of the signal. In general, the order 8 Bessel filter was found to reduce the energy content from noise for frequencies above 49 Hz by at least 99 %, which was deemed sufficient for this study.

5.4.6. ATTENUATION OF INERTIAL LOADS

As previously discussed in Section 5.3.6, the load cells of the 6-component scale measured both ice-induced and inertial global loads during the test runs. To attenuate these undesirable loads, the inertial force F_{x-iner}^{6COMP} from the x-direction 6COMP load measurements was computed as follows:

$$F_{x-iner}^{6COMP}(t) = m_{osc}\ddot{u}_x(t) \tag{5.12}$$

where m_{osc} is the oscillating mass as determined in Section 5.3.6 and $\ddot{u}_x$ is the x-direction structural acceleration. Assuming symmetry of properties of the test apparatus between the x-direction and y-direction, the the inertial force F_{y-iner}^{6COMP} from the y-direction 6COMP load measurements can be calculated similarly:

$$F_{y-iner}^{6COMP}(t) = m_{osc}\ddot{u}_y(t) \tag{5.13}$$

where $\ddot{u}_y$ is the y-direction structural acceleration. It is important to note that the relaxation test for each test run was only performed in the x-direction, the direction of ice motion. Therefore, the oscillating mass in the y-direction could not be determined in the same explicit manner as that for the x-direction. For attenuation, the inertial forces in the x-direction and y-direction were directly subtracted from their respective 6COMP global force signals for the 26020 and 23010 test runs. To visually assess the impact of the inertial load attenuation, Figure 5.6 and Figure 5.7 illustrate a prominent reduction in energy content at the dominant natural frequency for the 26020 and 23010 test runs, respectively. This method of inertial load attenuation in the x-direction targets and reduces the energy content near the dominant natural frequency of the structure, but may also introduce some energy content to the natural frequency of the bending of the 6-component scale by means of the acceleration signal. This method is also applied to the y-direction, but because the oscillating mass in the y-direction is not explicitly known, the result in this case is treated warily. Overall, the method is deemed suitable as a preliminary means of inertial load mitigation for this study; however, further review is highly recommended.

5.4.7. TIME-SYNCHRONIZATION OF FORCES

The data acquisition devices of the 6COMP and TAC systems collected data separately; in order to compare the global loads between the systems, the data needed to be synchronized in time. Due to the difference in storage space between the the data acquisition devices of the 6COMP and TAC systems, the 6COMP system typically recorded data sets for longer duration than that of the TAC system. To facilitate the synchronization of the global forces in time between the 6COMP and TAC systems, the data of the 6COMP system was

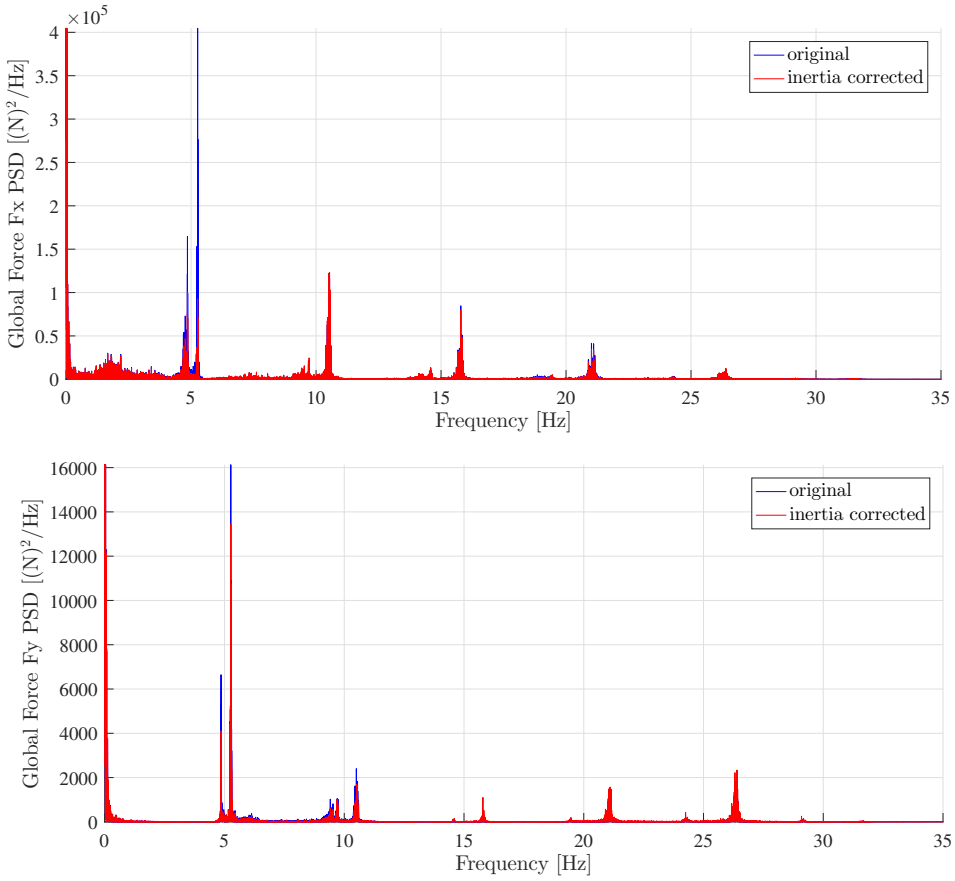

Figure 5.6: Effect of inertial load attenuation on power spectral density function of the x- and y-direction global loads for the 26020 test run. The ordinate is truncated for clarity.

truncated such that the global force signals more closely matched in shape between the systems. Generally, time–synchronization can be readily executed for time series with equal sampling frequencies. Unfortunately, the sampling frequencies differed between the 6COMP and TAC systems. To match sampling frequencies and synchronize the systems in time, the following routine was performed. First, the 6COMP time series with a sampling frequency of 600 Hz was decimated via reverse interpolation by a MATLAB default function to about 300 Hz, which approximately matched the TAC system sampling frequency. Second, cross-correlation of the signals was conducted with a MATLAB default function to compute the lag required to shift the TAC global load in time and match the TAC global load signal shape with the 6COMP global load signal shape. For consistency, the TAC global load was always shifted with respect to the 6COMP global load. Third, the lag was applied to the TAC global load time series such that the original 600 Hz 6COMP global load and 300 Hz TAC global load were synchronized in time.

The synchronization of global loads in time between the 6COMP and TAC systems was performed for the x-direction and then the x-direction lag was applied to the y-direction time series to shift and synchronize the y-direction global loads. In this manner, the x-direction and y-direction global loads were shifted equivalently. The time-synchronization of the x-direction and y-direction global loads for the 26020 and 23010 test runs was cursorily verified by visual inspection (see Figure 5.8 and Figure 5.9, respectively).

5.4.8. TRUNCATION BY SELECTION OF CONSTANT ICE VELOCITY

Each model structure was tested over a range of ice velocities (see Appendix A) that was recorded in time as a continuous data set for each test run. The different regimes of ice-induced vibrations experienced by each model structure during each test run were dependent on ice velocity and varied in magnitude of force as well as dynamic structural response. For the post-calibration of the TAC global loads for some duration

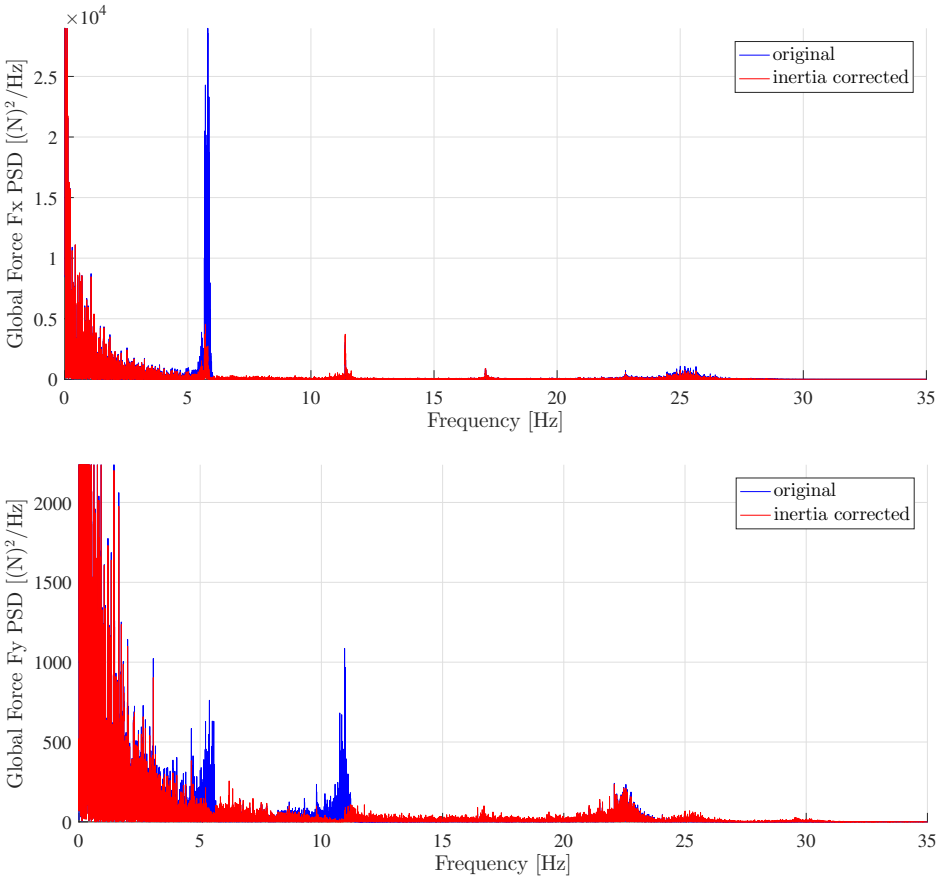

Figure 5.7: Effect of inertial load attenuation on power spectral density function of the x- and y-direction global loads for the 23010 test run. The ordinate is truncated for clarity.

to be valid, the regime of ice-induced vibrations should be maintained. Therefore, a duration with constant ice velocity was chosen for each test run; in this case, a duration with ice velocity of 19 mm/s was selected for the 26020 and 23010 test runs, respectively. The global forces corresponding to this duration of constant ice velocity were again synchronized in time using the same method as in Section 5.4.7. This repetition of synchronization was performed because although the sampling frequency of the 6COMP system was exactly 600 Hz, the sampling frequency of the TAC system was approximately 300.03 Hz. This non-integer ratio between the sampling frequencies of the systems resulted in a phase shift of TAC system over a long duration.

Distinguishing time series of constant ice velocity by manual inspection was challenging because the ice velocity signal from the 6COMP data, which was technically the carriage velocity, was generally severely obfuscated by noise. Moreover, the noise in the ice velocity signal primarily originated from the velocity controller of the carriage that used stepwise error correction with magnitude on the order of the ice velocity increments, which made differentiating between noise and changes in ice velocity difficult.

5.4.9. METHODOLOGY FOR POST-CALIBRATION

To post-calibrate the x-direction TAC global loads using the x-direction 6COMP global loads, specific data points from the TAC global loads were selected. Based on the recommendations by HSVA and the measurement quality from the large tactile sensor, the following criteria were developed to specify useful data points from the TAC global loads for post-calibration:

1. The global load data point must be equal to at least half of the mean of global load (no local minima).

2. No saturated pressure sensels can be present in the frame corresponding to the global load data point; all pressure sensels must contain less than 255 relative pressure.

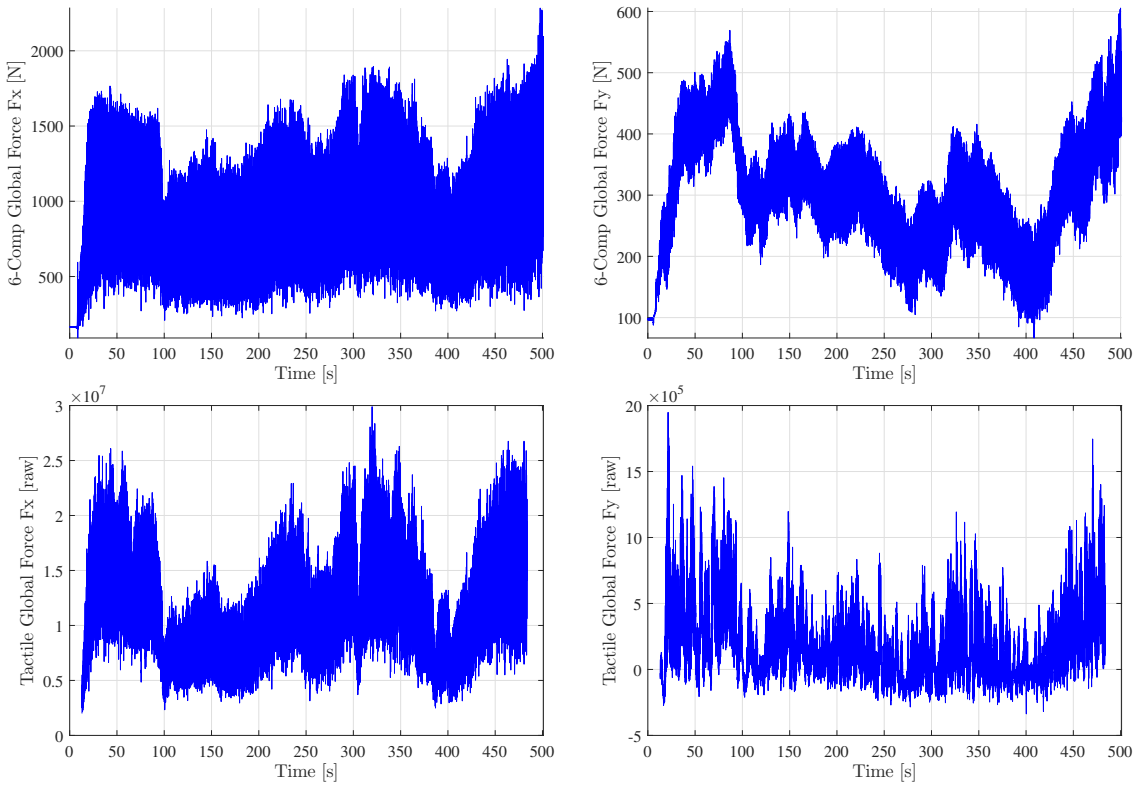

Figure 5.8: Synchronization in time of the x- and y-direction global loads from the 6COMP and TAC systems for the 26020 test run.

3. For each frame corresponding to the global load data point, there should be a user specified minimum number of sensels of at least 95 to 98 % of maximum pressure for that frame (recommend 4 to 6 sensels).

TAC global load data points of interest comprised frames with many pressure sensels of high relative pressure that were less than the saturation pressure. The criterion 2 and 3 ensured that actual relative pressures were considered, and not saturated sensels which may have contained more pressure than recorded. Also, a minimum global load was set via criterion 1 to avoid inclusion of frames with relatively high levels of noise and other anomalies. Application of these criteria were executed on the TAC global loads to determine a frequency of occurrence of frames containing a specific number of sensels which satisfy the criteria. It was assumed that frequency of occurrence of the frames should be no more than 100 in order to limit the number of data points selected; this was fairly arbitrary but expedited manual inspection of data points selected.

The TAC global load data which satisfied the criteria were selected and the concurrent 6COMP global load data points were determined. Using these data points, a power regression was fit to the data which acted as the means to post-calibrate the TAC global loads. The power regression, as defined by Tekscan (2003) and practiced by Ziemer (2015), was defined as follows:

$$F_x^{6COMP} = a\left[F_x^{TAC*}\right]^b \tag{5.14}$$

where F_x^{6COMP} is the x-direction 6COMP global load data points, F_x^{TAC*} is the x-direction uncalibrated TAC global load data points, and a and b are the terms derived from the power regression for the post-calibration of the x-direction TAC global loads. The x-direction calibrated TAC global force F_x^{TAC} was calculated as follows:

$$F_x^{TAC}(t) = a\left[F_x^{TAC*}(t)\right]^b \tag{5.15}$$

where $F_x^{TAC*}(t)$ is the x-direction uncalibrated TAC global load for each time t of the duration of constant ice velocity. Table 5.6 presents the terms derived from the power regression of the data points from the x-direction 6COMP and uncalibrated TAC global loads for the 26020 and 23010 test runs.

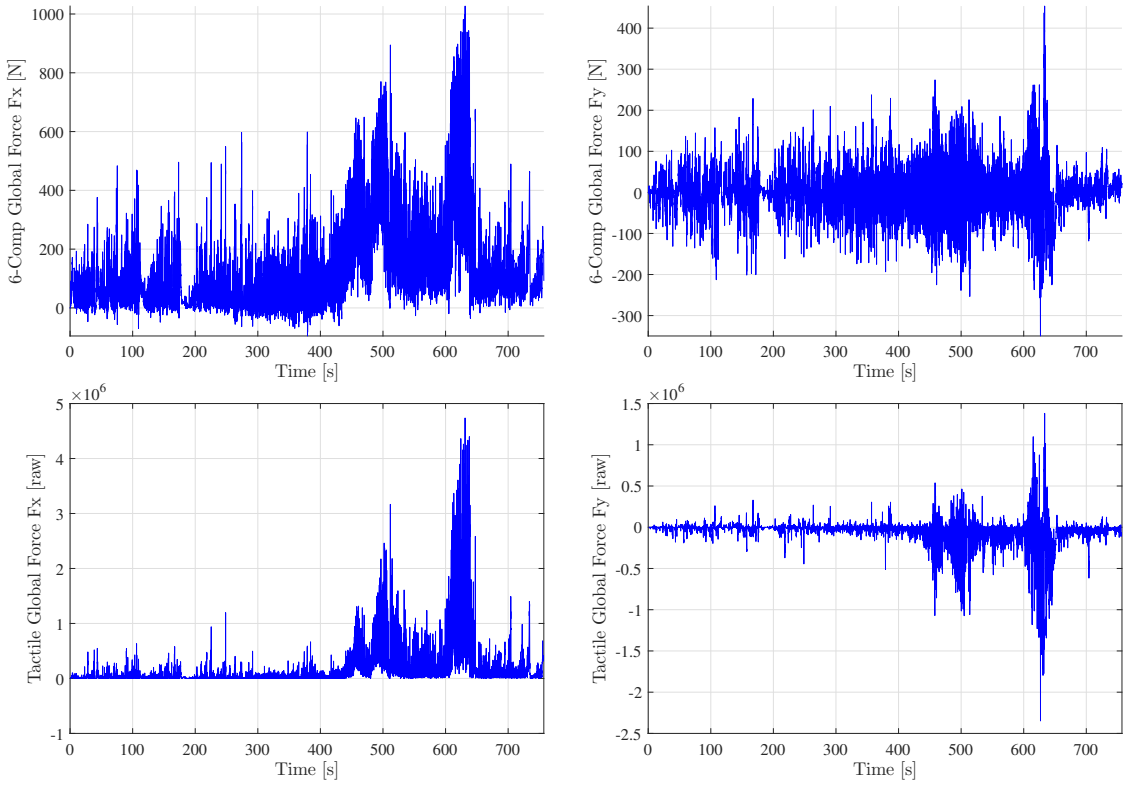

Figure 5.9: Synchronization in time of the x- and y-direction global loads from the 6COMP and TAC systems for the 23010 test run.

Table 5.6: Power regression terms and linear correlation of the data points for the post-calibration of the x-direction TAC global loads for the 26020 and 23010 test runs. For the power regression $y = ax^b$, y is the 6COMP global force and x is the uncalibrated TAC global force.

Test run	26020	23010
Term "a" [N]	8.438e-04	1.056e+00
Term "b" [-]	8.547e-01	4.380e-01
Linear correlation [-]	0.876	0.919

Since the y-direction global loads could be in both positive and negative directions, the method of post-calibration with a power regression was not applicable to the y-direction. Due to insufficient time, another post-calibration technique was not developed. Instead, the power regression terms from the x-direction post-calibration were directly implemented to determine y-direction calibrated TAC global force F_y^{TAC} as follows:

$$F_y^{TAC}(t) = a\left[F_y^{TAC*}(t)\right]^b \tag{5.16}$$

where $F_y^{TAC*}(t)$ is the y-direction uncalibrated TAC global load for each time t of the duration of constant ice velocity and a and b are the terms derived from the power regression for the post-calibration of the x-direction TAC global loads. The results of this approach were unsatisfactory and inconclusive, but the method was nevertheless applied for the sake of curiosity. The results of the post-calibration of the x-direction and y-direction TAC global loads for a duration with constant ice velocity of 19 mm/s are shown in Figure 5.10 and Figure 5.11 for the 26020 and 23010 test runs, respectively.

VALIDATION BY ALTERNATIVE METHODOLOGY

Of concern regarding the post-calibration technique was the difference in range of global loads between the TAC and 6COMP systems; the ratio between the maximum global loads and the ratio between the minimum global loads for each system were not similar. To investigate this issue, an alternative calibration technique was developed and implemented as follows:

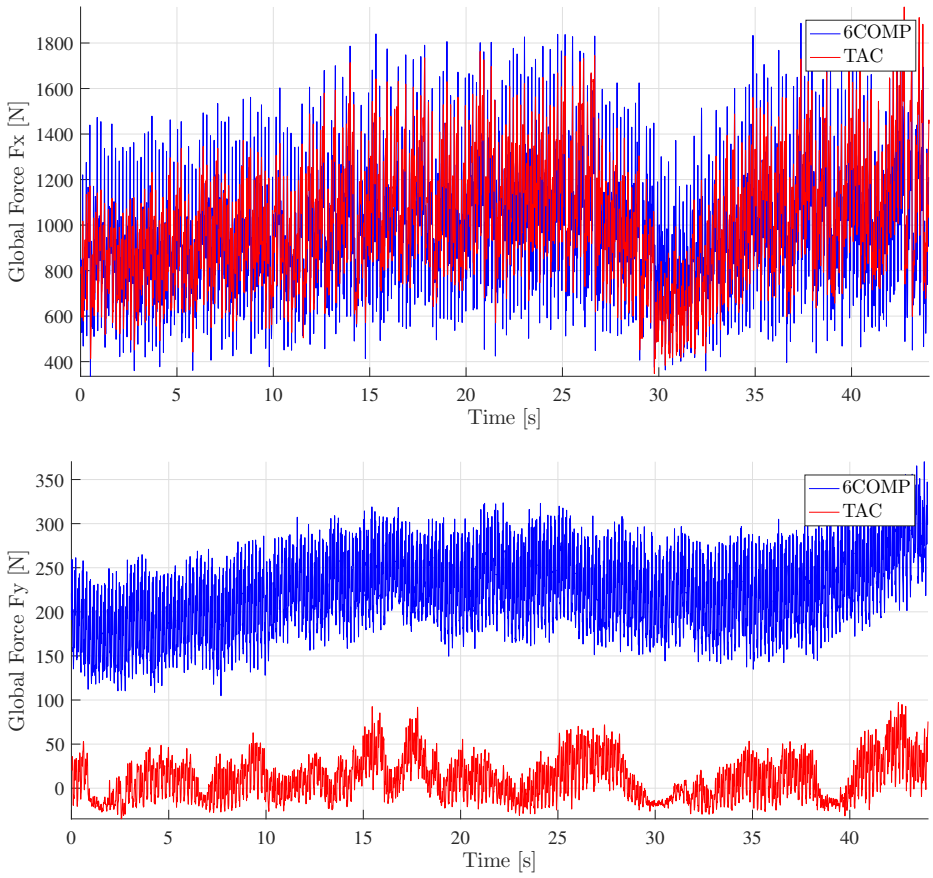

Figure 5.10: Comparison of the x- and y-direction global loads from the 6COMP and calibrated TAC systems for the 26020 test run. The duration corresponds to a constant ice velocity of 19 mm/s.

1. Respective mean values are subtracted from the calibrated and uncalibrated signals.
2. Absolute values of the both signals are taken while noting the indices of negative and positive values.
3. A power regression is fit using all data points from both signals subjected to steps 1 and 2 and the regression coefficients are recorded for the calibration function.
4. The calibration function is applied to the uncalibrated signal subjected to steps 1 and 2 and then the positive and negative values are restored.
5. Mean value of the original calibrated signal is added to the newly calibrated signal from step 4 under the assumption that the calibrated mean values should be equivalent.

This calibration method was tested on two simulated sinusoidal signals with different mean values and amplitudes but with the same phase. It was found that the technique matched the simulated signals more or less exactly, which proved the validity of this calibration method. When this calibration technique was applied to the temporally local x-direction TAC and 6COMP global loads, the resulting x-direction calibrated TAC global loads were similar to those from the original calibration method. Therefore, the original calibration method was decided as appropriate for further analysis since the alternative calibration method demonstrated no significant improvement to the post-calibration of the TAC global loads. An interesting general finding was the difference in shape of signals at a local level. Even though the 6COMP and TAC global loads were synchronized in time both globally and locally, the shape of signals did not match sufficiently for the power regression to have a valid fit. The selection of specific data points was necessary in this case for adequate fitting of the data by power regression.

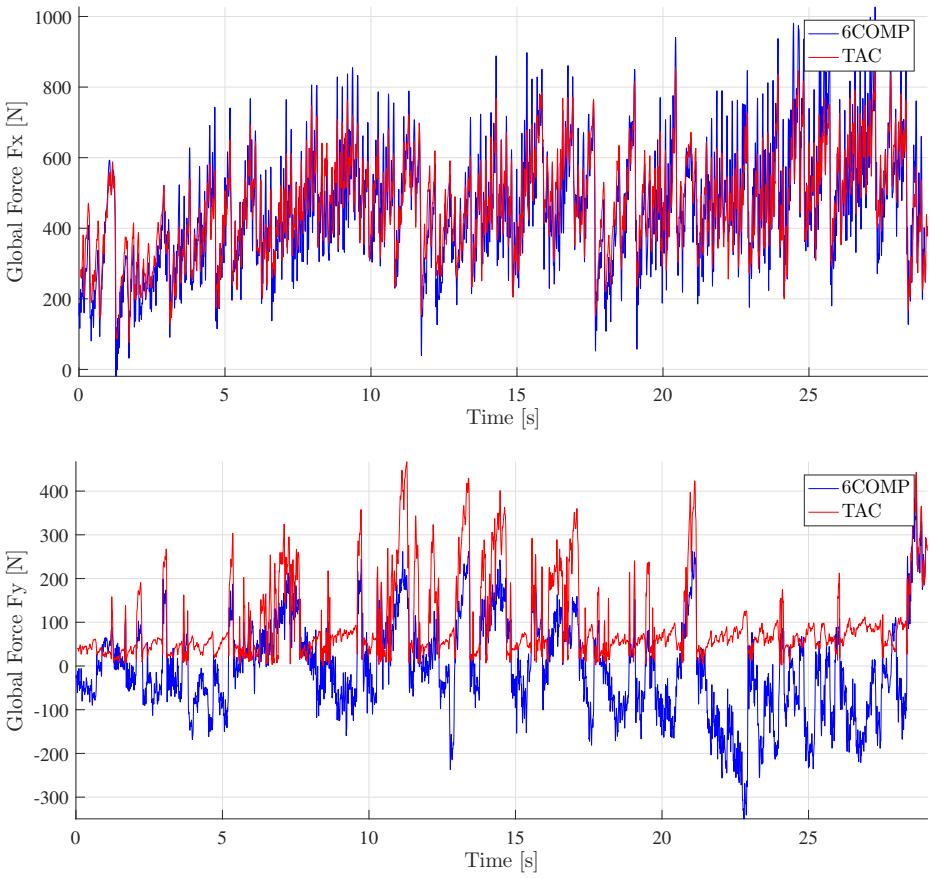

Figure 5.11: Comparison of the x- and y-direction global loads from the 6COMP and calibrated TAC systems for the 23010 test run. The duration corresponds to a constant ice velocity of 19 mm/s.

5.4.10. CONCLUSION FOR POST-CALIBRATION

The post-calibration method was devised based on the available data and the guidance from HSVA. Based on the results from the post-calibration of the TAC global loads, it was decided that the post-calibration method was not suitable to match the 6COMP and TAC global loads. A major problem was that the TAC system data were recorded at different sensitivities for different test runs. The difference in sensitivity altered the relative pressure saturation of the pressure sensels and influenced the inclusion of noise. The saturation of the relative pressure caused a false limit to the recorded pressures, meaning that higher pressures could have existed but could not be recorded. Also, the noise—at the same order of magnitude—severely obfuscated the pressure measurements at times of low ice crushing pressures. Henceforth, the 6COMP data were exclusively post-processed (see Section 5.5) and used for following analyses (see Chapter 6 and Chapter 7), given the uncertainty in the post-calibration technique and the lack of clarity in the data of the TAC system.

5.5. POST-PROCESSING FOR GLOBAL COMPARATIVE ANALYSIS

As previously stated, the data from the 6COMP system were exclusively chosen for further analysis in this study. Preceding the analysis, these data were post-processed using techniques that are treated in the next sections.

5.5.1. SIGNAL PROCESSING

The following relevant data were extracted from the 6COMP system:

- Force in x-direction from 6-component scale

- Force in y-direction from 6-component scale
- Acceleration in x-direction from accelerometer on model structure
- Acceleration in y-direction from accelerometer on model structure
- Displacement in x-direction from laser transducer
- Velocity of ice in x-direction

from the 26020 and 23010 test runs. Each of these measurements was filtered with an order 8 Bessel filter (including zero-phase digital filtering) and an offset adjustment was made for each signal by using the mean of the first 5 s duration of the signal. In general, the order 8 Bessel filter was found to reduce the energy content from noise for frequencies above 49 Hz by at least 99 %, which was deemed sufficient for this study.

5.5.2. DERIVATION OF DISPLACEMENT FROM ACCELERATION

Besides the x-direction structural displacement, the y-direction displacement was also of interest to this study. The Qualisys optical motion capture system provided displacement measurements of the compliant basis, but only for the 23010 test run and not for the 26020 test run. Moreover, the motions of the compliant basis were not suitable to represent the motions of the model structure due to the flexibility of the 6-component scale. Therefore, the measurements from the Qualisys optical motion capture system were not considered for this study. Alternatively, the displacements of the model structure were determined from the acceleration signals. First, the derived velocity of the model structure $\dot{u}_s$ for the respective x-direction and y-direction was computed as follows:

$$\dot{u}_s(t) \approx \frac{1}{2}\sum_{t}^{t+t_s}\left[\ddot{u}_s(t+t_s)+\ddot{u}_s(t)\right]\left[(t+t_s)-t\right] \tag{5.17}$$

where t is some time instant, t_s is the incremental time step, and $\ddot{u}_s$ is the structural acceleration. Because the trapezoidal numerical method of integration can only approximate between existing data points, the integrated data set was one element shorter than the original data set. Specifically, the integrated data set was shifted by one element such that the computed area beneath each pair of elements in the original data set was assigned to the first element of each pair. This method approximately maintained the time series when comparing the various data sets. Second, the derived velocity $\dot{u}_s$ was then filtered with an order 8 Bessel filter (including zero-phase digital filtering) to mitigate any remaining noise that was exacerbated by the approximate numerical integration. The order 8 Bessel filter was found to reduce the energy content from noise for frequencies above 49 Hz by at least 98 %, which was deemed sufficient for this study. Third, the derived displacement of the model structure u_s for the respective x-direction and y-direction was computed as follows:

$$u_s(t) \approx \frac{1}{2}\sum_{t}^{t+t_s}\left[\dot{u}_s(t+t_s)+\dot{u}_s(t)\right]\left[(t+t_s)-t\right] \tag{5.18}$$

where the resulting data set was two elements shorter than the original data set due to the double numerical integration. An issue with this method of determining displacements was that a potential non-zero mean in the derived velocity or displacement signals, if actually present in the test runs, could not be found. Furthermore, the displacement from the laser transducer and the derived displacement in the x-direction were compared from both 26020 and 23010 test runs and the derived displacement was observed with significantly greater mean amplitude than that of the laser transducer. Under the assumption that the x-direction displacement from the laser transducer was an acceptable basis for displacements of the model structure, a scaling method was developed in attempt to rectify the derived displacements. The displacement scaling factor was defined as the ratio between the mean of the amplitude of the x-direction displacement from the laser transducer and the mean of the amplitude of the derived x-direction displacement. Note that the time-variant mean was subtracted from the x-direction displacement from the laser in order to aptly compare displacement amplitudes. The displacement scaling factor was applied to the x-direction and the scaling method was assessed by computing the linear correlation coefficient between the x-direction amplitudes of derived displacement and displacement from the laser: 0.952 for the 26020 test run and 0.966 for the 23010 test run. Having deemed this method acceptable, the displacement scaling factor was then applied to the y-direction

derived displacement for each of the test runs. Although the mean amplitude of the y-direction derived displacement was scaled, any time-variant mean that may have been present in the y-direction displacement during the test runs could not be readily determined and was thus unknown for this study.

5.5.3. DERIVATION OF VELOCITY FROM DISPLACEMENT

The velocity of the model structure was not measured during the test runs; therefore, it was decided that the velocity would be derived from the displacement measurements. It is important to note that the displacements considered henceforth were the x-direction displacement from the laser transducer and the y-direction derived displacement that was scaled according to Section 5.5.2. The velocity of the model structure $\dot{u}_s$ in the x-direction and y-direction for each test run was determined as follows:

$$\dot{u}_s(t) \approx \frac{u_s(t+t_s) - u_s(t)}{(t+t_s) - t} \tag{5.19}$$

where t is some time instant, t_s is the incremental time step, and u_s is the structural displacement. Because the finite difference method of differentiation can only approximate between existing data points, the derived data set was one element shorter than the original data set. Specifically, the derived data set was shifted by one element such that the computed slope between each pair of elements in the original data set was assigned to the second element of each pair. This method approximately maintained the time series when comparing the various data sets.

5.5.4. FURTHER SIGNAL PROCESSING

The global loads in the x-direction and y-direction for both test runs were attenuated with respect to inertial loads in the same manner as discussed in Section 5.4.6 by using the respective oscillating mass as detailed in Section 5.3.6. A duration with constant ice velocity was then selected and the following post-processed data were truncated:

- Force in x-direction with filtering, offset adjustment, and inertial load attenuation
- Force in y-direction with filtering, offset adjustment, and inertial load attenuation
- Acceleration in x-direction with filtering and offset adjustment
- Acceleration in y-direction with filtering and offset adjustment
- Velocity in x-direction from derivation
- Velocity in y-direction from derivation
- Displacement in x-direction from laser transducer with filtering and offset adjustment
- Displacement in y-direction from derivation with scaling

for the 26020 and 23010 test runs. A constant ice velocity of 19 mm/s was selected for the global comparative analysis because testing was performed at and the frequency lock-in regime of ice-induced vibrations was observed for this velocity for both the 26020 and 23010 test runs. The frequency lock-in regime was visually distinguished by the sustained quasi-harmonic structural displacement, periodic duration with near-zero relative velocity, and the distinct periodic load amplification that was similarly observed in the forced vibration experiments from Hendrikse et al. (2012).

5.5.5. RELATIVE VELOCITY

The relative velocity between the ice and the model structure v_{rel} was determined from the following relationship:

$$v_{rel}(t) = v_{ice} - \dot{u}_x(t) \tag{5.20}$$

where v_{ice} is the constant ice velocity and $\dot{u}_x$ is the x-direction structural velocity.

5.5.6. POST-PROCESSED DATA FOR ANALYSIS

In summary, the following post-processed data were considered for the global comparative analysis:

- Force with filtering, offset adjustment, inertial load attenuation, and truncation
  - in x-direction
  - in y-direction
- Acceleration with filtering, offset adjustment, and truncation
  - in x-direction
  - in y-direction
- Velocity from derivation with truncation
  - in x-direction
  - in y-direction
- Displacement in x-direction with filtering, offset adjustment, and truncation
- Displacement in y-direction from derivation with scaling and truncation
- Relative velocity

where the relative velocity is computed from the velocity in x-direction from derivation with truncation. The time series of the post-processed data are presented in Appendix B. Additionally, a summary of structural and ice properties from the 26020 and 23010 test runs are provided in Table 5.7.

Table 5.7: Summary of ice and structural properties from the 26020 and 23010 test runs. Unmarked properties were provided by Hinse et al. (2017), Ziemer (2016). * Properties computed from relaxations tests. † Damping ratio corresponding to a structural displacement amplitude of 1.0 mm. ‡ Single ice velocity chosen for comparison; other velocities are also available.

Property	**Test run**	26020	23010
Structural	**Cross-sectional geometry**	Rectangular	Circular
	Width [mm]	200	200
	System mass* [kg]	1747	1372
	Oscillating mass* [kg]	151	145
	Natural frequency* [Hz]	5.35	5.78
	System stiffness* [N/mm]	2011	1781
	Damping ratio*† [-]	0.0151	0.0230
Ice	**Scale type**	Model	Model
	Thickness [mm]	45	42
	Compressive strength [kPa]	110	97
	Flexural strength [kPa]	60	45
	Velocity‡ [mm/s]	19	19

6

GLOBAL COMPARATIVE ANALYSIS

The following juxtapositional analyses in this chapter focus on particular data from the Phase 2 tests with specific regards to the frequency lock-in regime for the model structures with circular and with rectangular cross-section. To reiterate, only the post-processed data from the 6COMP system as specified by Section 5.5.6 were used for the following analyses due to the uncertainty in the data of the TAC system and the inconclusive results of the post-calibration method (see Section 5.4). In this chapter, the ice-structure interaction is assumed one-dimensional, i.e. only the kinematics and kinetics in the direction of ice motion (x-direction) are considered. However, it is important to note that the ice-structure interaction regarding the circular cross-section structure is indeed a two-dimensional problem; this problem is treated for both structures in Chapter 7.

To begin the global comparative analysis, the differences between test properties of the test runs are addressed in Section 6.1. Then, in Section 6.2, the ice-induced global loads are investigated. Next, the energy of the system is evaluated in Section 6.3. Finally, in Section 6.4, the influence of buckling failure of ice on the aforementioned topics is treated.

6.1. SCALING OF TEST PROPERTIES

In order to precisely compare the effect of cross-sectional geometry of the different structures on the global loads and energy of the system, all other parameters such as the ice and structural properties should be identical. The necessary ice and structural properties of the test runs were recorded such that comparison could be made among the properties from the various test runs. For this study, the circular cross-section (23010) and the rectangular cross-section (26020) model structures were compared based on their cross-sectional shape and similar, but not identical, ice and structural properties. Basic scaling, where deemed appropriate, was applied to the test properties such that more direct comparison of the data from the 26020 and 23010 test runs could be performed and is described in the following sections.

6.1.1. ICE PROPERTIES

To redress the effect of the differences in ice properties between the two relevant test runs on the ice-induced global loads, the global loads from the 23010 test run were scaled using the ice properties from the 26020 test run. This scaling was performed by first identifying the relationship between the global loads and the ice properties. In a very simplified manner, the ice-induced global force F_{ice} on a rigid structure can be described as follows:

$$F_{ice} = \sigma_{comp} h_{ice} w_s \tag{6.1}$$

where σ_{comp} is the compressive strength of the ice, h_{ice} is the ice thickness, and w_s is the width of the ice-structure interface. Asserting that the ice-induced global force is linearly dependent on the ice compressive strength and ice thickness, the ice scaling factor λ_{ice} for the 23010 test run based on the 26020 test run was derived:

$$\begin{aligned}\lambda_{ice} &= \frac{F_{ice}^{Rect}}{F_{ice}^{Circ}} \\ &= \frac{\sigma_{comp}^{Rect} h_{ice}^{Rect} w_s^{Rect}}{\sigma_{comp}^{Circ} h_{ice}^{Circ} w_s^{Circ}} \\ &= \frac{\sigma_{comp}^{Rect} h_{ice}^{Rect}}{\sigma_{comp}^{Circ} h_{ice}^{Circ}}\end{aligned} \tag{6.2}$$

where the superscript $Rect$ refers to the 26020 test run and the superscript $Circ$ refers to the 23010 test run. The ice thickness recorded for each of the test runs was an average value that approximated a homogeneous ice sheet. The width of ice-structure interface was assigned as the width of the structure, meaning that the structural widths were equivalent and therefore cancel within the scaling factor. In reality, the width of ice-structure interface depends on many aspects such as the cross-sectional geometry ($2/\pi$ perimeter ratio between the circular and rectangular cross-sections), which are not considered for this simplified analysis. The scaling of the global loads from the 23010 test run was executed as follows:

$$F_{ice-scaled}^{Circ} = \lambda_{ice} F_{ice}^{Circ} \tag{6.3}$$

where $F_{ice-scaled}^{Circ}$ represents the ice-induced global loads on the circular cross-section structure from the 23010 test run with the same ice compressive strength and ice thickness as those from the 26020 test run. It is important to note that the compressive strength of ice is dependent on strain rate, which varies during a FLI cycle. For simplicity, it is assumed that the ratio between strain rates for the ice sheets from the different test runs is time-invariant at every instant during a FLI cycle. Thus, although the strain rate changes over the course of a FLI cycle, there is no change in ratio between strain rates—and compressive strengths—for the ice sheets from the different test runs during a FLI cycle.

The ice scaling factor derived herein does not directly apply to global loads on flexible structures, where ice-structure interaction plays a major role in the variation of ice compressive strength and width of ice-structure interface. A change in the global loads on a structure via scaling of ice properties would result in a change in the response of the structure, thereby altering the ice-structure interaction which affects the strain rate of the ice sheet and therefore the global loads. However, the scaling factor can be warily employed when comparing the quasi-static statistical properties of the global loads on the different structures. Henceforth, the ice scaling factor is utilized only as a means to compare the statistical properties of the global loads on the different structures and the time-averaged energy of the system from the specified test runs. Note that all following sections refer to the global loads from the 26020 test run and the scaled global loads from the 23010 test run.

6.1.2. STRUCTURAL PROPERTIES

For the structural properties, simplified linear scaling cannot be performed due to the dynamical nature of the system. The one of the test runs would have to be repeated with structural properties that are identical to the other test run in order to isolate and exclusively compare the effect of cross-section geometry on the ice-induced global loads on the different structures. It was concluded that the differences in structural properties between the 23010 and 26020 test runs were acknowledged in further analysis but could not be altered for the purpose of comparison.

6.2. ICE-INDUCED GLOBAL LOADS

For the comparison of ice-induced global loads between the rectangular and circular cross-section structures, the effects of both the cross-sectional geometry and the regime of ice-induced vibrations were treated. First, in Section 6.2.1, the impact of the difference in cross-sectional shape of the structure is discussed in terms of past studies and a novel approach is given to challenge previous research. Then the ice-induced global loads from the 26020 and 23010 test runs were investigated statistically in Section 6.2.2 with respect to frequency lock-in and comparatively evaluated in Section 6.2.3.

6.2.1. EFFECT OF GEOMETRY ON LOADS

As introduced in Chapter 2 and discussed in Chapter 3, the cross-sectional geometry of the structure at the ice-structure interface can significantly affect the ice-structure interaction. But little focus is given to this topic in literature; consequently, the subject is treated trivially or even is neglected in design standards such as ISO 19906 (ISO 2010). The successive sections respectively elucidate the context of pertinent literature and then provide a derivation for the contrastive impact of cross-sectional shape of a structure on the ice-induced global loads. Additionally, the contribution of ice friction to the derivation is considered.

CLARIFICATION IN RELEVANT LITERATURE

When discussing the effect of cross-sectional shape of the structure on ice-induced vibrations, Hendrikse (2017) referred to a shape factor of 0.9 when comparing loads from a structure of circular cross-section to that of a rectangular cross-section (Korzhavin 1962). Based on general results from the IVOS Phase 2 test runs, a reservation about the general use of this shape factor has developed. Therefore, the work done by Korzhavin (1962) that is relevant to this study was reviewed to particularize the definition and appropriate use of the shape factor as mentioned by Hendrikse (2017).

To examine the effect of the cross-section geometry at the ice-structure interface on the ice-induced global loads of a structure, Korzhavin (1962) conducted a series of experiments. The experiments consisted of indenters of various shapes each being pressed into an ice sample, with and without lateral compression (confinement), at a constant rate of indentation and the loads on each indenter were measured (see Figure 6.1). Of interest to this study were the semicircular and rectangular indenters as shown by $N1$ and $N2$, respectively, in Figure 6.1.

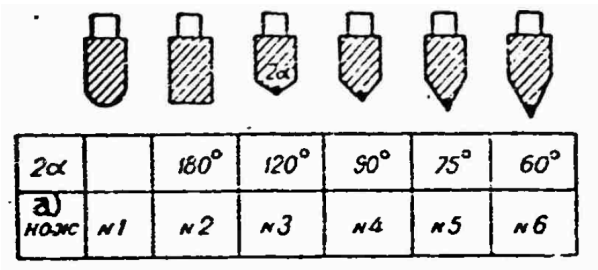

Figure 6.1: Shape of indenters test during experiments from Korzhavin (1962).

The ice samples tested were natural ice taken from a freshwater river; each sample had a size of 120 mm by 200 mm by 70 mm, and were maintained at about 0°C during the testing (see Figure 6.2). Additionally, each ice sample was loaded perpendicularly to the c-axis by the indenter. But it was not specified whether the samples were cut from the surface of the river ice sheet downward in order to obtain an ice sample with realistic granular and crystal layer structure. Furthermore, neither the thickness of each layer of the ice sample nor the properties of the ice directly from the river were stated. The rate of indentation was constant at 0.25 mm/s, corresponding to a strain rate of about 0.002 s^{-1} for the length dimension of 120 mm according to Korzhavin (1962). For full-scale ice, a strain rate of 0.001 s^{-1} generally represents the transition from ductile to brittle deformation of ice (ISO 2010). Because few properties of the ice were explicitly provided by Korzhavin (1962), it was assumed that the ice deformation acted with transitional deformation behavior during the experiments due to the order of magnitude of the computed strain rate.

Based on the experiments, it was concluded by Korzhavin (1962) that a structure with a semicircular cross-section would experience 90 % of the ice-induced loads when compared with an equivalent structure of rectangular cross-section. Specifically, the structures would have equivalent widths but the different geometries at the ice-structure interface and would experience the same ice-induced loading conditions. However, this form coefficient of 90 % may only be valid for strain rates, according to Korzhavin (1962), on the order of 0.001 s^{-1}. Additionally, this factor should only be applicable to structures subjected to finite ice floes where the stressed state throughout the ice floe plays a major role in the deformation of the ice and the formation of microscopic and macroscopic cracks. In other words, the form coefficient derived from the experiments is not valid for semi-infinite level floating ice sheets for which brittle ice deformation predominantly governs the failure mechanisms.

Since not explicitly stated, it may be assumed that the ice sample tested was not floating, which further deviates the results from the experiments from realistic applications. Moreover, the experiments implemented

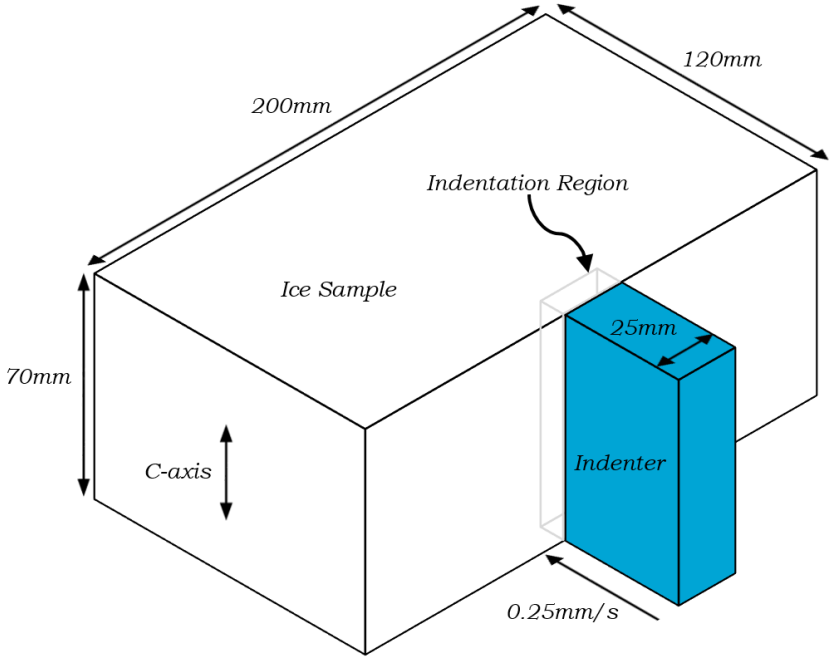

Figure 6.2: Schematic of experiment with rectangular indenter as interpreted from Korzhavin (1962).

a model-scale indenter with full-scale ice and no explicit assessment was made regarding the effect of the size of the indenter relative to the size of the ice grains. Korzhavin (1962) states that the maximum ice-induced loads on the various indenters were recorded, which were then used to determine form coefficients. But not mentioned were the amounts of indentation necessary for maximum loads to occur or the type of material deformation or failure mechanisms which were governing before, during, or after the maximum loads were recorded. It can be presumed that the entire width of the semicircular indenter was needed to achieve the maximum loads for that shape of indenter, but this may not have been the case if radial cracks formed prior to full width penetration of the indenter.

It can be concluded that this form coefficient should be applied with great caution since there is much uncertainty in general about the results from the experiments. The form coefficient should only be used under similar conditions as those specified in the experiments.

GEOMETRIC FORCE CONTRAST

When a floating, level ice sheet impinges on a vertically sided structure, a global force is experienced by the structure and is caused by pressure along the ice-structure interface. The pressure from the ice acts orthogonal to the surface of the structure, regardless of the direction of motion of the ice sheet. But the majority of force from the ice pressing against the structure acts in the direction of the ice motion. Thus, to determine the global force on the structure in a specific direction, the geometry of the ice-structure interface must be considered. For the sake of brevity, the effect of difference in cross-sectional geometry on the manner that the ice induces a force on the structure is referred to as the geometric force contrast.

For rigid vertically sided structures, and assuming uniform thickness of a homogeneous, semi-infinite ice sheet, the scenario can be assumed as two-dimensional with respect to a view from above and applied to the two different cross-section structures of interest (see Figure 6.3). Under the assumption of uniform ice thickness, the ice pressure distribution along the ice-structure interface can be treated as a force distribution. The distribution of force per unit length is expressed as f_{ice} in Figure 6.4 and is distributed over the portion of the perimeter which is most likely to experience ice pressure. Additionally, these distributions correspond to the regions mostly covered by the large tactile sensors on the model structures in the test runs. Note that for the rectangular cross-section structure in Figure 6.4a, the force distribution extends along the sides of the structure and is marked with dotted lines. It is improbable that pressure from ice crushing occurs along the sides of this structure, but transfer of pressure from the intact ice sheet to the structure via confinement or ice rubble is possible.

To find the global force experienced by each model structure, the force distribution is integrated over the

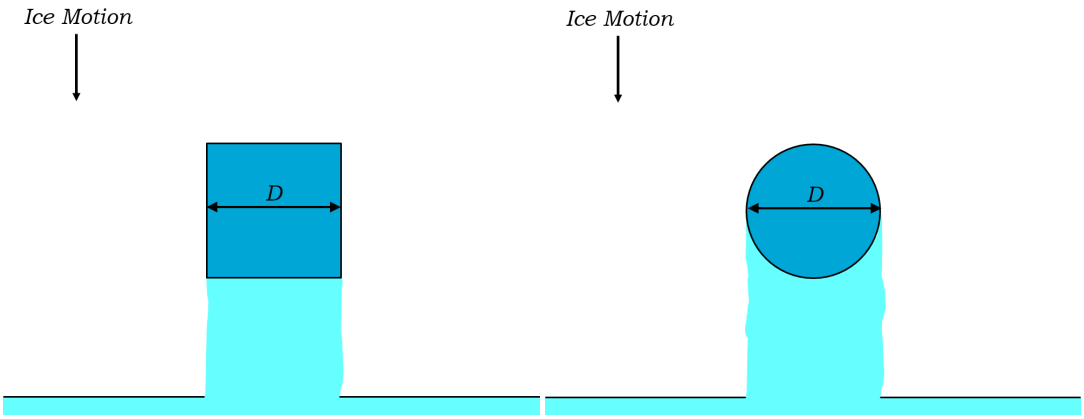

(a) Schematic for rectangular cross-section. (b) Schematic for circular cross-section.

Figure 6.3: Schematics of structures of different cross-section subjected to an impinging ice sheet.

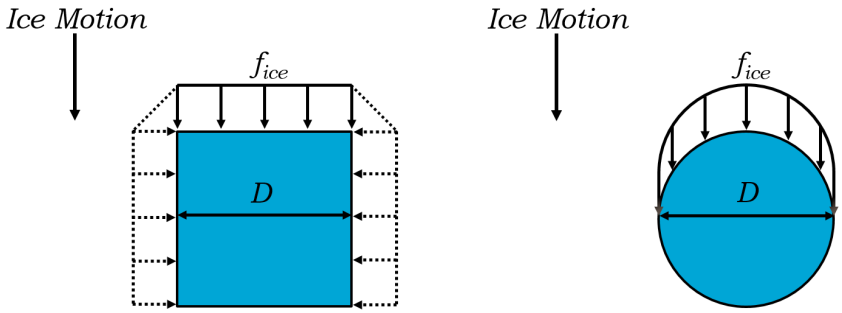

(a) Schematic for rectangular cross-section. (b) Schematic for circular cross-section.

Figure 6.4: Schematic of ice pressure distributions for structures of different cross-section subjected to an impinging ice sheet. A uniform pressure distribution is illustrated for simplicity.

indicated perimeter of the structure. For a uniform distribution of ice pressure along the indicated perimeter of the structure, the resulting global force acts in the direction of ice motion because the force components perpendicular to the ice motion are negated due to symmetry of the structure. In reality, a uniform pressure distribution might be observed only for ice sheets moving at very low velocity where the creep governs the ice failure mode. For ice-induced vibrations to develop, the ice sheet needs to move against a flexible structure with velocities great enough to cause the ice to fail in crushing. Based on observations from the Phase 2 test runs, it can be affirmed that a uniform pressure distribution of some duration from ice crushing is highly unlikely. Although a force distribution caused by ice crushing would be non-uniform both spatially and temporary, the force distribution selected for this scenario, f_{ice}, is assumed uniform for simplicity.

As an aside, the global force computed from a non-uniform force distribution does not always act in the direction of ice motion, but a major component of global force acts in that direction. Moreover, not only does the ice crushing cause non-uniformity of normal force distribution but also the cross-sectional geometry of the structure causes the non-uniform force distribution to act in certain directions along the perimeter of the structure. In order to aptly compare the global forces from the structures of different cross-sectional geometries, the global force in the direction of ice motion must be isolated for each structure.

To determine the global force acting in the direction of ice motion for each structure, the force distribution acting in the direction of ice motion is isolated. For the rectangular cross-section structure, shown in Figure 6.5, the normal force distribution acting along the front of the structure, which is orthogonal to the direction of ice motion, contributes to the global force in the direction of ice motion. The ice-structure friction force caused by the intact ice sheet and ice rubble on the sides of the structure also contributes to the global force in the direction of ice motion, but is surmised to contribute marginally and therefore neglected in this derivation. The ice-structure friction force is considered in the next section.

The global force F_{Rect} in direction of ice motion for the rectangular cross-section structure with an ideal-

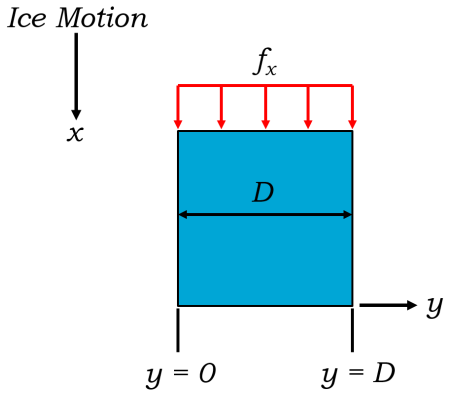

Figure 6.5: Schematic of ice pressure distribution in the direction of ice motion for a rectangular cross-section structure subjected to an impinging ice sheet. A uniform pressure distribution is illustrated for simplicity.

ized uniform force distribution f_x in the direction of ice motion can be easily determined as follows:

$$\begin{aligned} F_{Rect} &= \int_0^D f_x dy \\ &= \int_0^D f_{ice} dy \\ &= f_{ice} D \end{aligned} \tag{6.4}$$

where the force distribution is integrated along the front side of the structure with width D and the force per unit length is interchangeable between the ice force and the force in the direction of ice motion.

For the circular cross-section structure, the force distribution in direction of ice motion, which acts along the front half-circumference of the structure, must first be decomposed into components that are normal and tangential to the surface of the structure (Willems 2016). As shown in Figure 6.6, the contribution to the global force in the direction of ice motion is taken as the integral of some component of the force normal to the surface of the structure. The ice-structure friction force along the indicated perimeter of the structure also adds to the global force in the direction of ice motion, but was neglected for this derivation. The ice-structure friction force for this case is considered in the next section.

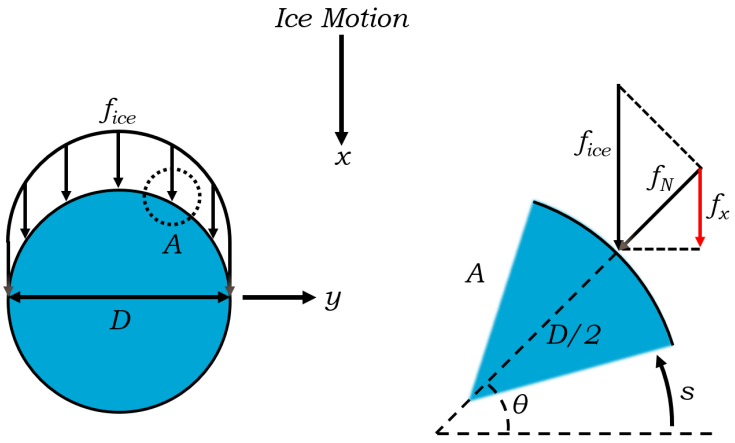

Figure 6.6: Schematic of ice pressure distribution in the direction of ice motion for a circular cross-section structure subjected to an impinging ice sheet. A uniform pressure distribution is illustrated for simplicity.

The global force in the direction of ice motion for the circular cross-section structure with an idealized uniform force distribution in the direction of ice motion is determined by first calculating the force per unit length f_N that is normal to the surface of the structure:

$$f_N = f_{ice} \sin\theta \tag{6.5}$$

where θ is angle from the axis orthogonal to ice motion (y-direction) to the location of interest (see detail A Figure 6.6). Next, the force per unit length f_x in the direction of ice motion is computed as follows:

$$f_x = f_N \sin\theta \tag{6.6}$$

which has the same trigonometric function as in Equation 6.5. Prior to integrating the force per unit length in the direction of ice motion, the relationship between the angle θ and the distance s along the perimeter of the structure is given:

$$\begin{aligned} s &= \frac{D}{2}\theta \\ ds &= \frac{D}{2}d\theta \end{aligned} \tag{6.7}$$

where D is the diameter of the structure and operator $d[*]$ is the infinitesimal change or derivative. The global force in the direction of ice motion for the circular cross-section structure is initially formulated as follows:

$$\begin{aligned} F_{Circ} &= \int_0^{\pi} f_x\left(\frac{D}{2}d\theta\right) \\ &= \int_0^{\pi} [f_{ice}\sin^2\theta]\left(\frac{D}{2}d\theta\right) \end{aligned} \tag{6.8}$$

where the integration is performed over the half-circumference using the θ angle. Given the symmetry along the x-direction axis, Equation 6.8 is reformulated:

$$F_{Circ} = 2\int_0^{\pi/2} [f_{ice}\sin^2\theta]\left(\frac{D}{2}d\theta\right) \tag{6.9}$$

and inserting Equation 6.7 in Equation 6.9 yields the following:

$$F_{Circ} = 2f_{ice}\int_0^{\pi D/4} [\sin^2\left(\frac{2s}{D}\right)]ds \tag{6.10}$$

where the integral is performed over the length of the perimeter of the structure and the ice force per unit length f_{ice} is given as a constant. Using a trigonometric half-angle identity, the integral in Equation 6.10 can be readily solved.

$$\begin{aligned} F_{Circ} &= 2f_{ice}\int_0^{\pi D/4} [\sin^2\left(\frac{2s}{D}\right)]ds \\ \sin^2\left(\frac{2s}{D}\right) &= \frac{1}{2}\left(1-\cos\left(2\frac{2s}{D}\right)\right) \\ F_{Circ} &= 2f_{ice}\int_0^{\pi D/4} [\frac{1}{2}\left(1-\cos\left(2\frac{2s}{D}\right)\right)]ds \\ &= \frac{2}{2}f_{ice}\left[\left(\frac{\pi D}{4}-0\right)-\frac{D}{4}\left(\sin\left(\frac{4}{D}\frac{\pi D}{4}\right)-\sin\left(\frac{4}{D}0\right)\right)\right] \\ &= \frac{\pi}{4}f_{ice}D \end{aligned} \tag{6.11}$$

Comparing the ratio of global forces between the different cross-section structures yields the following:

$$\begin{aligned}\frac{F_{Circ}}{F_{Rect}} &= \frac{\frac{\pi}{4} f_{ice} D}{f_{ice} D} \\ &= \frac{\pi}{4} \\ &\approx 0.79\end{aligned} \tag{6.12}$$

where the approximate ratio between the global forces of the circular and rectangular cross-section structures is about 79 %. For an idealized case where there is an equivalent uniform force distribution acting on each of the structures, it can expected that the circular cross-section structure will experience about 79 % of the global force that is experienced by the rectangular cross-section structure. However, the ice pressure, and thus the force distribution, on each of the structures during ice crushing is not uniform. Furthermore, the ice-structure interaction is not considered as the structures are assumed rigid in this scenario. Therefore, this value may not be expected for the global force ratio between the different structures but can be treated as a guideline for analysis.

From Hendrikse (2017), the numerical model was extended in a preliminary manner to incorporate two-dimensional in-plane ice-structure interaction. Note that frictional and sliding forces were neglected for this extended model. Comparing rigid rectangular and circular cross-section structures of equivalent diameter and identical ice properties, Hendrikse (2017) discovered that—in the direction of ice motion—the mean and maximum global loads on the circular cross-section structure were between 80 % and 85 % of the global loads on the rectangular cross-section structure. These results are in fair agreement with the geometric force contrast ratio derived previously. Nevertheless, both results are preliminary and therefore inconclusive without further substantiation.

CONTRIBUTION OF ICE FRICTION

Besides the global loads related to ice deformation and consequential failure mechanisms of the ice sheet, friction force from ice sliding along the ice-structure interface also contributes to the global loads experienced by the structure. Typically, the ice friction force does not comprise a majority of the ice-induced global loads, but the ice friction force is also not irrefutably negligible. Ergo, the ice friction force is assessed analytically and then compared with other ice-induced loads, e.g. ice crushing. The following assessment is made conservatively and with many simplifying assumptions.

For vertically sided structures, and assuming uniform thickness of a homogeneous, semi-infinite ice sheet, the scenario can again be assumed as two-dimensional with respect to a view from above and applied to the two different cross-section structures of interest (see Figure 6.3). To realize a very conservative ice friction force scenario, it is assumed that there is full contact along the ice-structure interface and that the force considered on the structure is from the intact ice sheet sliding at a constant speed along the structure at the ice-structure interface. These assumptions imply that the ice sheet acts as an incompressible fluid which flows around the structure and only exerts a force on the structure via Coulomb dry kinetic (dynamic) friction. Technically, there has to be a force acting orthogonal to the surfaces of the ice and structure in order for friction to be present. For this scenario, the ice-induced force on the structure in the direction of ice motion is decomposed into a force normal to the surface of the structure, which is then used to compute the ice friction force. The friction force per unit length f_f along the ice-structure interface is determined as follows:

$$f_f = \mu_k f_N \tag{6.13}$$

where μ_k is the kinetic ice-structure friction coefficient and f_N is the force per unit length that is normal to the surface between the ice and structure.

In terms of the force that is perpendicular to the surface of the structure and the corresponding friction force, there are two cases to consider for the rectangular cross section structure (see Figure 6.7). The first case is along the front of the structure where the normal force f_N is the same as the force in the direction of ice motion f_{ice} (detail A in Figure 6.7). The ice friction force f_{fy} then acts parallel to the front of the structure and does not contribute to the force in the direction of ice motion. The second case is along the sides of the structure where normal force cannot originate from the ice-induced force in the direction of ice motion because the side is parallel to the ice motion. Maybe the normal force could be supplied by the confinement of the ice sheet, f_{N-con}, but not enough is known about the confinement in this scenario to determine the normal force on the sides of the structure (detail B in Figure 6.7). In conclusion, the ice friction force f_{fx} in the direction of ice motion for the rectangular cross-section structure cannot be known and thus is disregarded.

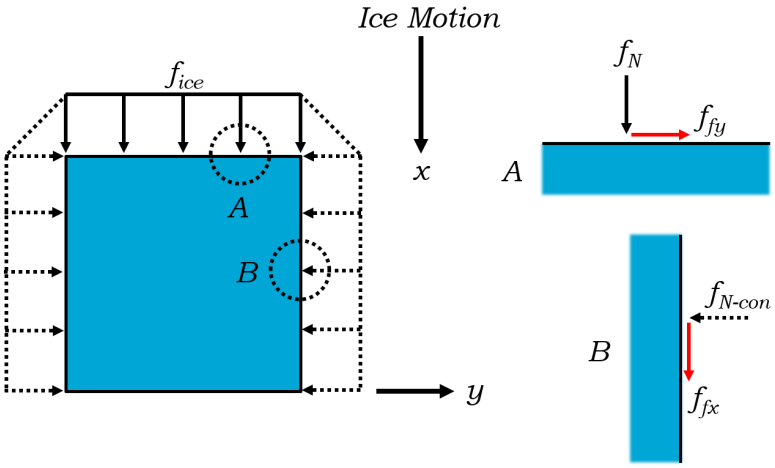

Figure 6.7: Schematic of ice pressure distribution in the direction of ice motion and corresponding friction force for a rectangular cross-section structure subjected to an impinging ice sheet. A uniform pressure distribution is illustrated for simplicity.

For the circular cross section structure, the magnitude and direction of the ice friction force are dependent on the location along the front half-circumference (see Figure 6.8). Most importantly, the ice friction force in the direction of ice motion (x-direction) is dependent on this location along the perimeter of the circular cross section, which can be described by again an angle θ from the axis orthogonal to ice motion (y-direction) to the location of interest (see detail A in Figure 6.8).

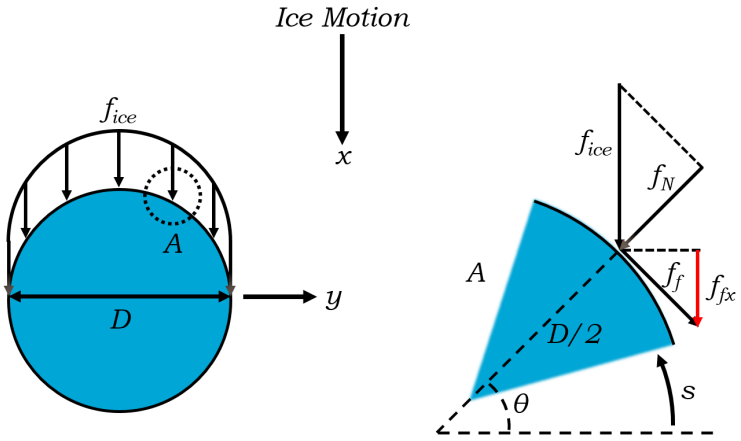

Figure 6.8: Schematic of ice pressure distribution in the direction of ice motion and corresponding friction force for a circular cross-section structure subjected to an impinging ice sheet. A uniform pressure distribution is illustrated for simplicity.

To determine the x-direction ice friction force per unit length f_{fx}, a few steps are taken. First, the ice force per unit length f_{ice} is decomposed into the normal force per unit length f_N as in Equation 6.5. Using this normal force, the friction force per unit length which is parallel to the ice-structure surface f_f can be computed as in Equation 6.13. Finally, the friction force is decomposed into the x-direction friction force per unit length f_{fx} as follows:

$$f_{fx} = f_f \cos\theta \tag{6.14}$$

where the trigonometric function cosine is present as opposed to the sine function in Equation 6.5, in accordance with Willems (2016). Combining Equation Equation 6.5, Equation 6.13, and Equation 6.14 yields the following relationship.

$$f_{fx} = \mu_k f_{ice} \sin\theta \cos\theta \tag{6.15}$$

Based on Equation 6.15, the ratio between the x-direction ice friction force per unit length f_{fx} and the x-direction ice force per unit length f_{ice} is at most 50 % of the kinetic ice-structure friction coefficient. However,

the global forces are most relevant, which require the forces per unit length to be integrated over the half-circumference of the circular cross-section structure. Therefore, the angle θ is again related to the distance s along the circumference as in Equation 6.7. The global force from ice friction is initially formulated as follows:

$$\begin{aligned} F_{fx} &= \int_0^{\pi} [f_{fx}]\left(\frac{D}{2}d\theta\right) \\ &= \int_0^{\pi} [\mu_k f_{ice} \sin\theta\cos\theta]\left(\frac{D}{2}d\theta\right) \end{aligned} \tag{6.16}$$

where the integration is performed over the half circumference using the θ angle. Given the symmetry along the x-direction axis, Equation 6.16 is reformulated.

$$F_{fx} = 2\int_0^{\pi/2} [\mu_k f_{ice} \sin\theta\cos\theta]\left(\frac{D}{2}d\theta\right) \tag{6.17}$$

Inserting Equation 6.7 into Equation 6.17 grants:

$$F_{fx} = 2\mu_k f_{ice} \int_0^{\pi D/4} [\sin\left(\frac{2s}{D}\right)\cos\left(\frac{2s}{D}\right)]ds \tag{6.18}$$

where a trigonometric double angle formula can be implemented to solve the integral. The global force F_{fx} from ice friction is determined in the following integration.

$$\begin{aligned} F_{fx} &= 2\mu_k f_{ice} \int_0^{\pi D/4} [\sin\left(\frac{2s}{D}\right)\cos\left(\frac{2s}{D}\right)]ds \\ \sin\left(\frac{2s}{D}\right)\cos\left(\frac{2s}{D}\right) &= \frac{1}{2}\sin\left(2\frac{2s}{D}\right) \\ F_{fx} &= 2\mu_k f_{ice} \int_0^{\pi D/4} [\frac{1}{2}\sin\left(\frac{4s}{D}\right)]ds \\ &= -\frac{2}{2}\mu_k f_{ice}\frac{D}{4}\left[\cos\left(\frac{4}{D}\frac{\pi D}{4}\right) - \cos\left(\frac{4}{D}0\right)\right] \\ &= \frac{1}{2}\mu_k f_{ice} D \end{aligned} \tag{6.19}$$

Comparing Equation 6.19 and Equation 6.11 results in the following:

$$\begin{aligned} \frac{F_{fx}}{F_{Circ}} &= \frac{\frac{1}{2}\mu_k f_{ice} D}{\frac{\pi}{4} f_{ice} D} \\ &= \frac{2}{\pi}\mu_k \\ &\approx 0.64\mu_k \end{aligned} \tag{6.20}$$

which indicates that the ratio between x-direction global force from ice friction and x-direction global force not from ice friction is at most 64 % of the friction coefficient. Based on a coefficient of friction between the ice and the tactile sensors of $\mu_k = 0.1$ as provided by HSVA, the resulting x-direction global force from ice friction would be 6.4 % of the x-direction global force not from ice friction. This scenario is possibly valid for very slow ice velocities when there is nearly complete contact at the ice-structure interface and the ice deforms plastically in the creep failure mode. Important to note is the fact that the friction coefficient is dependent on ice velocity (Løset et al. 2006). Since the ice failure mode also changes with ice velocity, the interaction between ice and structure and the friction coefficient vary, thereby restricting the aforementioned scenario to that of ice which fails in creep.

For high ice velocities where the ice deforms with brittle behavior, ice crushing can govern the ice failure mode. Under these conditions, ice rubble subsequently forms at the ice-structure interface and can contribute to the ice friction force. However, much is unknown about the manner by which the ice rubble adds to the friction force or the magnitude of that force. Additionally, the ice crushing failure mechanism typically has stochastic, non-simultaneous failure of ice at the ice-structure interface, which means that the contact area is less than that for the creep of ice. Generally, it can be concluded that the ice friction force on the circular cross-section structure should comprise no more than about 5 % of the x-direction total global force on the structure. For the purpose of this preliminary and simplified analysis, the ice friction force on each of the different structures can be neglected.

6.2.2. STATISTICAL REVIEW OF LOADS

As a preliminary investigation of the time series of global forces in the x-direction from the 26020 and 23010 test runs, a normalized probability distribution and fitted Gaussian probability density function of the forces from each test run were computed as shown in Figure 6.9. Additionally, a summary of statistical values of the global forces from each test run is given in Table 6.1. Considering that the global loads from the 23010 test run were only scaled by the ice thickness and compressive strength from the 26020 test run, the lower force statistics for the circular cross-section structure when compared to that of the rectangular cross-section structure could be attributed to the following:

- Difference in flexural strength between the test runs and the pervasiveness of buckling failure for the ice of lower flexural strength;
- Difference in cross-sectional geometry and its impact on
  - the formation of radial cracks and subsequent formation of circumferential cracking from ice buckling failure;
  - the magnitude and shape of the stress distribution in the ice in proximity of the ice-structure interface;
- Difference in structural properties and the consequential difference in dynamic response between the test runs;

or combinations thereof. For the 23010 test run, the lower flexural strength of ice may explain the lower maximum and minimum of loads as the pervading failure of ice in buckling may have limited the maximum load to that of the critical buckling load and permitted near-zero minimum loads from momentary loss of contact between the intact ice sheet and the structure. By assuming a normal distribution for the stochastic nature of ice crushing failure, and possibly buckling failure, the mean force for the circular cross-section structure can be justified as approximately the median of the force distribution. Ergo, the mean force should be and was reduced for the circular cross-section structure when compared to the mean of the rectangular cross-section structure. The buckling failure for the 23010 test run may have acted as a limiting mechanism for the perpetuation of ice-induced vibrations in frequency lock-in regime and also may have caused a more Gaussian force distribution; this limiting mechanism is addressed in Section 6.4. The force distribution for the 26020 test run was almost Gaussian but with a shift of force distribution towards the maximum, which may be caused by the load amplification of the frequency lock-in regime (see Section 6.2.3).

The ratios of force statistics, displayed in Table 6.1, serve as a preliminary basis comparison between the structures. However, because of the numerous potential sources for the differences in the statistics between the structures, distinct conclusions were not drawn from these force ratios.

6.2.3. ANALYSIS FOR FREQUENCY LOCK-IN

As elaborated in Section 3.2.2, the frequency lock-in regime of ice-induced vibrations develops in part due to the change in deformation and failure behavior of the ice. Thus, it was necessary to isolate and analyze the global loads resulting from the different ice behavior for each test run with the subsequent method.

The peak forces caused by ductile ice deformation were defined by the largest local maxima with a frequency that was very similar to the dominant natural frequency of the system. The mean force of interest in the frequency lock-in regime was the average of the forces not caused by transitional or ductile ice deformation that were induced by the prolonged low relative velocity between the structure and the ice; i.e.

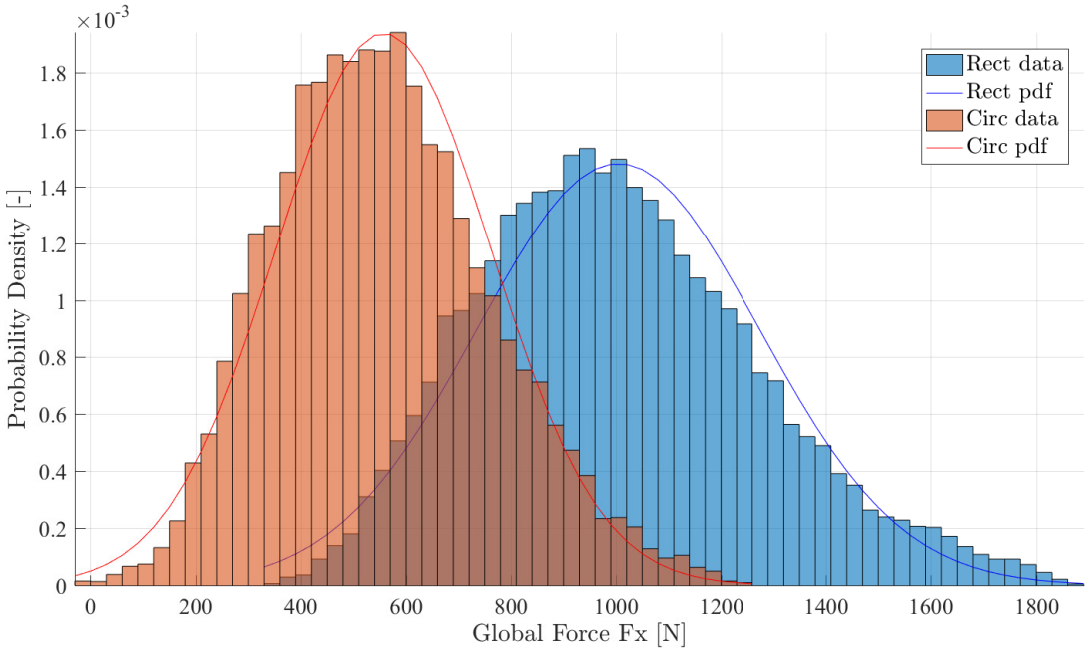

Figure 6.9: Normalized probability distribution and fitted Gaussian probability density function of the global forces in the x-direction from the 26020 ($Rect$) and 23010 ($Circ$) test runs. The probability density function is abbreviated to pdf in the legend.

Table 6.1: General statistical summary and comparison of the global forces in the x-direction from the 26020 and 23010 test runs.

Test run	26020	23010	**Circ/**
Cross-sectional geometry	Rectangular	Circular	**Rect [-]**
Mean of force [N]	1004	557	0.55
Standard deviation of force [N]	269	206	0.76
Maximum of force [N]	1887	1248	0.66
Minimum of force [N]	336	-24	-0.07

mean force was the average of the forces caused by brittle ice deformation and crushing failure. The cyclical range of forces caused by non-brittle ice deformation were discerned using the peak forces as presented in Figure 6.10: the initial point was chosen as the nearest local minimum preceding the peak force and the final point was selected as the nearest local maximum following the peak force. The initial point corresponded to the time when the relative velocity was low and the ice deformation behavior could change from brittle to transitional. The final point was chosen based on the premise that the large global load increase and consequential collapse only occurred with the frequency lock-in regime governing. The effect of frequency lock-in on the global loads then was assumed mitigated by the following local maximum where brittle ice behavior again dominated. Note that, in Figure 6.10 and for the following analysis, the blue line refers to global force caused by brittle ice deformation behavior and the red line corresponds to global force caused by transitional ice behavior and the subsequent failure of ice as a consequence of the frequency lock-in load amplification.

As described by Ziemer & Hinse (2017), the load amplification ΔF from frequency lock-in during the build-up phase is determined as follows:

$$\Delta F = \bar{F}_{peak} - \bar{F}_{CBR} \tag{6.21}$$

where $\bar{F}_{peak}$ is the mean peak force as a result of the build-up phase of the frequency lock-in regime and $\bar{F}_{CBR}$ is the mean force exclusively caused by ice failure with brittle behavior (similar to continuous brittle crushing regime abbreviated CBR). Note that the mean values are dependent on the number of frequency lock-in cycles considered when computing the frequency lock-in load amplification ΔF.

Due to the time-variant mean of both test runs and the pervasiveness of buckling ice failure during the 23020 test run, a time series of about 1.0 s was selected for from each test run that possessed evident charac-

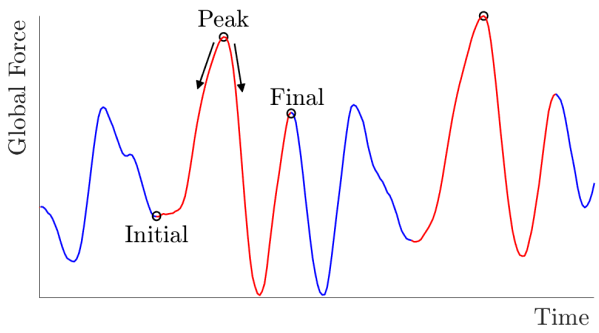

Figure 6.10: Illustration of method to determine range of ice-induced global force caused specifically by frequency lock-in regime.

teristics of the frequency lock-in regime. Additionally, the truncated time series for each test run was chosen based on highest observable mean force for the given duration within the entire time series. The short duration was unavoidable since the buckling failure limited the perpetuation of many clear frequency lock-in cycles for the 23010 test run; the duration for the 26020 test run was chosen to match that of the 23010 test run. For the 26020 and 23010 test runs, the global loads were assessed as portrayed in Figure 6.11 and Figure 6.12 by using the aforementioned method of discrimination in ice deformation behavior. Accompanying the global forces in Figure 6.11 and Figure 6.12 are the relative velocities and displacements, which illustrate the defining features of the frequency lock-in regime: the displacement is quasi-harmonic, the relative velocity is periodically low (near zero) for some duration, and the load amplification can be observed to initiate during the period of low relative velocity. The affect of the bending of the 6-component scale on frequency lock-in for both test runs can be betokened by momentary decrease in relative velocity during the relative velocity maxima as well as the succeeding force peak after the load amplification peak force. Also important to identify is the negative relative velocity during each frequency lock-in cycle, which results in a reduction in the global load preceding the load amplification. Under the assumption that buckling ice failure did not significantly affect the frequency lock-in cycles and resulting global loads during the selected time series of the 23010 test run, the global loads from both test runs were compared for the frequency lock-in regime in the next section.

COMPARATIVE ANALYSIS FOR FREQUENCY LOCK-IN

Again, the normalized probability distribution and fitted Gaussian probability density function of the global loads from each test run were determined, but for the truncated time series in this case (see Figure 6.13). Furthermore, a review and comparison of statistics for the truncated time series of forces from the 26020 and 23010 test runs are provided in Table 6.2. It can be observed from Figure 6.13 that the general mean forces between the test runs were more similar in this case, and the near-zero loads caused by buckling ice failure were not included in the range of forces from the 23010 test run. For the forces from brittle ice behavior, the statistical ratios between the circular and rectangular cross-section structures were similar to the previously derived geometric force contrast ratio of 0.79. However, for the peak forces caused by frequency lock-in load amplification, the ratios between the structures for the statistics vary notably and were not similar to the geometric force contrast ratio. Moreover, the ratio between structures of load amplification was markedly different from the geometric force contrast ratio.

It cannot be presumed that a time series of global loads of 1.0 s for each test run is representative of the forces for the frequency lock-in regime for the given ice and structural properties. For this study, such a small sample size of frequency lock-in for each test run was necessary so that the time series from the 23010 test run would not be influenced by buckling failure. Thus, given the circumstances, the 1.0 s time series for each test run was treated superficially and the ratios between the various statistical properties were considered qualitatively indicative of differences between the structures. Specifically, the circular cross-section structure experienced lower global loads than those of the rectangular cross-section during frequency lock-in due to the difference in cross-sectional shape, assuming that the lower flexural strength of ice in the 23010 test run did not significantly govern the ice-induced global loads on the circular cross-section structure.

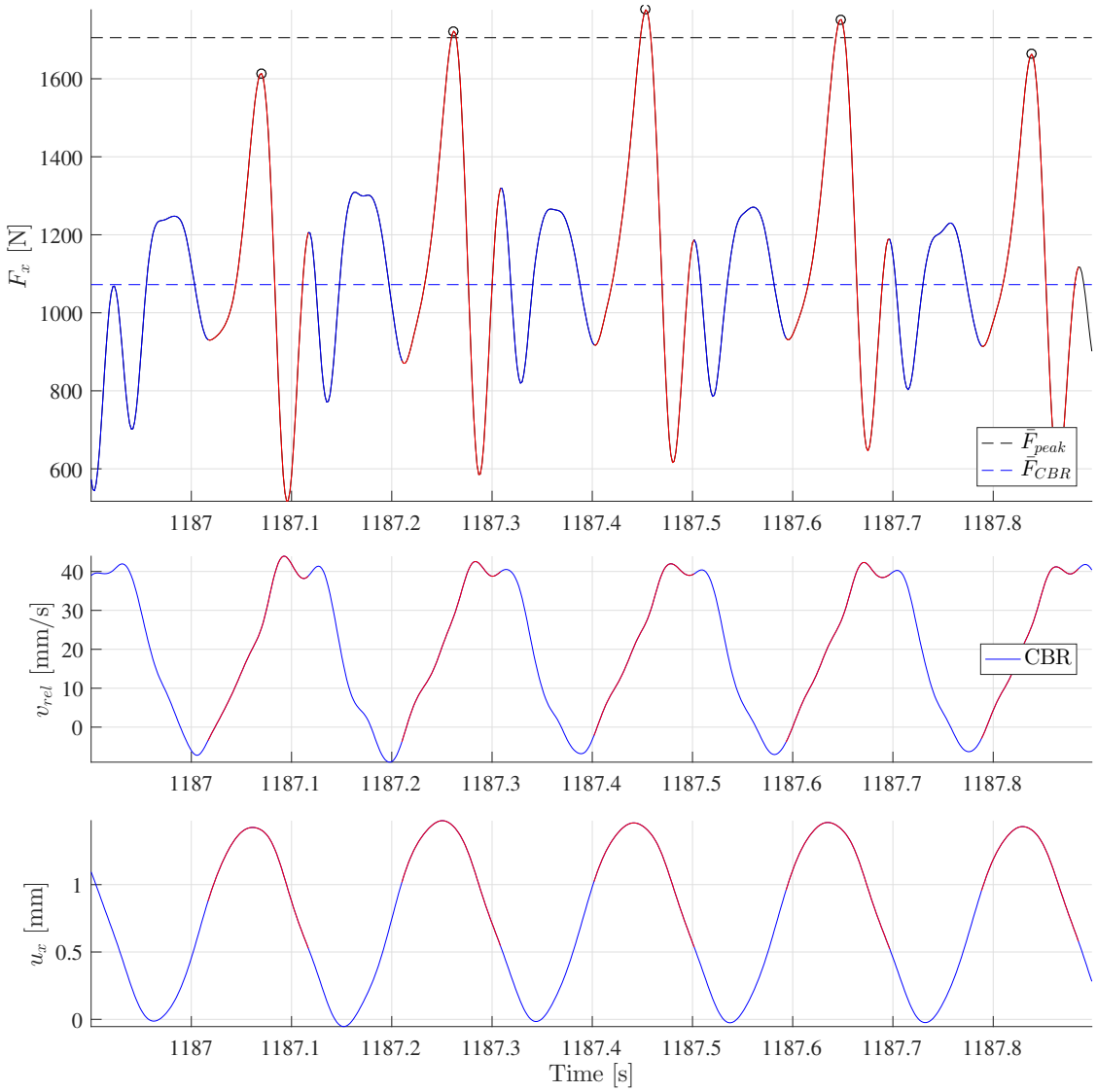

Figure 6.11: Ice-induced global force analysis and corresponding relative ice-structure velocity and structural displacement in the x-direction for 26020 test run.

6.3. ENERGY OF THE SYSTEM

For the frequency lock-in regime of ice-induced to be sustained, the energy imparted from the ice to the structure must be at least equal to the energy dissipated by the structure. The energy from the ice-structure interaction E_{ice} per frequency lock-in cycle is determined as follows:

$$E_{ice} = \int_0^{T_{nat}} \left(F_{ice}\dot{u}_s\right) dt \tag{6.22}$$

where T_{nat} is the dominant natural period of the system, F_{ice} is the ice-induced force on the structure, and $\dot{u}_s$ is the velocity of the structure. The natural period of the structure differs slightly from the period of a frequency lock-in cycle, but this nuance is assumed negligible for the case of computing the energy into the system. The energy dissipated by the structure during each cycle, referred to as E_s, is calculated as follows:

$$E_s = 2\zeta\omega_{nat} m_{sys} \int_0^{T_{nat}} \left(\dot{u}_s\right)^2 dt \tag{6.23}$$

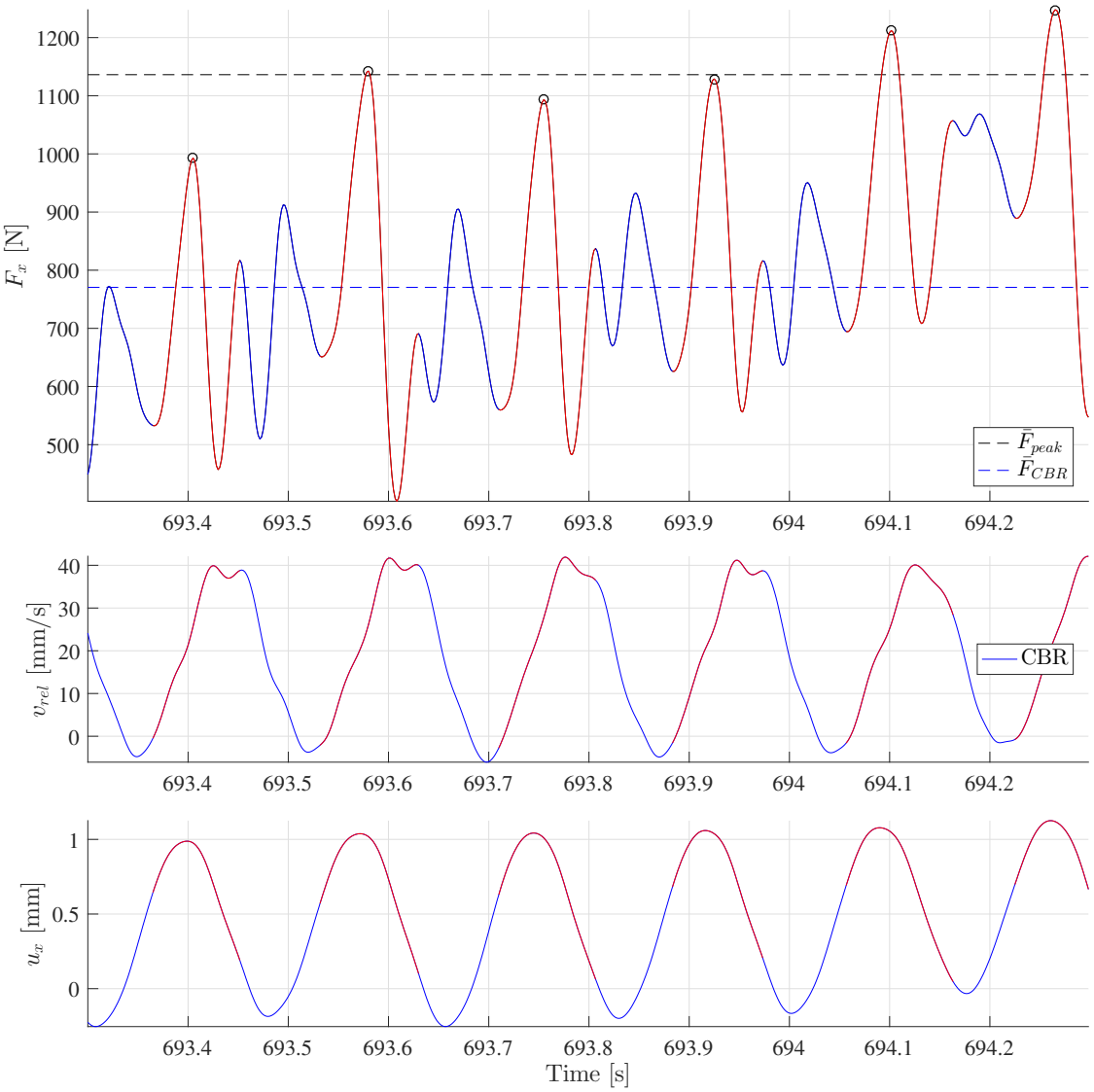

Figure 6.12: Ice-induced global force analysis and corresponding relative ice-structure velocity and structural displacement in the x-direction for 23010 test run.

where ζ is the damping ratio, ω_{nat} is the dominant natural angular frequency of the system, and m_{sys} is the mass of the system. Note that the damping ratio was found from the relaxation tests to be proportional to the amplitude of the structural displacement; therefore, the damping ratio is reincorporated into the time integral as follows:

$$E_s = 2\omega_{nat} m_{sys} \int_0^{T_{nat}} \zeta\left(u_s(t)\right)\left(\dot{u}_s\right)^2 dt \tag{6.24}$$

where ζ is now a function of the structural displacement u_s as a function of time t. Energy is dissipated by the system via structural damping on the order of 1 % to 3 % and is an irreversible process, meaning that the energy out is always has a non-negative sign convention. But the sign convention of the energy into the system from ice-structure interaction can be negative, indicating that energy is extracted from the system by the ice-structure interaction. This convention for negative energy refers to the time when the structure is moving in opposition to the direction of ice motion and thus the ice crushing against the structure dissipates the kinetic energy and retards the motion of the structure.

For a relatively short time series, the energy from ice-structure interaction per frequency lock-in cycle precludes net energy from preceding cycles. Therefore, the continuous energy from ice-structure interaction

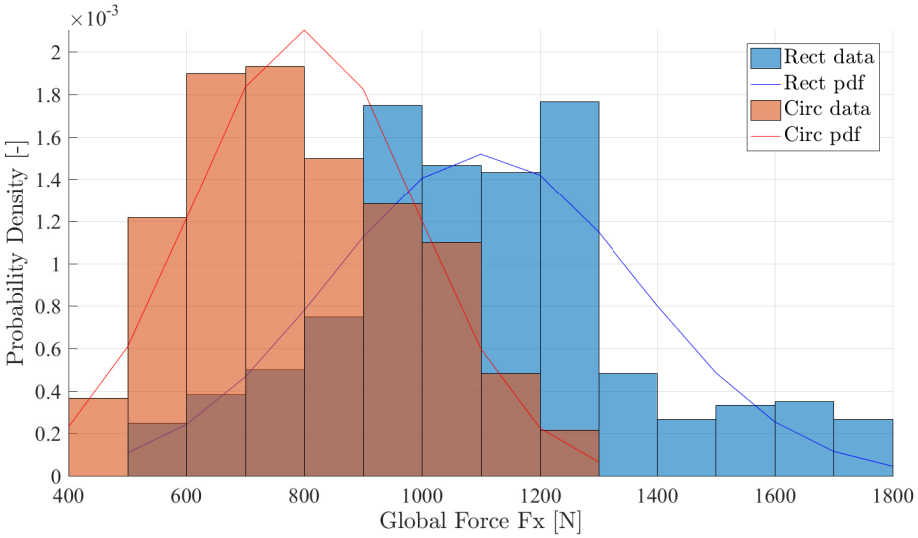

Figure 6.13: Normalized probability distribution and fitted Gaussian probability density function of the truncated time series of global forces in the x-direction from the 26020 (*Rect*) and 23010 (*Circ*) test runs. The probability density function is abbreviated to *pdf* in the legend.

Table 6.2: Statistical summary of the global force analysis and comparison between the 26020 and 23010 test runs for the frequency lock-in regime.

Test run	26020	23010	**Circ./**
Cross-sectional geometry	Rectangular	Circular	**Rect.** [-]
Force from brittle ice behavior [N]			
Mean	1072	771	0.72
Standard deviation	176	147	0.83
Maximum	1319	1069	0.81
Minimum	544	449	0.83
Peak force [N]			
Mean	1705	1136	0.67
Standard deviation	67	90	1.35
Maximum	1777	1248	0.70
Minimum	1613	993	0.62
Load amplification from frequency lock-in [N]	633	366	0.58

is considered as follows:

$$E_{ice}(t) = \int_{t}^{t+t_s} \left(F_{ice}(\tau)\,\dot{u}_s(\tau)\right) d\tau \tag{6.25}$$

where the integral is computed from some time instant t to the sum of that and the incremental time step t_s. For comparison, the continuous energy dissipated by the structure is treated in the same manner:

$$E_s(t) = 2\omega_{nat} m_{sys} \int_{t}^{t+t_s} \zeta(u_s(\tau)) \left(\dot{u}_s(\tau)\right)^2 d\tau \tag{6.26}$$

where the continuous energy into and out of the system can be contrasted per incremental time step t_s. Finally, the net energy E_{net} from ice-structure interaction and from structural dissipation—either as time-integrated or continuous—is computed as follows:

$$E_{net} = \pm E_{ice} - E_s \tag{6.27}$$

where the ± symbol is a reminder that the energy from ice-structure interaction can either be added to or subtracted from the total energy of the system. In addition to the energy into and out of the system, the total energy of the system in time comprising the kinetic and spring potential energy was investigated. The kinetic energy E_{kin} of the system is computed as follows:

$$E_{kin}(t) = \frac{1}{2} m_{sys} \left[\dot{u}_s(t) \right]^2 \tag{6.28}$$

and the spring potential energy E_{spr} of the system is determined as follows:

$$E_{spr}(t) = \frac{1}{2} k_{linear} \left[u_s(t) \right]^2 \tag{6.29}$$

where k_{linear} is the linear stiffness of the system and u_s is the structural displacement. Finally, the total energy E_{total} of the system is simply calculated in the following equation.

$$E_{total}(t) = E_{kin}(t) + E_{spr}(t) \tag{6.30}$$

The total energy of the system in this case only explicitly includes the structural energy and not the ice-structure interaction energy. In accordance with Section 6.2.3, the same time series of 1 s was selected from each of the 26020 and 23010 test runs and analyzed with respect to the net and total energy of the system as depicted in Figure 6.14 and Figure 6.15, respectively. For each of Figure 6.14 and Figure 6.15, the top and middle plots signify the net energy either into out out of the system, and the bottom plot indicates the total structural energy of the system. Focus is given to the middle plot because the increase or decrease of total energy of the system per frequency lock-in cycle should correspond to some net energy being imparted to the system per cycle. For the net energy per cycle in the middle plot, the colored points represent the integration from the preceding structural displacement peak to the displacement peak at which the colored point is located. Therefore, an increase in the total energy of the system from, for instance, the first to the second displacement peak should correspond to positive net energy from the ice-structure interaction less the structural dissipation. Time instances of displacement peaks were selected since the time between displacement peaks were the most uniform when compared to velocity, acceleration, or force peaks. For the points very close to zero, the red or blue color may not properly signal the actual net energy flux due to the uncertainty that is discussed below.

Information about the properties for the net energy of the system for the selected time series for each test run is provided in Table 6.3. Mentioned in Table 6.3 for the sake of acknowledgment are the number of frequency lock-in cycles for each test run; the difference in number of cycles during the truncated time series originates from the discrepancy in dominant natural frequency between the structures. The significant disparity in net energy for each test run can be attributed to the uncertainty in the computation of the stiffness, system mass, damping ratio, and velocity of the structure. Specifically, the damping ratio, which strongly influenced the energy dissipated by the structure, was considered for a single-degree-of-freedom system when in reality the system was not so. Also, the nonlinearity of the system springs probably further invalidated the method of computing the damping ratio. Moreover, the frequency lock-in phenomenon for both test runs was discovered to impact the motions of the structure in both the x-direction and the y-direction (see Chapter 7). Therefore, the results of the one-dimensional energy analysis were treated as vaguely indicative of energy behavior of the system, but generally as inconclusive.

Table 6.3: Properties of the net energy of the system from the 26020 and 23010 test runs.

Test run	26020	23010
Cross-sectional geometry	Rectangular	Circular
Number of frequency lock-in cycles [-]	4	5
Net energy from Equation 6.27 [J]	0.2597	0.2007
Net energy from Equation 6.30 [J]	0.0192	0.2588
Damping ratio for maximum displacement amplitude [-]	0.0211	0.0258

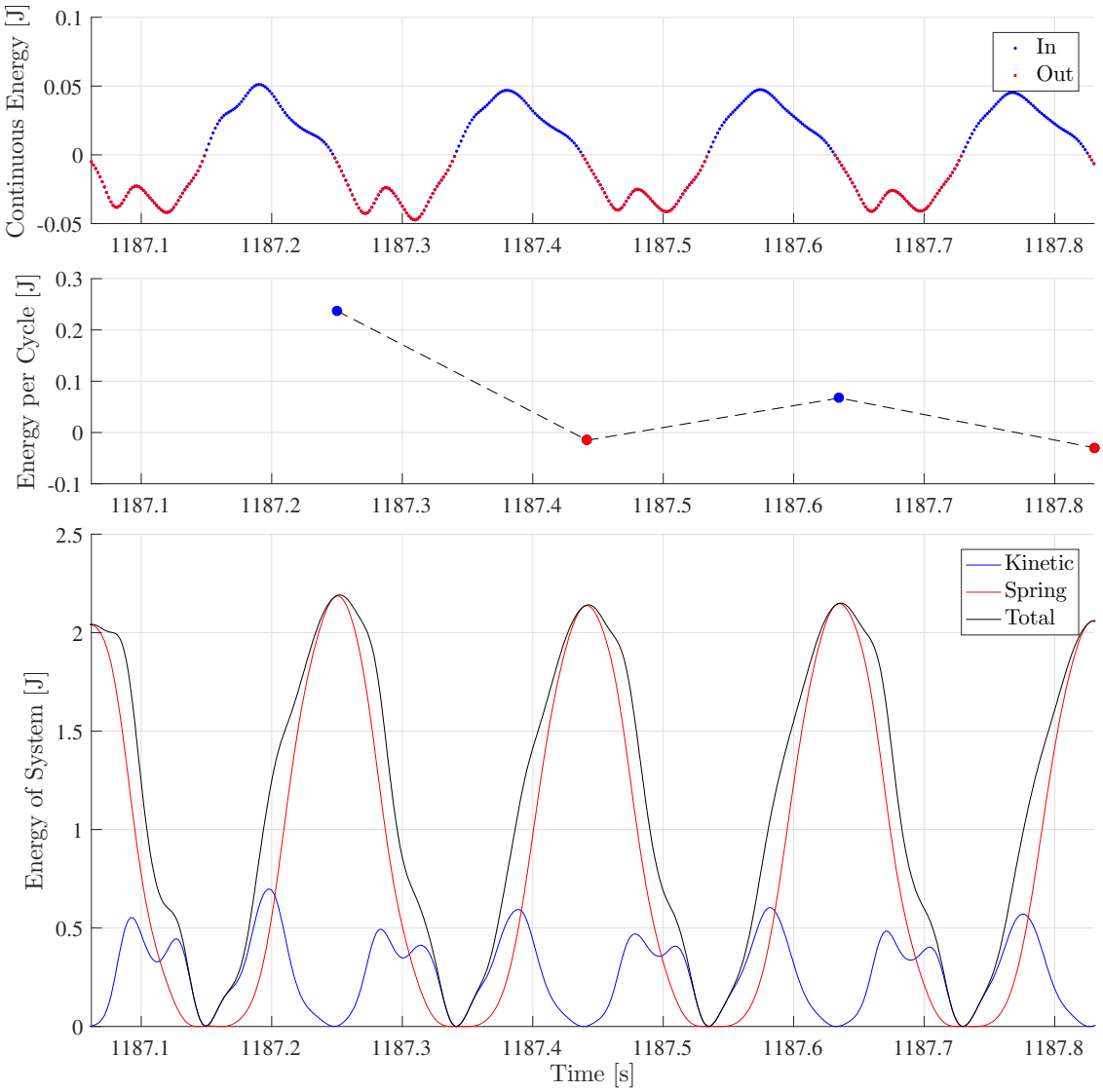

Figure 6.14: Energy components of the system for the 26020 test run.

6.3.1. FREQUENCY LOCK-IN RELATION AND ENERGY

As introduced in Section 3.2.2, the frequency lock-in relation β may have a value between 1.0 and 1.5 for frequency lock-in events (Hendrikse 2017). It is mentioned by Ziemer & Hinse (2017) that the range may be between 0.9 and 1.4, or even greater. But it was decided that the range for β stated by Hendrikse (2017) would be applied for this case. The frequency lock-in relation was computed for the selected time series at $v_{ice} = 19\,mm/s$ from the 26020 and 23010 test runs and compared in time to the net energy from ice-structure interaction and structural dissipation per frequency lock-in cycle (see Figure 6.16 and Figure 6.17, respectively). The time instants of β correspond to the time of maximum structural velocity and the lines connecting the points represent the trend over time and between frequency lock-in cycles for the frequency lock-in relation. Similarly, the colored points of net energy per frequency lock-in cycle correspond to integration between the velocity peaks and the association of the net energy per cycle to the second peak; the blue and red points represent net positive and negative energy, respectively. Generally, the frequency lock-in relation and the net energy for each test run follow similar trends. It can be postulated that an increase of energy into the system causes an increase in β; conversely, a decrease of energy into the system causes a decrease in β or at least reduces the increase in the frequency lock-in relation. It is especially apparent that negative net energy (energy out of the system from ice-structure interaction and structural dissipation) for a frequency lock-in cycle causes a decrease in β for that cycle.

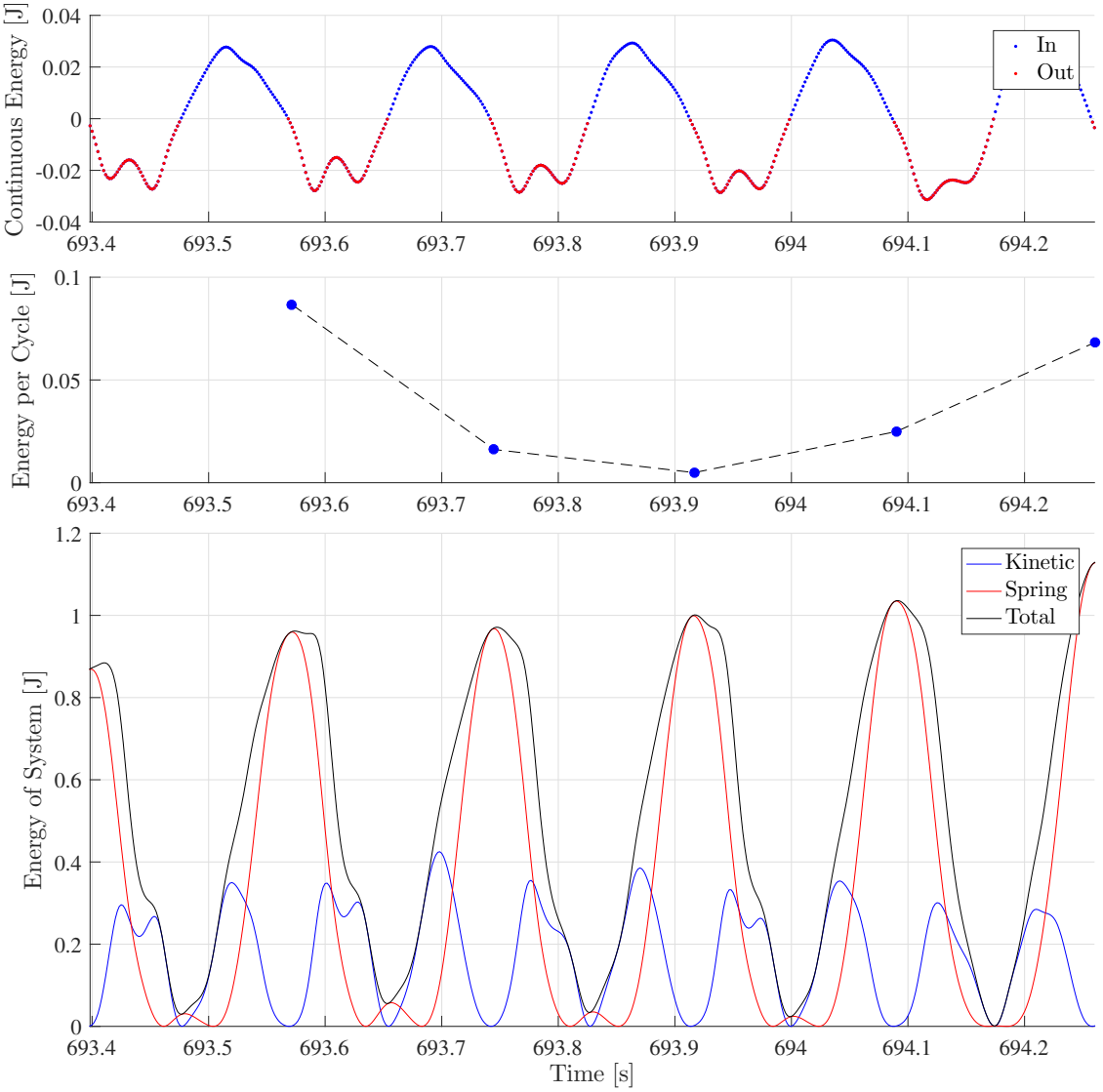

Figure 6.15: Energy components of the system for the 23010 test run.

6.4. EFFECT OF BUCKLING FAILURE ON FREQUENCY LOCK-IN

During the 23010 test run of the IVOS Phase 2 tests, it was observed that buckling failure of ice occurred frequently within the frequency lock-in regime of ice-induced vibrations. Generally, the buckling failure either impeded the development of or interrupted the sustained frequency lock-in cycles. However, quasi-sinusoidal structural displacement persisted regardless of the buckling failure, albeit with a lesser amplitude of displacement. To visually assess the influence of buckling failure on the frequency lock-in regime, a sample time series with two buckling failure events was distinguished (see Figure 6.18). Marked by vertical black dashed lines are the two buckling failure events: the first event at about 684.7 s and the second event at around 686.1 s. The substantial decrease in load accompanying the buckling events were only momentary; complete loss of contact between the structure and intact ice sheet did not seem to occur. Instead, perhaps asymmetric buckling occurred where only part of the contacting ice sheet buckled and separated while another portion of the ice sheet remained whole and in contact with the structure. Additionally, ice rubble may have transferred some load from the intact ice sheet to the structure; however, this load would have been small when compared to the unbuckled ice sheet in contact with the structure.

Based on the relative velocity and structural displacement, the frequency lock-in regime appeared to be only momentarily hampered by the buckling events, and recovered with one or two structural oscillations. With the structural response barely interrupted, the shape of the force signal began to regain the expected

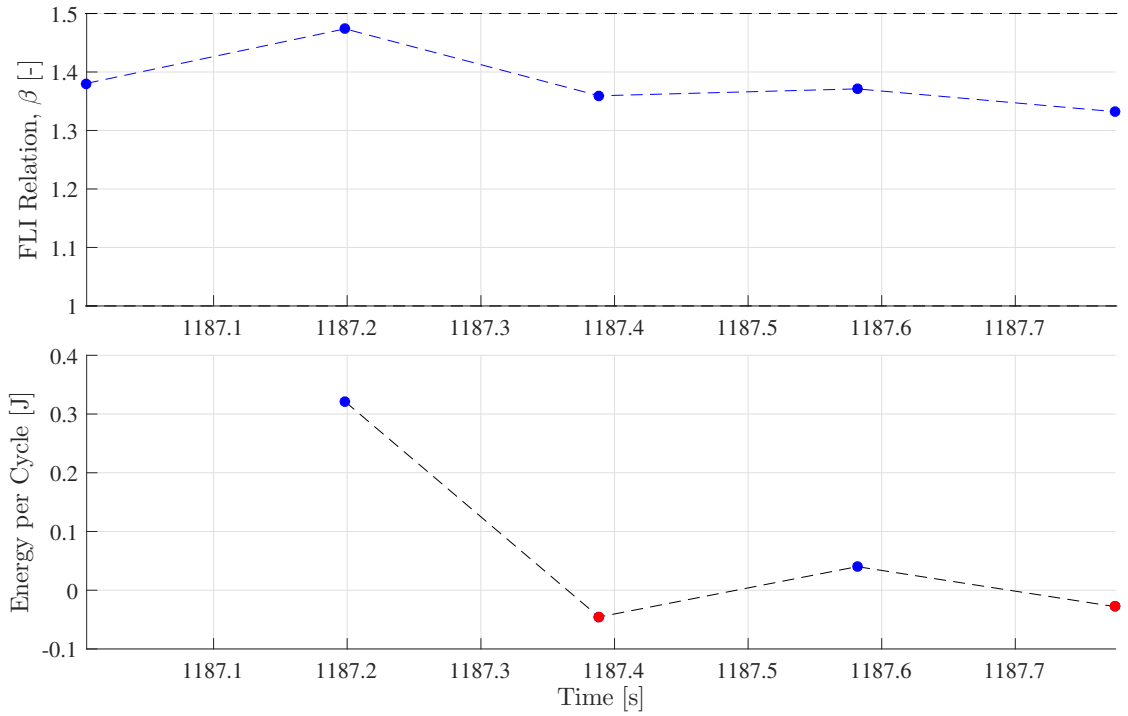

Figure 6.16: Frequency lock-in relation and the corresponding net energy per frequency lock-in cycle for the 26020 test run. Legend for energy per cycle: blue - positive net energy; red - negative net energy.

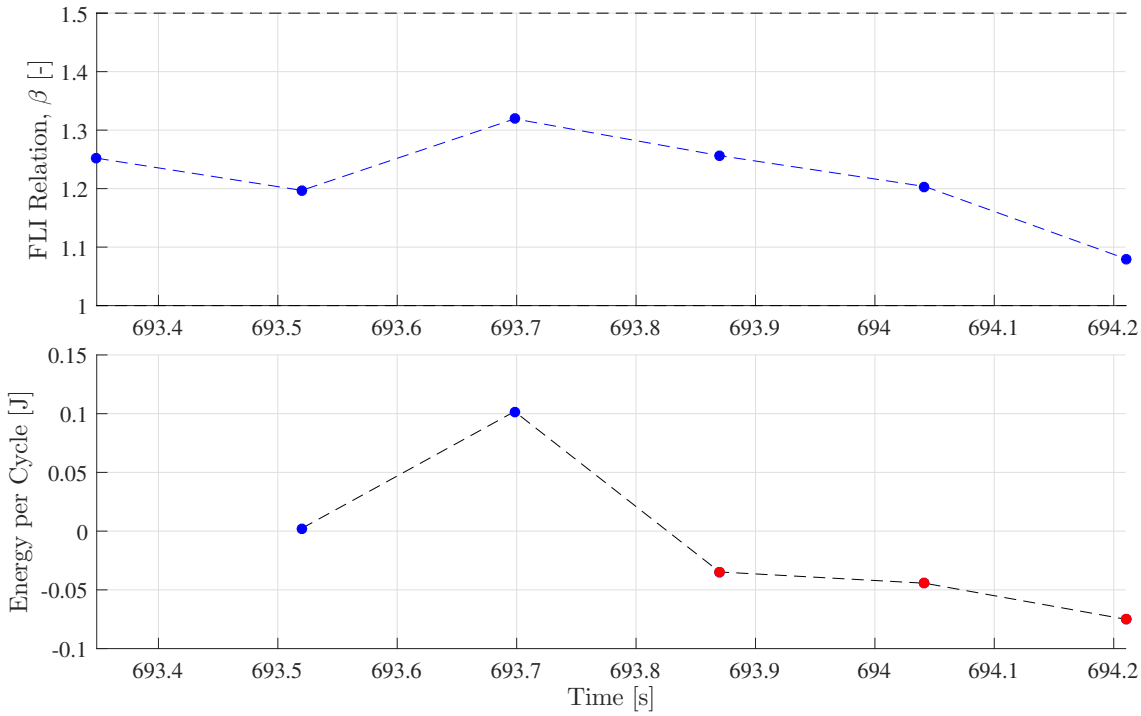

Figure 6.17: Frequency lock-in relation and the corresponding net energy per frequency lock-in cycle for the 23010 test run. Legend for energy per cycle: blue - positive net energy; red - negative net energy.

shape and the load gradually increased until reaching the second buckling event. In this case, the buckling events altered the force signal but did not cease the frequency lock-in vibrations. For further evaluation of the effect of buckling on the frequency lock-in regime, the frequency lock-in relation and the corresponding net energy were determined and are presented in Figure 6.19. From Figure 6.19, it can be observed that

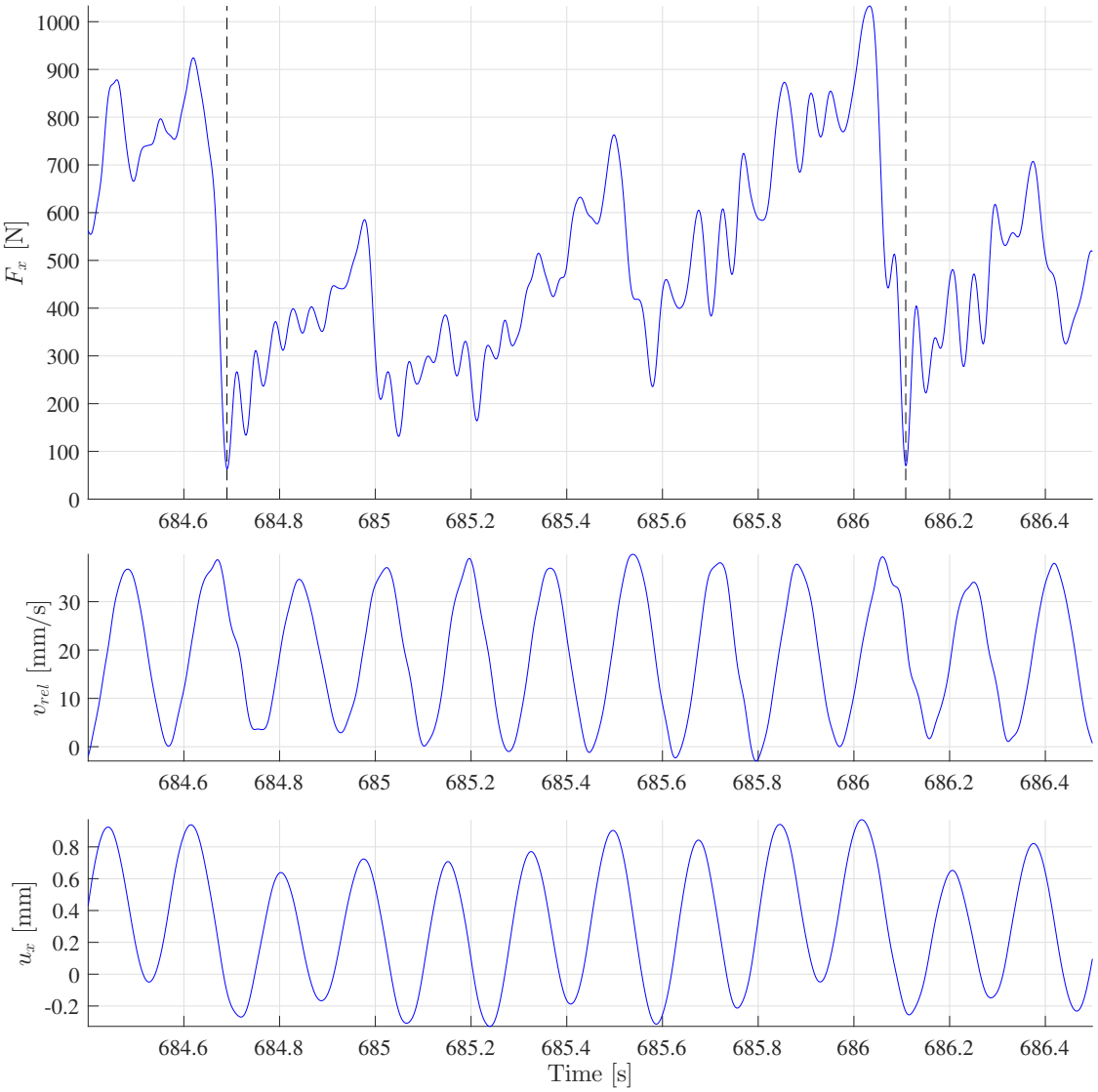

Figure 6.18: Ice-induced global force and corresponding relative ice-structure velocity and structural displacement in the x-direction for time series with ice buckling events from 23010 test run. The two instances of buckling failure are marked by vertical black dashed lines.

β dropped below the typical range of values for frequency lock-in around the buckling events and the net energy was remarkably negative. But the system quickly recuperated and resumed frequency lock-in cycles after one or two velocity peaks. Overall, the buckling events only hindered the frequency lock-in vibrations for about one or two oscillations of the structure; therefore, the buckling failure—in combination with crushing failure—of ice happened in tandem during the frequency lock-in regime from the 23010 test run.

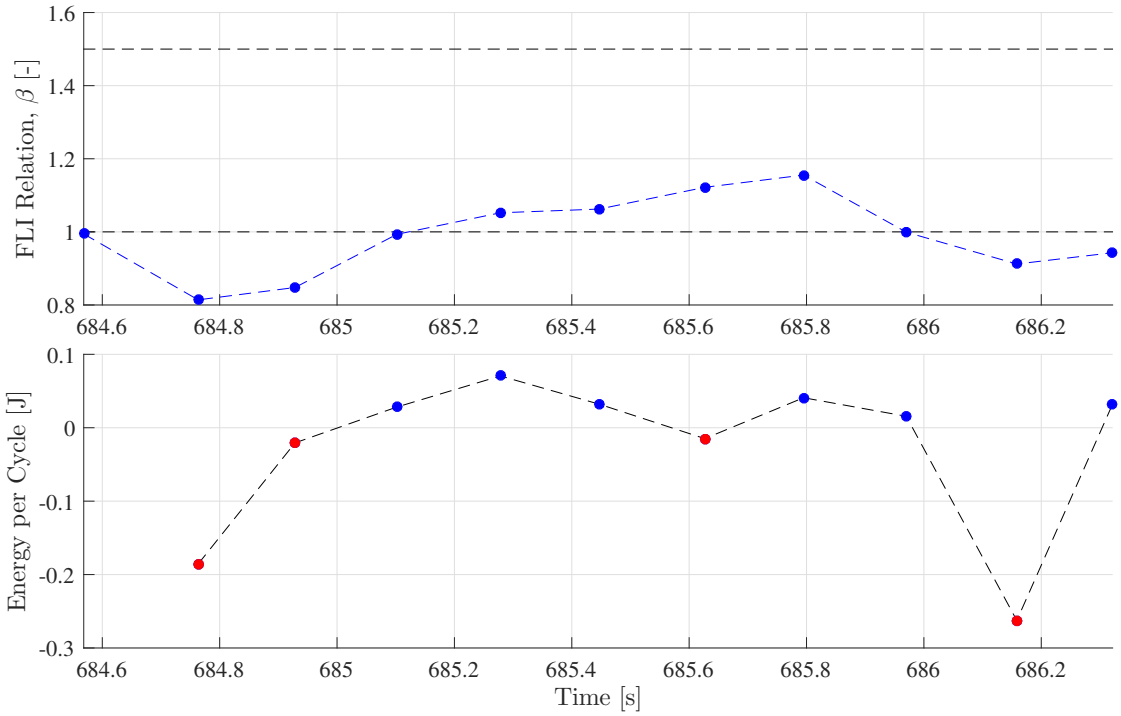

Figure 6.19: Frequency lock-in relation and the corresponding net energy per frequency lock-in cycle for time series with ice buckling events from the 23010 test run. Legend for energy per cycle: blue - positive net energy; red - negative net energy.

7

TWO-DIMENSIONAL ANALYSIS

While investigating the discrepancies between the net energy from ice-structure interaction and structural dissipation and from the difference between the final and initial total energy of the system (see Section 6.3, it was discovered that the y-direction motions of the model structures were not insignificant. Furthermore, the y-direction global loads were occasionally of the same order of magnitude as the x-direction loads. Thus, the frequency lock-in regime was re-analyzed with respect to both the x-direction and the y-direction for the 26020 and 23010 test runs. Again, only the data from Section 5.4 and scaled according to Section 6.1 were regarded in this chapter, albeit for both the x-direction and the y-direction. It is important to emphasize that this chapter is considered introductory and only provides some new insight about the two-dimensional effects of frequency lock-in vibrations on the model structures of the IVOS Phase 2 tests.

First, the ice-induced global loads in the y-direction are inspected for the 26020 and 23010 test runs in Section 7.1. Then, in Section 7.2, the motions of each model structure in the plane of the ice sheet during frequency lock-in are introduced. This is finally followed by analysis of the energy of the system, regarding both the x- and y-direction, in Section 7.3.

7.1. ICE-INDUCED GLOBAL LOADS

Analogous to Section 6.2.2, a normalized probability distribution and fitted Gaussian probability density function of the ice-induced global forces in the y-direction from the 26020 and 23010 test runs were computed as shown in Figure 7.1. A summary and comparison of statistical values of the global forces from each test run is given, as a supplement to the distribution, in Table 7.1. Notable, in Figure 7.1, is the fact that the y-direction global forces for the rectangular cross-section structure were distributed very narrowly about a positive mean, whereas the loads for the circular cross-section structure were distributed broadly about a near-zero mean. For the ice motion acting along an axis of symmetry of each of the model structures, one would expect an approximately zero mean for the loads in the crosswise direction as was observed for the circular cross-section structure. An explanation for the asymmetric y-direction loading on the rectangular cross-section structure could be that the structure was accidentally mounted to the 6-component scale such that the front side of the structure was not perpendicular to the direction of ice motion, i.e. the model structure was set at an oblique angle, which caused only the front side and the port side to experience prominent ice-induced forces from crushing (see Figure 5.2).

The magnitude of the y-direction forces was comparable to that of the x-direction forces for the 26020 and 23010 test runs (see Figure 6.9), but the x-direction forces were nevertheless dominant during the ice-structure interaction. The larger range and magnitude in global forces for the circular cross-section structure when compared to that of the rectangular cross-section structure can be attributed to the difference in cross-sectional shape between the structures. Ideally, very small loads would be anticipated for the y-direction of the rectangular cross-section structure because the starboard and port sides would be parallel to the direction of ice motion and thus would not experience significant, if any, ice-induced forces from crushing. Due to the asymmetry of the y-direction loads for the rectangular cross-section structure, the comparison of force statistics as displayed in Table 7.1 serve little purpose and were neglected for this study.

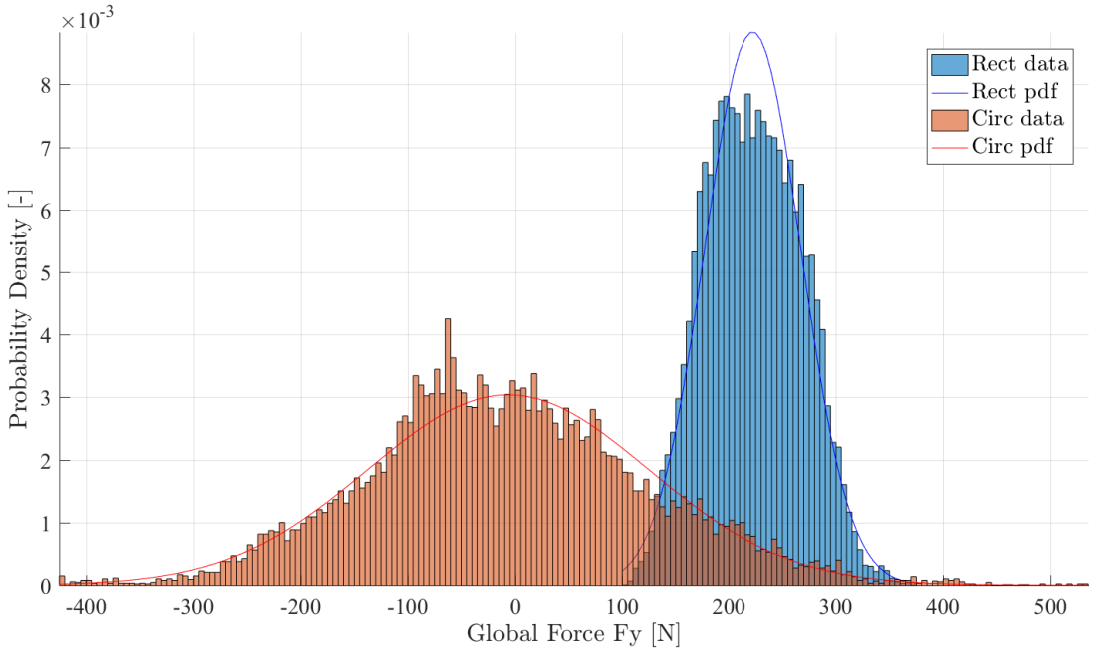

Figure 7.1: Normalized probability distribution and fitted Gaussian probability density function of the global forces in the y-direction from the 26020 ($Rect$) and 23010 ($Circ$) test runs. The probability density function is abbreviated to pdf in the legend.

Table 7.1: General statistical summary and comparison of the global forces in the y-direction from the 26020 and 23010 test runs.

Test run	26020	23010	**Circ/ Rect [-]**
Cross-sectional geometry	Rectangular	Circular	
Mean of force [N]	222	-6	-0.03
Standard deviation of force [N]	45	131	2.91
Maximum of force [N]	370	531	1.43
Minimum of force [N]	105	-425	-4.05

7.2. STRUCTURAL RESPONSE

In previous research, ice-induced vibrations of vertically sided structures in the frequency lock-in regime were treated as a one-dimensional scenario with the dimension being in the direction of ice motion. Since the test apparatus had equivalent system stiffness in the x-direction and y-direction, vibrations were permitted in the plane of the ice sheet. Although the dominant motions of each model structure were in the direction of ice motion, structural motions the crosswise direction were observed to be not unsubstantial. For each of the 1 s time series from the 26020 and 23010 test runs as utilized in Section 6.2.3, the in-plane structural displacements of the each model structure for the given duration are represented in Figure 7.2 and Figure 7.3, respectively. It can be observed that both model structures oscillated in a quasi-figure-eight pattern. For the rectangular cross-section structure, a double figure-eight pattern was apparent with small displacement amplitudes at the ends and larger displacement amplitudes towards the center of the pattern. Additionally, an asymmetry in the pattern was witnessed, which was due to the moderate asymmetric loading that was described in Section 7.1. For the circular cross-section structure, a more narrow-banded figure-eight formed, which may have been caused by the more symmetric y-direction loading.

It is important to note that, as discussed in Section 5.5.2, the y-direction displacements were derived from the y-direction acceleration measurements. This method could approximate the relative magnitudes of displacement amplitudes, but could not capture any time-variant mean displacements. Furthermore, the amplitude of the y-direction displacements were scaled according to the ratio between the x-direction displacement amplitudes from the laser transducer and the x-direction derived displacement amplitudes. Therefore, the y-direction displacements that are presented in Figure 7.2 and Figure 7.3 are perhaps qualitatively valu-

able but may not be accurate in terms of magnitude or mean. Regardless of the inaccuracy of the y-direction displacement, the in-plane motions of each model structure were interesting to visualize and discover this figure-eight pattern.

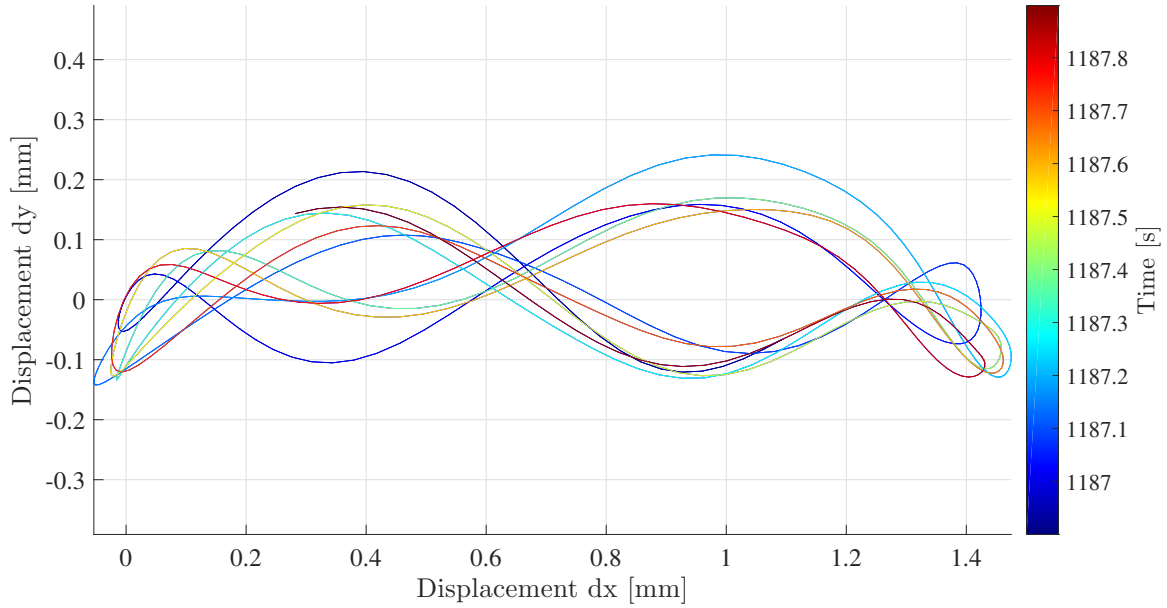

Figure 7.2: Structural displacement in the x- and y-direction over time for the 26020 test run.

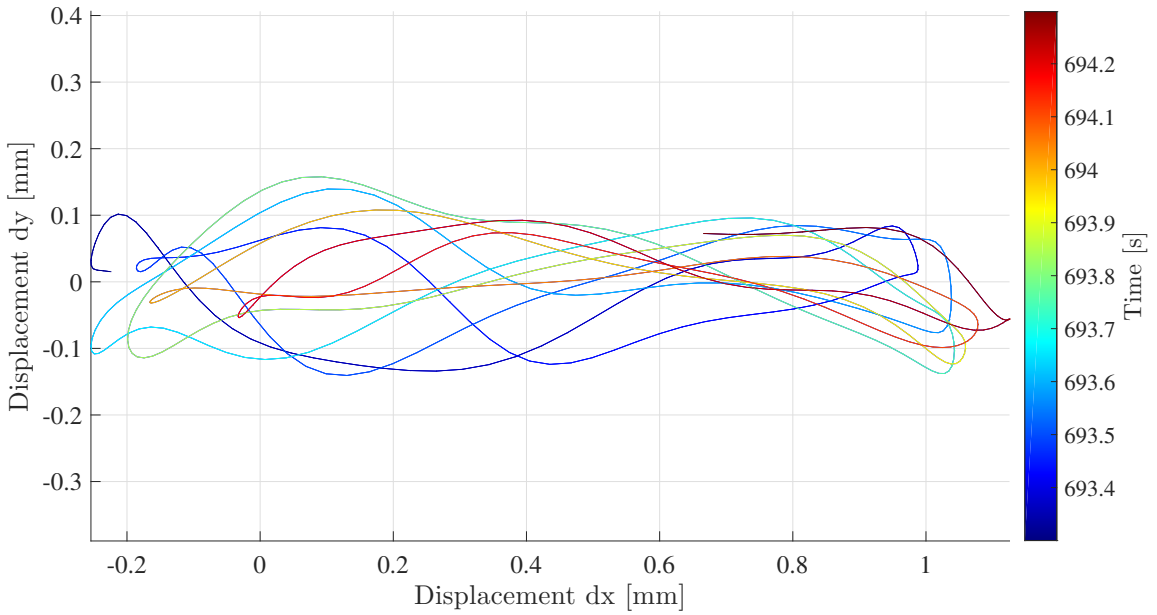

Figure 7.3: Structural displacement in the x- and y-direction over time for the 23010 test run.

7.3. ENERGY OF THE SYSTEM

As demonstrated in Section 7.2 by the sustained quasi-figure-eight patterns in the in-plane motions of the model structures during frequency lock-in vibrations, ice-structure interaction occurred not only for the x-direction but also for the y-direction. This y-direction ice-structure interaction implies that energy was im-

parted to the system from the crosswise direction. Therefore, the method of analyzing the energy of the system in Section 6.3 had to be reformulated for this situation in order to incorporate energy regarding both the x-direction and y-direction. To start, the energy from the in-plane ice-structure interaction E_{ice} per frequency lock-in cycle is computed as follows:

$$E_{ice} = \int_0^{T_{nat}} \left(F_{ice-x}\dot{u}_x + F_{ice-y}\dot{u}_y\right) dt \tag{7.1}$$

where F_{ice-x} is the x-direction ice-induced global force on the structure, $\dot{u}_x$ is the x-direction structural velocity, F_{ice-y} is the y-direction ice-induced global force on the structure, and $\dot{u}_y$ is the y-direction structural velocity. Next, the energy dissipated by the structure E_s per frequency lock-in cycle is calculated as follows:

$$E_s = 2\omega_{nat} m_{sys} \int_0^{T_{nat}} \zeta\left(\sqrt{(u_x(t))^2 + \left(u_y(t)\right)^2}\right)\left(\sqrt{(\dot{u}_x)^2 + \left(\dot{u}_y\right)^2}\right)^2 dt \tag{7.2}$$

where ζ is a function of the resultant structural displacement $u_s(x,y)$ as a function of time t and the resultant structural velocity $\dot{u}_s(x,y)$ is considered. The continuous energy from in-plane ice-structure interaction is considered as follows:

$$E_{ice}(t) = \int_t^{t+t_s} \left(F_{ice-x}(\tau)\,\dot{u}_x(\tau) + F_{ice-y}(\tau)\,\dot{u}_y(\tau)\right) d\tau \tag{7.3}$$

and the continuous energy dissipated by the structure is determined in the following relationship.

$$E_s(t) = 2\omega_{nat} m_{sys} \int_t^{t+t_s} \zeta\left(\sqrt{(u_x(\tau))^2 + \left(u_y(\tau)\right)^2}\right)\left(\sqrt{(\dot{u}_x(\tau))^2 + \left(\dot{u}_y(\tau)\right)^2}\right)^2 d\tau \tag{7.4}$$

The kinetic energy E_{kin} of the system from in-plane velocity is computed as follows:

$$E_{kin}(t) = \frac{1}{2} m_{sys}\left[\sqrt{(\dot{u}_x(t))^2 + \left(\dot{u}_y(t)\right)^2}\right]^2 \tag{7.5}$$

and the spring potential energy E_{spr} of the system from in-plane displacement is determined in the following equation.

$$E_{spr}(t) = \frac{1}{2} k_{linear}\left[\sqrt{(u_x(t))^2 + \left(u_y(t)\right)^2}\right]^2 \tag{7.6}$$

The equations from Section 6.3 that were not reformulated above are applied to the in-plane energy analysis in the same manner. Because the relaxation tests were performed only for the x-direction, the dominant natural frequency, system mass, damping ratio, and system stiffness were computed particularly for the x-direction. To continue with the analysis, it was dubiously assumed that all of the structural properties in the y-direction were equivalent to the structural properties in the x-direction, i.e. structural symmetry. For isolated structural responses in either the x-direction or the y-direction, this may be accurate given the symmetry of the model structure and the bending rods of the system springs. However, for combined x- and y-direction motions, the cross-section of the bending rods then acts as a diamond, which alters the linear stiffness and damping of the system. This issue was acknowledged but neglected for this study since no means of correction was readily available.

Similarly to Section 6.3, the same time series of 1 s was selected from each of the 26020 and 23010 test runs and analyzed with respect to the in-plane net and total energy of the system as depicted in Figure 6.14 and Figure 6.15, respectively. Also, a summary of the properties for the net energy of the system in the x- and y-direction for the chosen time series for each test run is provided in Table 7.2. In general, the in-plane energy of the system for both test runs was greater than that of just the x-direction energy of the system. Also, the contribution of the kinetic energy to the total energy of the system was more pronounced and resulted in a less sinusoidal shape of signal for the total energy. Inclusion of energy from both the x-direction and the y-direction should yield more accurate results. Yet, given the numerous uncertainties in the computations of the structural properties and the y-direction kinematics, the results of the energy analysis in the x- and y-direction were deemed inconclusive.

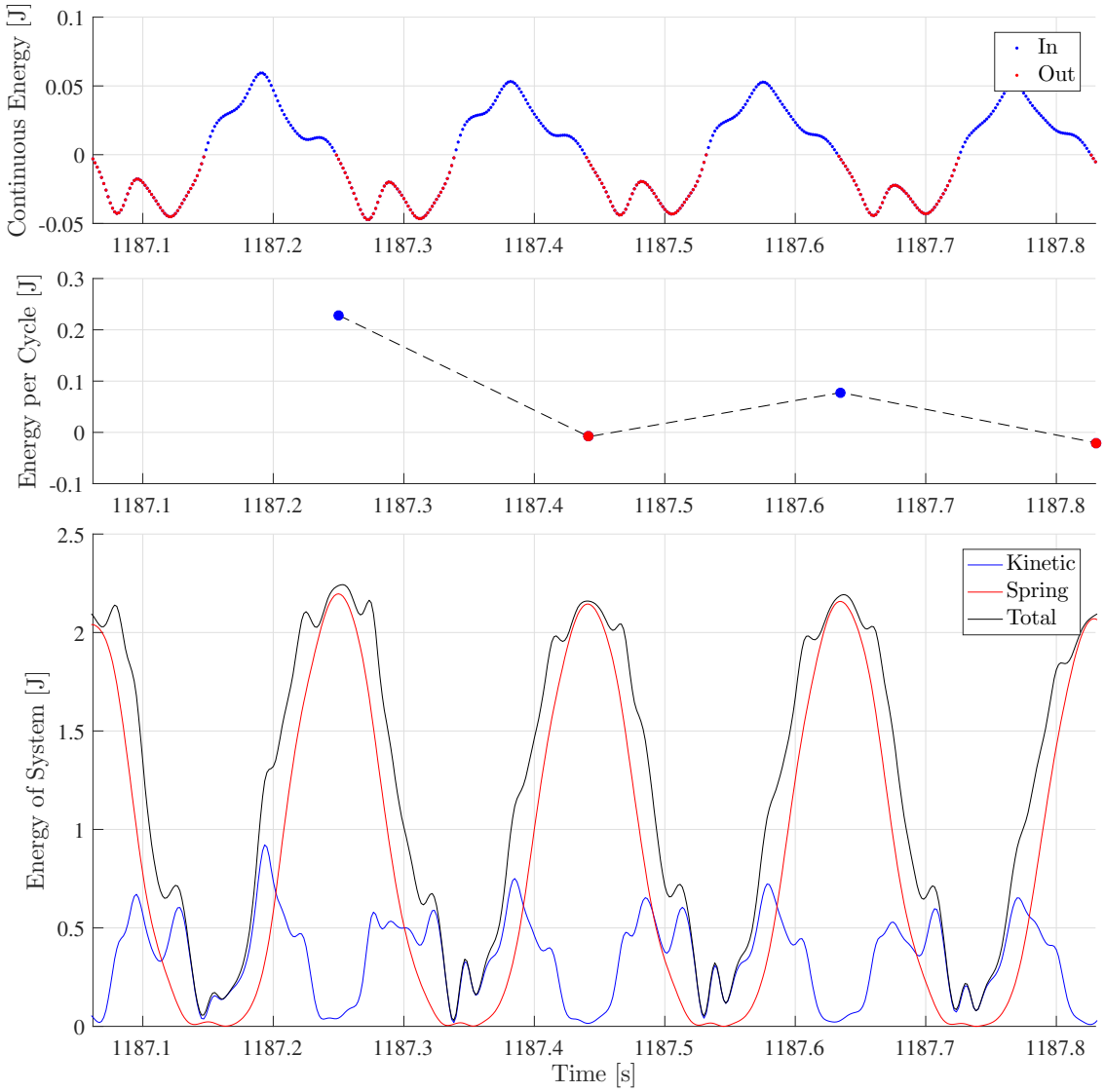

Figure 7.4: Energy components of the system in the x- and y-direction from the 26020 test run.

Table 7.2: Properties of the net energy of the system in the x- and y-direction from the 26020 and 23010 test runs.

Test run	26020	23010
Cross-sectional geometry	Rectangular	Circular
Number of frequency lock-in cycles [-]	4	5
Net energy from Equation 6.27 [J]	0.2777	0.2045
Net energy from Equation 6.30 [J]	0.0029	0.2613
Damping ratio for maximum displacement amplitude [-]	0.0212	0.0258

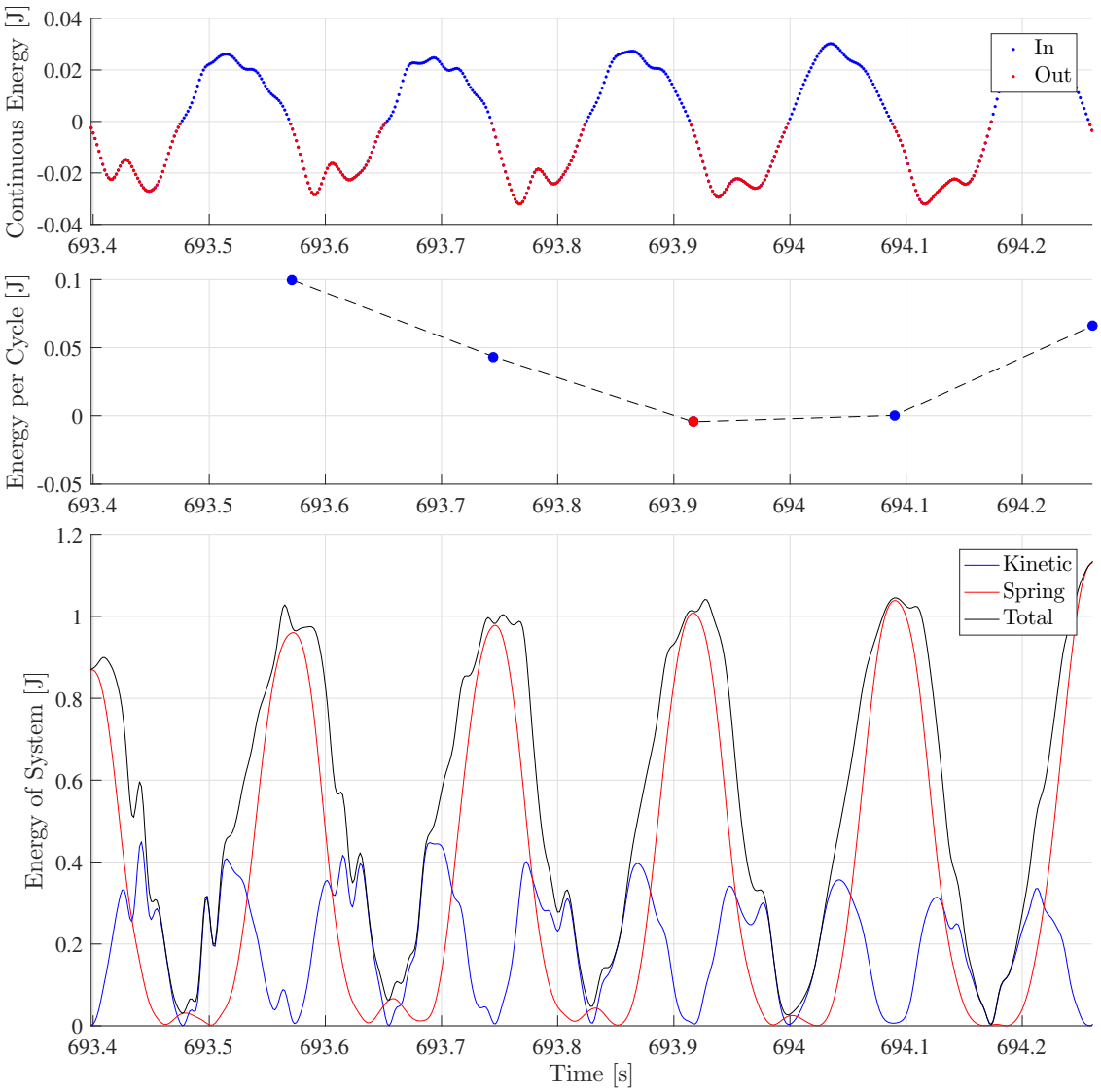

Figure 7.5: Energy components of the system in the x- and y-direction from the 23010 test run.

8

Conclusions and Recommendations

In this study, data from Phase 2 tests of the extensive IVOS experimental campaign, as undertaken by HSVA, were organized into a database for further research. Methods for post-processing the data were developed and applied to specific data sets. These data sets referred to tests with model structures of similar ice and structural properties, one of the structures with a rectangular cross-section and the other with a circular cross-section. Additionally, the data sets comprised conditions necessary for the model structures to experienced ice-induced vibrations in the frequency lock-in regime. Global behavior of the ice-structure interaction was performed in terms of ice-induced loads and energy of the system, and a comparison of this global behavior was made between the two different structures. To quantify the success of the research, the research objectives are discussed with respect to the level of completion in Section 8.1. Then, Section 8.2, the main conclusions are offered. Ultimately, recommendations are given in Section 8.3 for improving and expanding on the research performed in this study.

8.1. Fulfillment of Research Objectives

Presented in Section 1.2, the research objectives were executed in this study in order to answer the research questions. To evaluate the fulfillment of the research objectives, the tasks that were performed during the study and are relevant to each objective are discussed. The first research objective was to create a database for the IVOS Phase 2 tests; this was accomplished in Section 5.1. As for the universal analytical tools for data post-processing and manipulation, Chapter 5 provided a majority of satisfactory techniques for signal processing and corrections for the data. The second research objective was to, from the IVOS Phase 2 tests, select pertinent data and perform a comparative analysis of two different structures, one with circular cross-section and another with rectangular cross-section, that were subjected to ice-induced vibrations in the frequency lock-in regime. The IVOS Phase 2 tests were scrutinized in Chapter 4 and relevant data were discerned in Section 5.5. The method for identifying the frequency lock-in regime of ice-induced vibrations for a given structure was generally defined in Section 3.2.2 and applied satisfactorily in Section 5.5. Finally, a comparison of the global behavior of the ice-structure interaction between the different structures was attempted in Chapter 6 and Chapter 7. Results from the comparison were interesting, but changes in global behavior from differences in cross-sectional geometry could not be distinguished from differences in ice or other structural properties.

8.2. Conclusions

This study provides a foundation for further analysis of the IVOS Phase 2 tests. The application of the post-processing techniques that were discussed in Chapter 5 yield data that can be readily analyzed. Additionally, the post-calibration method as attempted in Section 5.4 granted insight into the relationship between pressure distributions along the ice-structure interface and the ice-induced global forces on the model structure. The global comparative analysis in Chapter 6 garnered qualitative information about the frequency lock-in regime and buckling failure of ice. It was observed that frequency lock-in vibrations usually persisted regardless of buckling events (see Section 6.4). For the frequency lock-in regime, the ice-induced global loads on the circular cross-section structure were generally lower than those for the rectangular cross-section structure. It

was unclear whether the difference in global loads between the structures was caused by the difference in cross-sectional shape, other structural properties, ice properties, or combinations thereof. The analysis of the energy of the system was intriguing but did not offer lucid conclusions. As for Chapter 7, the quasi-figure-eight pattern from the x-direction and derived y-direction structural displacements was an enlightening discovery that may later explain inconsistencies in the energy of the system. Based on the general configuration of the test apparatus from the IVOS Phase 2 tests and the results from the comparative analysis, it can be concluded that ice-induced vibrations of the model-scale structures in the frequency lock-in regime should be regarded as a two-dimensional problem.

8.3. RECOMMENDATIONS FOR FURTHER RESEARCH

Numerous recommendations for further research can be given considering that this study acts as a basis for developing more analysis of the IVOS Phase 2 tests. Regarding the assumptions for the tests, the test apparatus should be treated as a mass-spring-dashpot oscillator for the compliant basis that is coupled with a pendulum or beam for the 6-component scale and model structure. With this dynamical system, the bending of the 6-component scale can be included in the force and energy analysis in a more explicit fashion. Further validation of the method for computing the oscillating mass is required because inertial loads were observed in the global load measurements even after the inertial load attenuation was performed. The nonlinearity of the system springs can be investigated such that the stiffness of the system can be more accurately calculated. The determination of the structural damping needs improvement because the methods applied do not incorporate displacement amplitude dependence appropriately. Moreover, the frequency beating in the relaxation test measurements obfuscated the expected peaks of the signal for a single-degree-of-freedom system assumption. For the future, the relaxation tests should be executed for both the x- and y-direction based on the fact that the test apparatus had the same system stiffness in both directions and thus would be expected to experience significant motions in both directions. Furthermore, relaxation tests in the diagonal direction should be performed as well since the cross-section of the bending rods for the system springs were box-shaped and did not have symmetric stiffness in all in-plane directions.

From the post-calibration method, the criteria for determining relevant data points for calibration should be revised so that the specific regime of ice-induced vibrations and the corresponding deformation behavior of ice is reflected in the decision process. For example, the criteria for frequency lock-in should include choosing data points based on global load as well as whether transitional or brittle behavior governs the deformation of the ice at that point. The post-calibration method should be extended for applicability to the y-direction forces, which would require a different regression as the current power regression cannot accept negative values; the y-direction forces can be positive or negative depending on the side of the structure on which the forces act.

In terms of the pervading buckling failure of ice during the 23010 test run, a repeat of the test run with ice of higher compressive and flexural strength would provide a more suitable basis for comparison to the 26020 test run. Repetition of these test runs under more similar conditions may be difficult to achieve because the ice properties of each ice sheet are difficult to control. Nonetheless, the flexural strength of the ice and related probability of buckling cannot be scaled and therefore need to be more similar for comparison between the test runs to be made.

For the two-dimensional analysis, the addition of a laser transducer for measuring displacement in the y-direction would be crucial to accurately assessing the ice-induced global loads and energy of the system. Too much uncertainty exists in the computations of the y-direction displacements and assumptions for the y-direction structural properties. It is imperative that y-direction measurements for the structural properties and kinematics are recorded so that two-dimensional analysis can be properly performed.

A

IVOS Phase 2 Test Matrix

This appendix contains the test matrix from the IVOS Phase 2 tests, including Phase 2.1, 2.2, and 2.3 (see Table A.1, Table A.2, and Table A.3, respectively). For more information about the test matrix or design decisions regarding the test matrix, the reader is referred to HSVA.

Table A.1: Test matrix for IVOS Phase 2.1 test runs from Ziemer (2016).

Series	**Test Run**	**Diameter [mm]**	**System stiffness [N/mm]**	**Natural frequency [Hz]**	**Ice thickness [mm]**	**Ice flexural strength [kPa]**	**Ice compressive strength [kPa]**	**Indentation velocity (increment) [mm/s]**
21000	21010	500	2220	5.5	30.5	62	90	5-10 (5)
	21011							15-50 (5); 60-70 (10); 100
	21020		3020	7.6	30.5	53	80	5 7-8 (1); 10-100 (10)
22000	22010	200	1910	5.7	71	65	185	5-6 (1)
22100	22110		1960		81	29	149	5-6 (1)
	22120					32	103	5-9 (2); 10-11 (1)
23000	23010		1930	5.8	33	35	79	5-9 (2); 10-20 (5); 30-50 (10); 70 100 150
					42	45	97	5-9 (2); 10-20 (5); 30-50 (10); 70 100 150
	23020	500	2030	5.5	43		72	5-9 (2); 10-20 (5); 30-50 (10); 70 100

Table A.2: Test matrix for IVOS Phase 2.2 test runs from Hinse et al. (2017).

Series	Test Run	Diameter [mm]	System stiffness [N/mm]	Natural frequency [Hz]	Ice thickness [mm]	Ice flexural strength [kPa]	Ice compressive strength [kPa]	Indentation velocity (increment) [mm/s]
24000	24010	120	1935	5.4	41	69	136	3-70 (1); 75-110 (5); 120-200 (10)
	24020		rigid	-	43	64	136	3-10 (1); 15-20 (5); 30
	24021				43	64	136	150 100 70
25000	25010	200	1290	4.2	48	60	145	3-15 (2); 16-36 (1)
	25011					58	115	40-45 (1); 50-100 (5); 110-150 (10)
	25012							25
	25020		rigid	-	52	48	100	3-10 (1); 15-50 (5); 60-150 (10); 200
26000	26010	200 (283)	1915	5.6	44	60	110	3-10 (1); 15 20-50 (10); 70 100
	26020	200	1950	5.4	45	60	110	3-50 (1); 60-80 (10); 100 150

Table A.3: Test matrix for IVOS Phase 2.3 test runs from Hinse et al. (2017).

Series	Test Run	Diameter [mm]	System stiffness [N/mm]	Natural frequency [Hz]	Ice thickness [mm]	Ice flexural strength [kPa]	Ice compressive strength [kPa]	Indentation velocity (increment) [mm/s]
27000	27010	120	4300	6.8	34	140	630	5-10 (5); 20-100 (10); 150-200 (50)
	27020		2770	5.3	34	130	520	3-60 (1)
	27030				42	80	400	5-10 (5); 20-100 (10); 150-200 (50)

B

Post-processed Data for Analysis

This appendix contains the time series of post-processed data from the 26020 and 23010 test runs that were utilized for analysis. Figure B.1, Figure B.2, Figure B.3, and Figure B.4 comprise the data from the 26020 test run and Figure B.5, Figure B.6, Figure B.7, and Figure B.8 comprise the data from the 23010 test run. Note that for each test run the global force in the respective x-direction and y-direction and the ice velocity are repeated as visual reference.

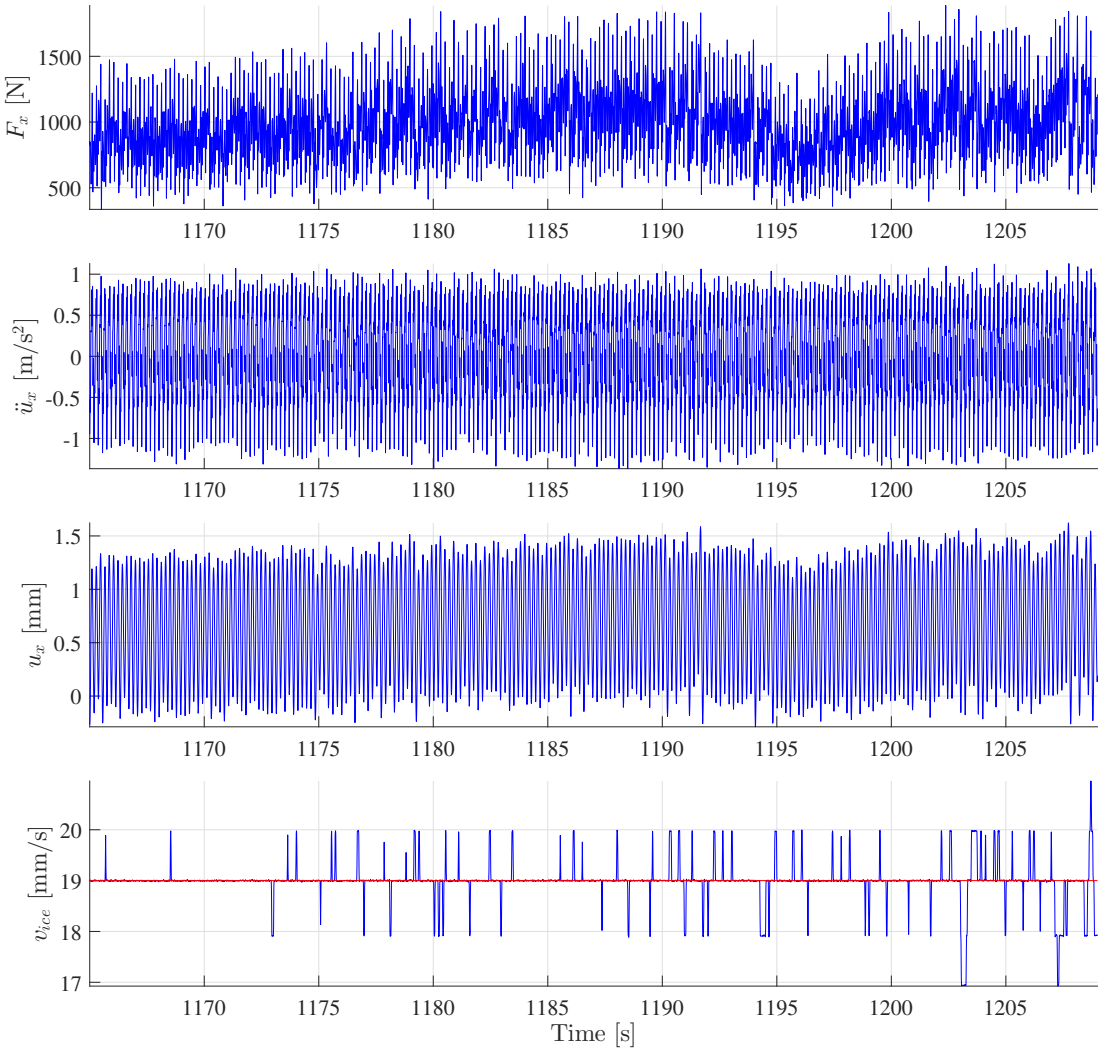

Figure B.1: Post-processed time series of global force, structural acceleration and structural displacement in the x-direction and ice velocity from the 6COMP system of the 26020 test run. The duration corresponds to a constant ice velocity of 19 mm/s.

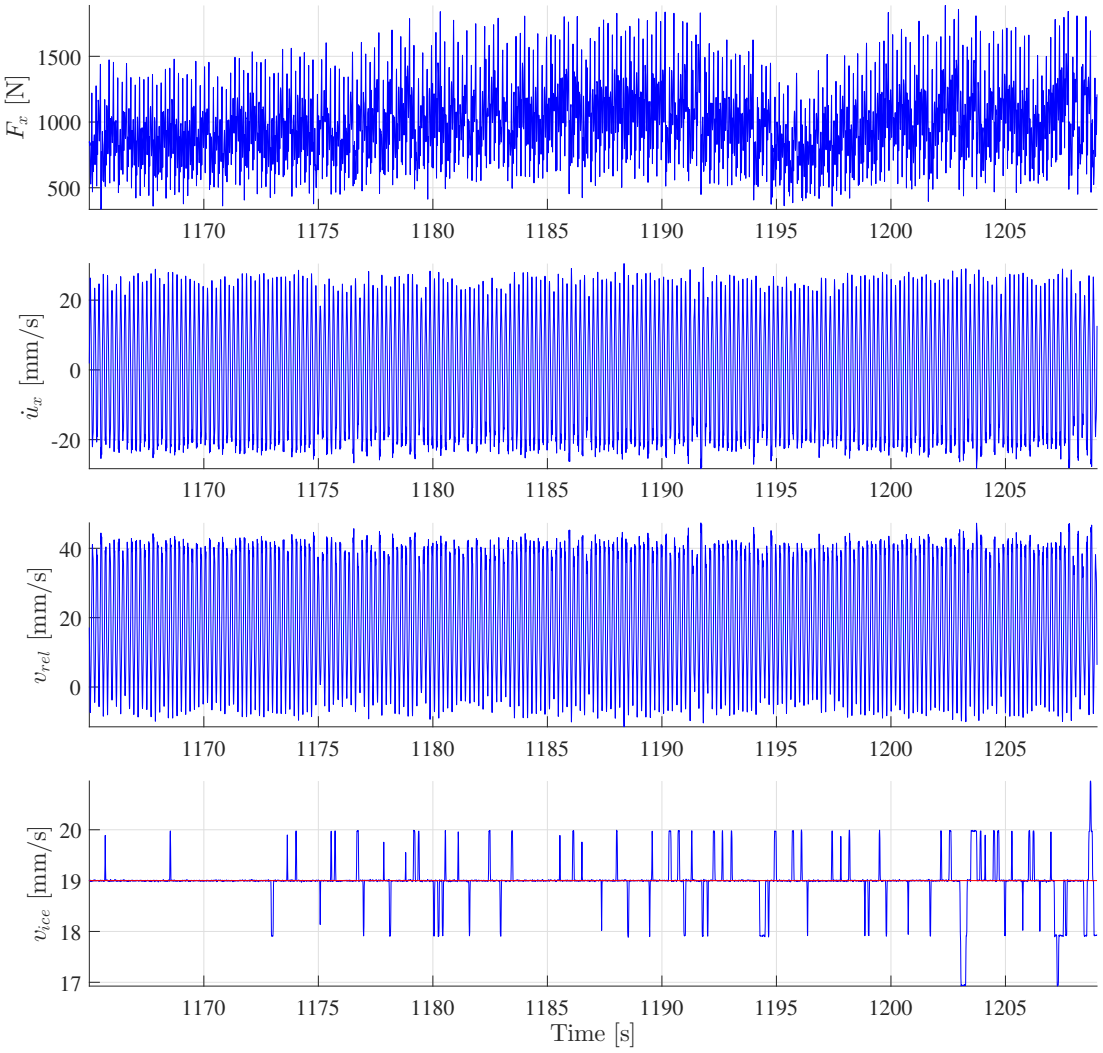

Figure B.2: Post-processed time series of global force, structural velocity and relative velocity in the x-direction and ice velocity from the 6COMP system of the 26020 test run. The duration corresponds to a constant ice velocity of 19 mm/s.

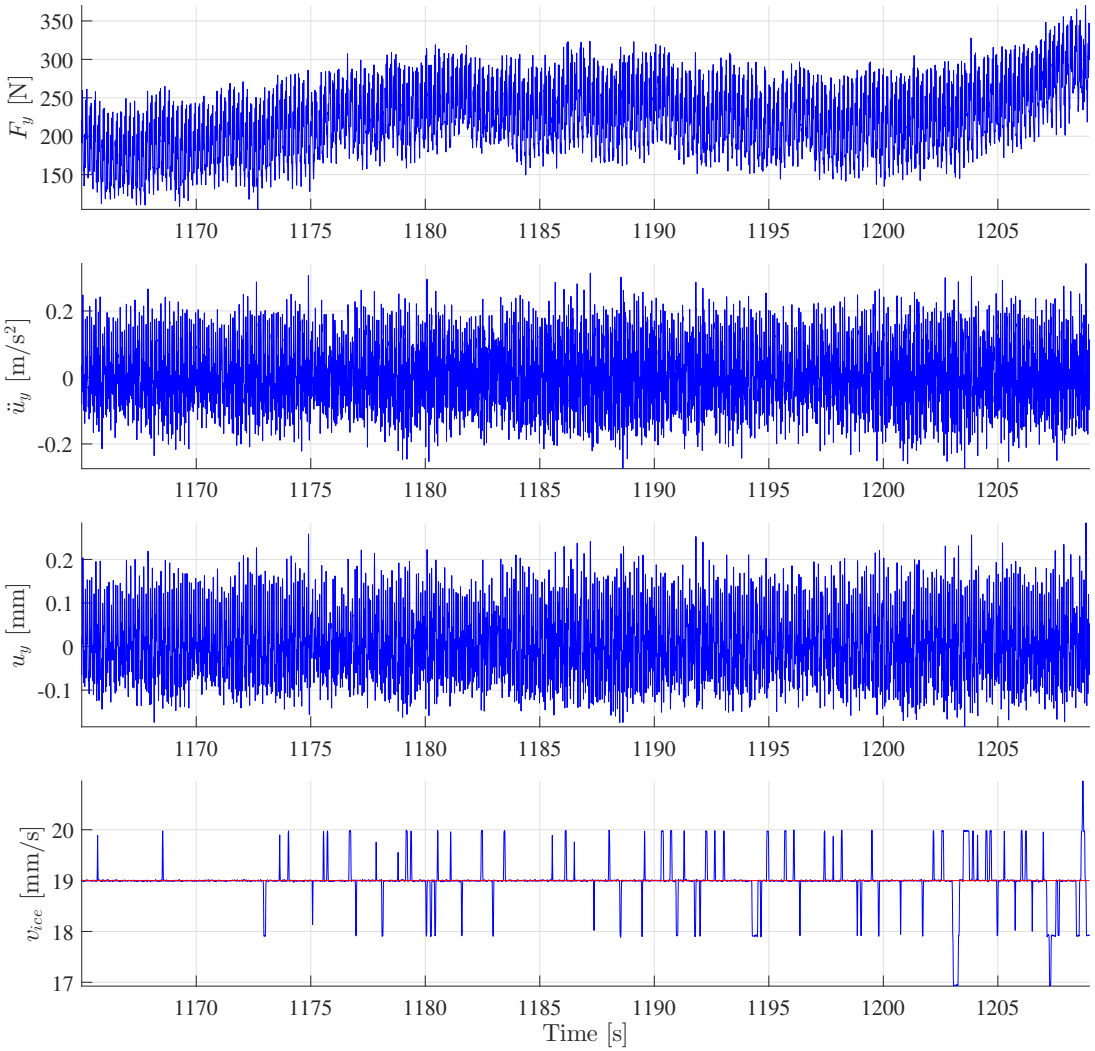

Figure B.3: Post-processed time series of global force, structural acceleration and structural displacement in the y-direction and ice velocity from the 6COMP system of the 26020 test run. The duration corresponds to a constant ice velocity of 19 mm/s.

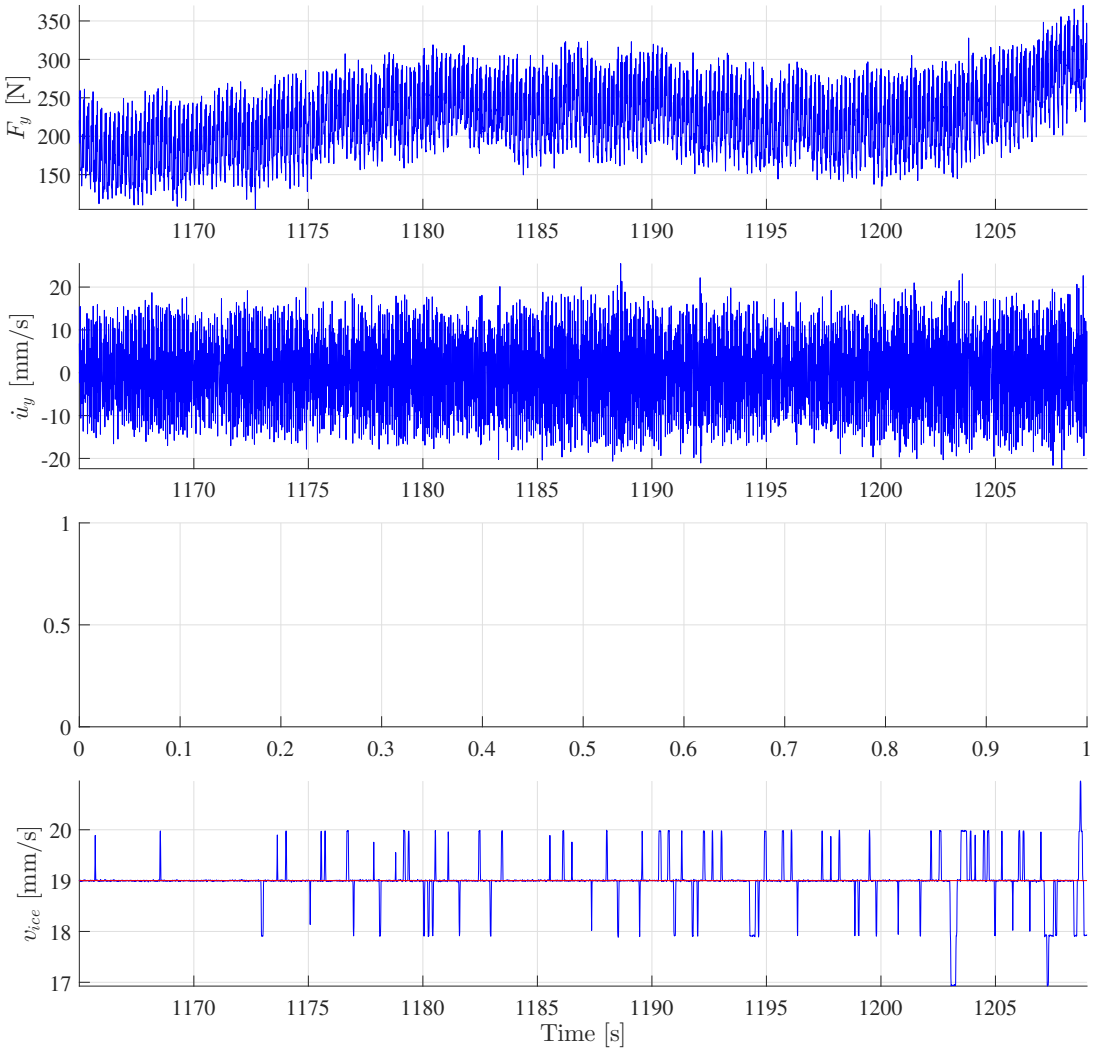

Figure B.4: Post-processed time series of global force and structural velocity in the y-direction and ice velocity from the 6COMP system of the 26020 test run. The duration corresponds to a constant ice velocity of 19 mm/s.

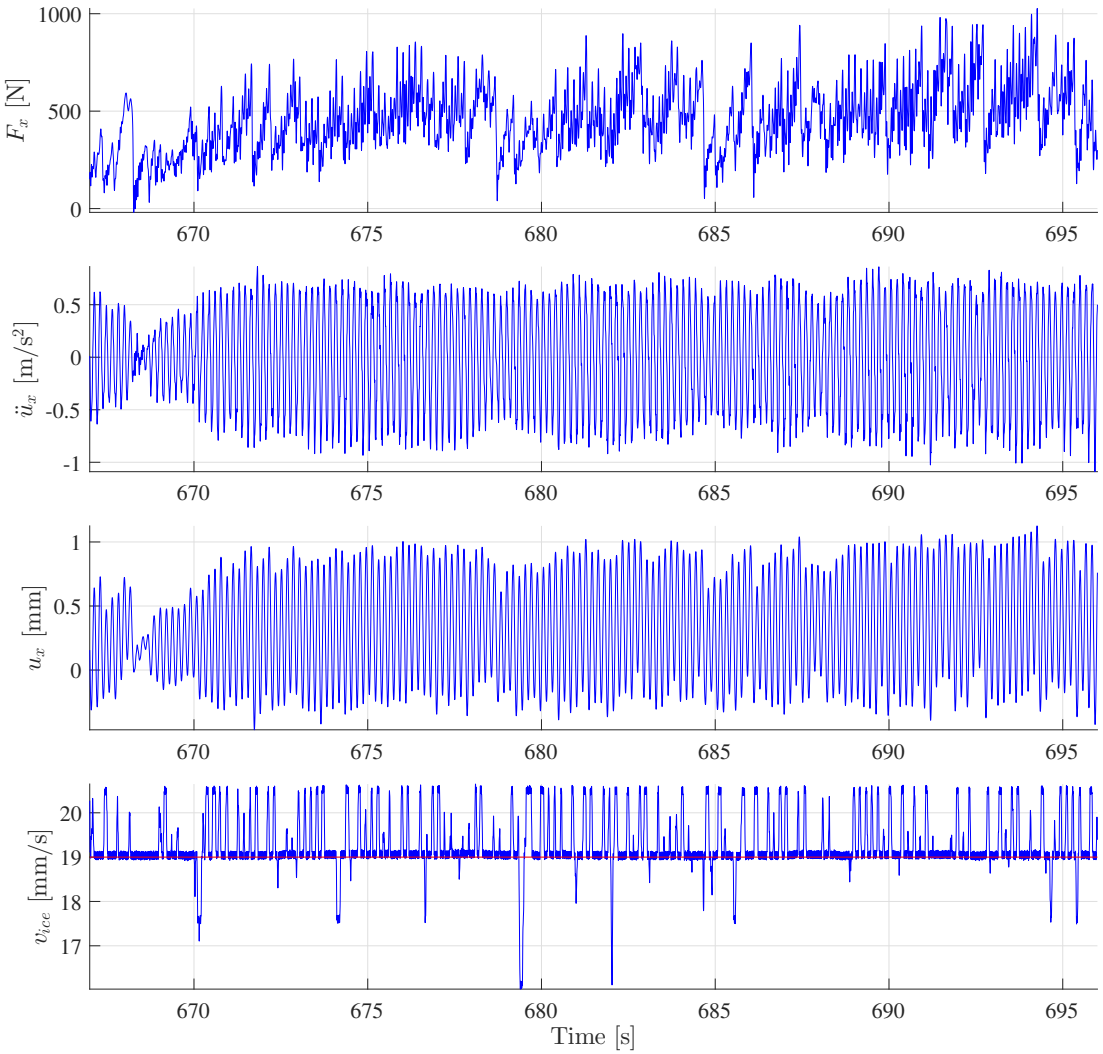

Figure B.5: Post-processed time series of global force, structural acceleration and structural displacement in the x-direction and ice velocity from the 6COMP system of the 23010 test run. The duration corresponds to a constant ice velocity of 19 mm/s.

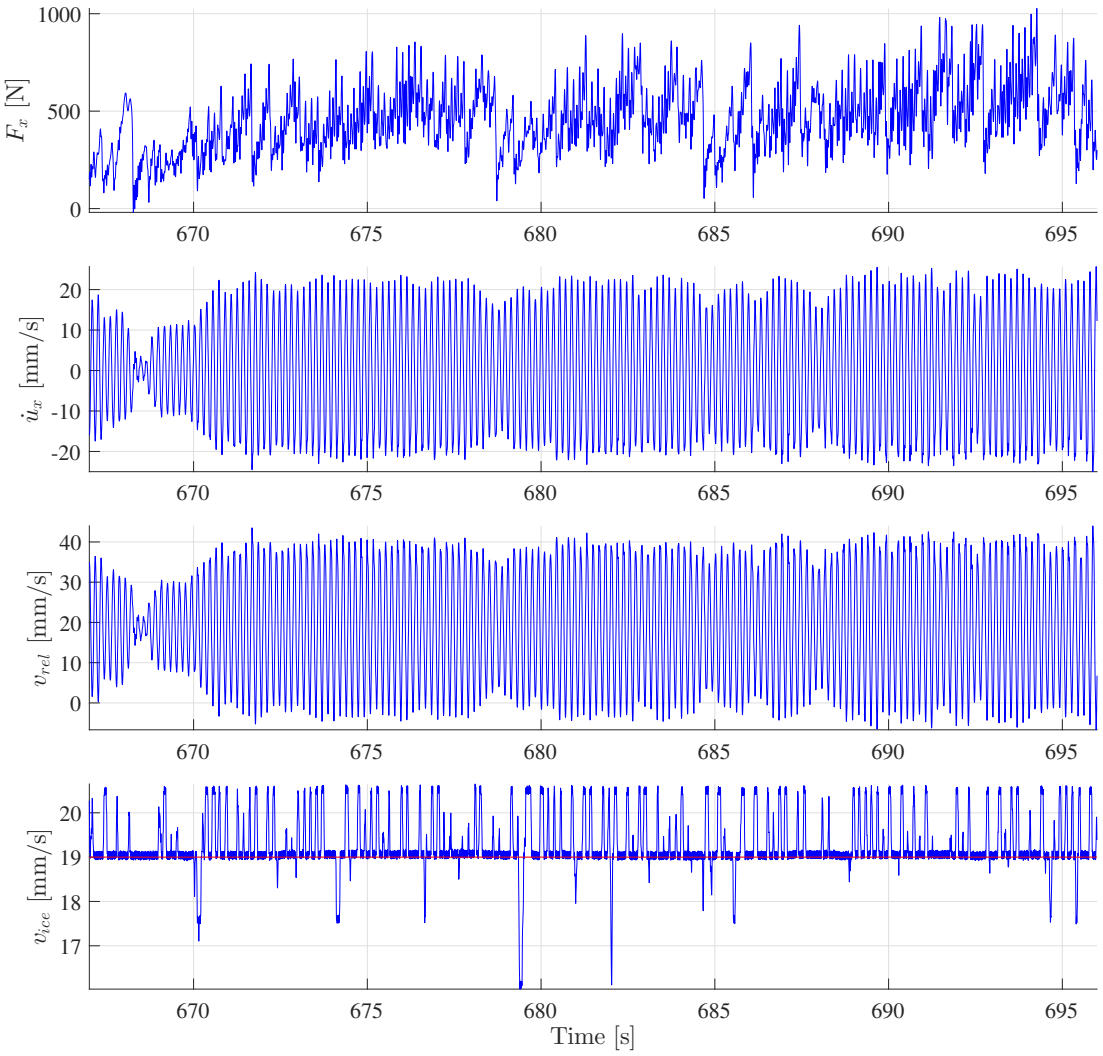

Figure B.6: Post-processed time series of global force, structural velocity and relative velocity in the x-direction and ice velocity from the 6COMP system of the 23010 test run. The duration corresponds to a constant ice velocity of 19 mm/s.

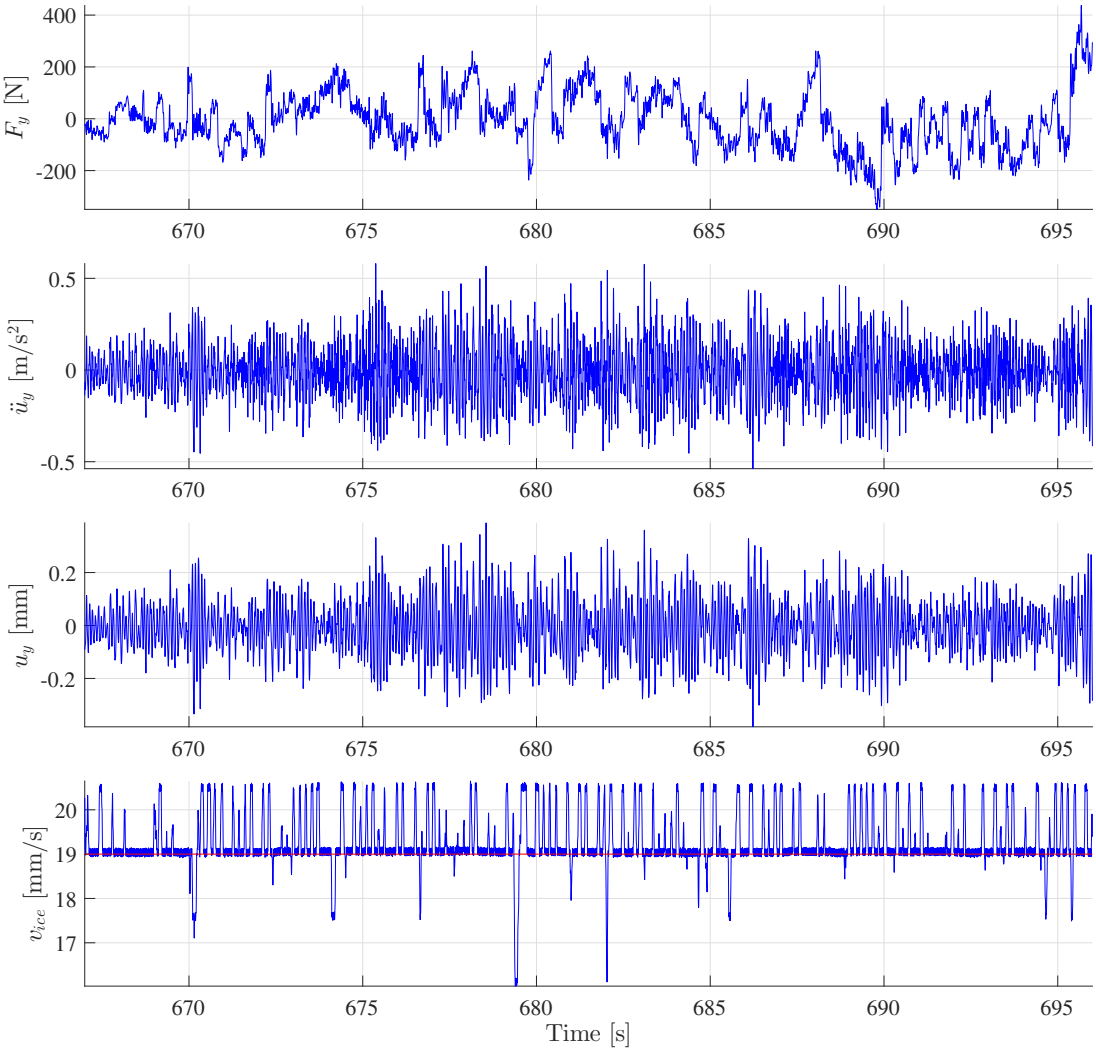

Figure B.7: Post-processed time series of global force, structural acceleration and structural displacement in the y-direction and ice velocity from the 6COMP system of the 23010 test run. The duration corresponds to a constant ice velocity of 19 mm/s.

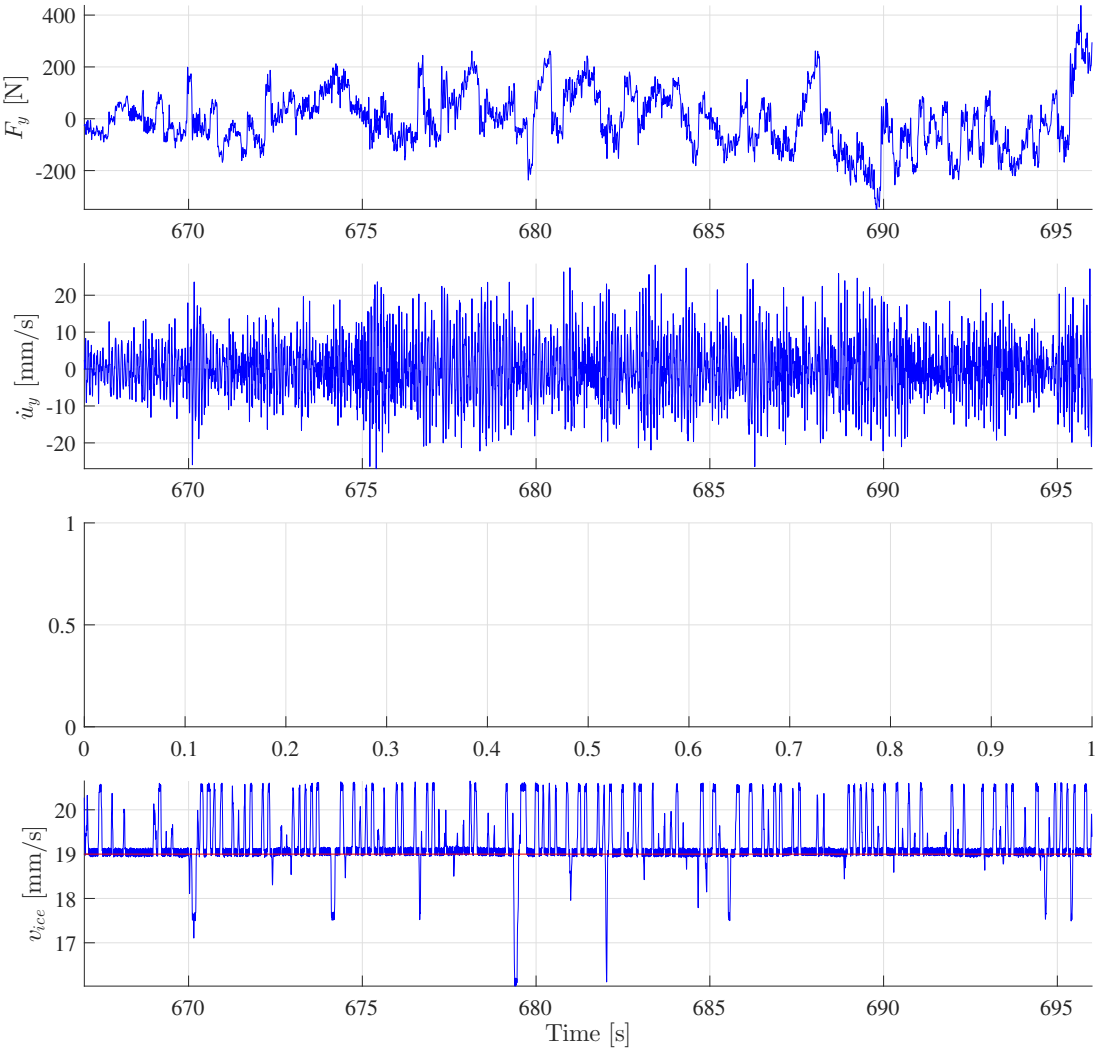

Figure B.8: Post-processed time series of global force and structural velocity in the y-direction and ice velocity from the 6COMP system of the 23010 test run. The duration corresponds to a constant ice velocity of 19 mm/s.

REFERENCES

Bjerkås, M., Meese, A. & Alsos, H. S. (2013), 'Ice induced vibrations - Observations of a full scale lock-in event', *Proceedings of the International Offshore and Polar Engineering Conference* **9**, 1272–1279.

Blanchet, D., Chrucher, A. & Fitzpatrick, J. (1988), 'An analysis of observed failure mechanisms for laboratory first year and multi-year ice', *Proceedings of the IAHR Ice Symposium* **3**, 89–136.

Evers, K.-U. & Jochmann, P. (1993), 'An advanced technique to improve the mechanical properties of model ice developed at the HSVA ice tank'.

Hendrikse, H. (2017), Ice-induced Vibrations of Vertically Sided Offshore Structures, Phd, Delft University of Technology.

Hendrikse, H. & Metrikine, A. (2015), 'Interpretation and prediction of ice induced vibrations based on contact area variation', *International Journal of Solids and Structures* **75-76**, 336–348.

Hendrikse, H. & Metrikine, A. (2016*a*), 'Edge indentation of ice with a displacement-controlled oscillating cylindrical structure', *Cold Regions Science and Technology* **121**, 100–107.

Hendrikse, H. & Metrikine, A. (2016*b*), 'Ice-induced vibrations and ice buckling', *Cold Regions Science and Technology* **131**, 129–141.

Hendrikse, H., Metrikine, A. & Evers, K. (2012), 'A Method to Measure the Added Mass and Added Damping in Dynamic Ice-structure Interaction : Deciphering Ice Induced Vibrations , Part 3', *21st IAHR International Symposium on Ice* pp. 972–984.

Hinse, P., Müller, F. & Ziemer, G. (2017), IVOS Progress Report, Technical Report April, HSVA, Hamburg.

Huang, Y., Shi, Q. & Song, A. (2007), 'Model test study of the interaction between ice and a compliant vertical narrow structure', *Cold Regions Science and Technology* **49**(2), 151–160.

ISO (2010), ISO/FDIS 19906:2010(E), Technical report, International Organization for Standardization.

Jordaan, I. J. (2001), 'Mechanics of ice-structure interaction', *Engineering Fracture Mechanics* **68**, 1923–1960.

Kärnä, T., Andersen, H., Gürtner, A., Metrikine, A., Sodhi, D., Loo, M., Kuiper, G., Gibson, R., Fenz, D., Muggeridge, K., Wallenburg, C., Wu, J.-F. & Jefferies, M. (2013), 'Ice-induced Vibrations of Offshore Structures – Looking Beyond ISO 19906', *POAC* pp. 1–12.

Kerr, A. D. (1978), 'On the determination of horizontal forces a floating ice plate exerts on structure', *Journal of Glaciology* **20**(82), 123–134.

Korzhavin, K. (1962), *Action of Ice on Engineering Structures*, Technical Report Translation TL260, U.S. Army Cold Regions Research and Engineering Laboratory.

Løset, S., Shkhinek, K. N., Gudmestad, O. T. & Høyland, K. V. (2006), *Actions from ice on Arctic offshore and coastal structures*, LAN, St. Petersburg.

Määttänen, M., Løset, S., Metrikine, A., Evers, K., Hendrikse, H. & Lønøy, C. (2012), 'Novel Ice Induced Vibration Testing in a Large-scale Facility : Deciphering Ice Induced Vibrations , Part 1', *IAHR* pp. 946–958.

Palmer, A. & Bjerkås, M. (2013), 'Synchronisation and the Transition from Intermittent to Locked-in Ice-Induced Vibration', *POAC* .

Palmer, a. C., Goodman, D. J., Ashby, M. F., Evans, a. G., Hutchinson, J. W. & S, P. a. R. (1983), 'Fracture and its role in determining ice forces on offshore structures', *Annals of Glaciology* **4**, 216–221.

Peyton, H. (1968), 'Sea Ice Forces', *Proceedings of Conference on Ice Pressures Against Structures, Laval University, Quebec* pp. 117–123.

Schulson, E. M. & Duval, P. (2009), *Creep and Fracture of Ice*, Cambridge University Press, New York.

Sodhi, D. S. (1991), Effective Pressure Measured During Indentation Tests in Freshwater Ice, *in* 'International Cold Regions Engineering Conference', Hanover, pp. 619–627.

Sodhi, D. S. (2001), *Crushing failure during ice-structure interaction*, Vol. 68, Pergamon.

Tekscan (2003), 'Tekscan I- Scan Equilibration and Calibration Practical Suggestions', pp. 1–51.

Timco, G. W. (1991), Laboratory observations of macroscopic failure modes in freshwater ice, *in* 'International Cold Regions Engineering Conference', Vol. 6, pp. 605–614.

Willems, T. (2016), Coupled Modeling of Dynamic Ice-structure Interaction on Offshore Wind Turbines, Msc, Delft University of Technology.

Ziemer, G. (2015), IVOS Progress Report, Technical Report November, HSVA, Hamburg.

Ziemer, G. (2016), IVOS Progress Report, Technical Report November, HSVA, Hamburg.

Ziemer, G. & Evers, K.-U. (2014), 'Ice Model Tests With a Compliant Cylindrical Structure to Investigate Ice-Induced Vibrations', *Omae* pp. OMAE2014–24011.

Ziemer, G. & Hinse, P. (2017), 'Relation of Maximum Structural Velocity and Ice Drift Speed during Frequency Lock-in', *Proceedings of the 24th International Conference on Port and Ocean Engineering under Arctic Conditions* .